Direct Photon Production in Hadron Induced Collisions

by

Vishnu V. Zutshi

Submitted in Partial Fulfillment

of the

Requirements for the Degree

DOCTOR OF PHILOSOPHY

Supervised by: Professor R. K. Shivpuri

Department of Physics and Astrophysics

University of Delhi

Delhi

1997

To Shalen

without whom this would never have been possible.

Acknowledgements

First and foremost I would like to thank my parents for the efforts and sacrifices they made to get me a good education. Many thanks to Mr. R. A. Alvi of [redacted] for showing me how interesting and challenging physics could be. Thanks are due to Prof. R. K. Shivpuri for giving me the opportunity to work at a first-rate research institution like Fermilab. I would like to express my gratitude to Prof. Paul Slattery for making my extended stay at Fermilab possible. His financial and moral support were crucial to the completion of this project. Many thanks to Prof. George Ginther and Prof. Marek Zielinski, my gurus on E706, for the patience and care they took in training me. Thanks to Prof. Tom Ferbel for constant encouragement and the innumerable letters of reference. The physical existence of this thesis owes more to Michael Begel than to anyone else. I would like to thank him and Lenny Apanasevich for the stimulating discussions and spirited cooperation I received from them, throughout my stay at Fermilab. Thanks to George Osborne, Dan Ruggiero, Jim Dunlea, Wieslaw Dlugosz, Nikos Varelas, Rob Roser, Dane Skow, Paoti Chang, Lucy deBarbaro, John Bacigalupi, Dave Striley, Lee Sorrell, Vijay Kapoor and Steve Blusk for being the great collaborators they all were. My sincere thanks to Indranil, Barnali, Yajnavalkya and Indermohan for being there whenever I needed them.

This work has been supported by grants from the National Science Foundation, U.S.A. and the University Grants Commission, India.

Abstract

This thesis presents an analysis of direct photon production by 515 GeV/c π^- and 530 and 800 GeV/c proton beams incident on beryllium target. The data on which this analysis is based was collected during the 1990 and 1991 fixed-target run of Fermilab experiment E706. A description of the experimental apparatus as well as reconstruction and analysis techniques is given. Inclusive direct photon and π^0 cross sections are presented as a function of p_T over the kinematic range $3 < p_T < 12$ GeV/c averaged over 1.5 units of rapidity. Comparisons of the measured cross sections to NLL QCD calculations are also made.

Table of Contents

List of Tables

List of Figures

Chapter 1 Introduction

This thesis presents results on inclusive direct photon production in hadron-hadron collisions from data collected during the 1990-91 fixed target run of experiment E706 at Fermi National Accelarator Laboratory. The results from E706's initial run in 1988 have already been published [1, 2, 3, 4]. E706 is a second generation experiment designed specifically for a high precision study of large p_T direct photon and neutral meson production. The apparatus used to perform the experiment consists of a large liquid argon calorimeter with a finely segmented electromagnetic section, a charged particle spectrometer using silicon vertex detectors in the target region and proportional wire chambers and drift tubes downstream of an analysis magnet.

1.1 Motivation

In our present understanding of hadron structure, hadrons are comprised of partons called quarks (spin 1/2 fermions) and gluons (massless spin 1 gauge bosons). The interactions between these partons is described by a gauge field theory, Quantum Chromodynamics (QCD) [5, 6], based on the non-abelian SU(3) colour gauge group. The strong interaction between two particles (described via QCD) is characterized by a coupling which is a function of the distance (which in scattering is related to the momentum transfer Q) between the two interacting partons. The QCD coupling strength exhibits the characteristic labeled 'asymptotic freedom'. That is, the coupling strength, decreases with decreasing distance or increasing momentum transfer.

It is this property of 'asymptotic freedom' which makes the study of parton-parton interactions extremely challenging because the flip side of smaller coupling

with decreasing distance is increasing coupling strength as the interacting particles separate from each other. Thus, the pardoxical situation in hadron interactions that to first order, the high energy cross sections are well described by the parton model, which views the hadron as a collection of non-interacting partons, and yet one cannot produce free quarks in scattering experiments. The inability to perform experiments with free quarks, couples the low and high energy regimes of the theory since the high energy scattering takes place between two partons whose states at the time of interaction are determined by the low energy evolution and interaction of partons in the parent hadrons. While the hard scattering can be calculated perturbatively, the probabilty of finding a particular parton in a particular state cannot because the coupling between partons is large and perturbation techniques become inadequate. Progress beyond this point is difficult unless one assumes factorization (see Figure 1.1), i.e., the short and long distance behaviour of the scattering process can be separated. Basically what one is claiming is that the initial state interactions occur too early and the final state hadronization happen too late to influence the hard scattering. Heuristically one can justify this by saying that the parton initial state is the result of interactions which occur on time scales of order 1 GeV^{-1} and so if the Q of the interaction is large (on the scale of 1 GeV) the interaction time is small and the partons are effectively frozen in definite states. Thus, the inclusive single particle production cross section in hadron-hadron collisions can be written as

$$\mathrm{E_C}\frac{\mathrm{d}^3\sigma}{\mathrm{dp_C^3}}(\mathrm{AB}\longrightarrow \mathrm{C}+\mathrm{X}) = \sum_{\mathrm{abcd}}\int \mathrm{dx_a dx_b dz_c G_{a/A}}(\mathrm{x_a},\mathrm{Q^2})\mathrm{G_{b/B}}(\mathrm{x_b},\mathrm{Q^2})$$

$$\frac{\hat{\mathrm{s}}}{\mathrm{z_c^2}\pi}\frac{\mathrm{d}\sigma}{\mathrm{d}\hat{\mathrm{t}}}(\mathrm{ab}\longrightarrow \mathrm{cd})\mathrm{D_{C/c}}(\mathrm{z_c},\mathrm{Q^2})\delta(\hat{\mathrm{s}}+\hat{\mathrm{t}}+\hat{\mathrm{u}})$$

where:

- a, b, c, and d label partons

- x_i is the fraction of the momentum of hadron 'I' carried by its constituent parton 'i'.

- Q is the scale of the hard scattering, which is assumed to be much greater than the mass of the hadrons and partons taking part in the scattering.

- $\hat{s}, \hat{t}, \hat{u}$ are the usual Mandelstam invariants in the partonic variables.

- $G_{i/I}$ are the parton distribution functions which give the probability of finding parton 'i' in hadron 'I' with momentum fraction between x and $x + dx$. They are determined from experiment and contain all the low energy behaviour or infrared sensitivity of the theory. These distribution functions are specific to each hadron but they can also be considered universal in the sense that they are assumed independent of any particular hard scattering process.

$\frac{d\sigma}{d\hat{t}}$ is the parton level hard scattering cross section which is calculable perturbatively.

$D_{C/c}(z_c, Q^2)$ is the fragmentation function which gives the probability of obtaining a particle 'C' with momentum fraction between z and $z + dz$ from a parton 'c'. Like the parton distribution functions, the fragmentation functions are also not calculable perturbatively and have to be determined from experiment.

It is the determination of these parton distribution and fragmentation functions that provides the motivation for doing precision direct photon physics.

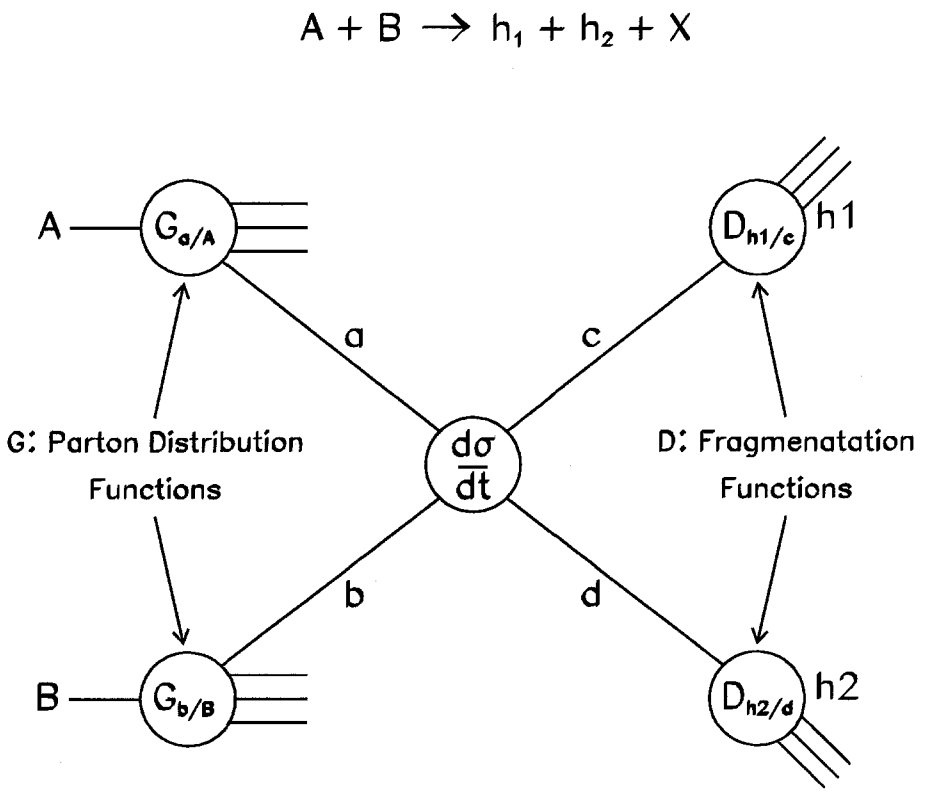

Figure 1.1 Hadron-Hadron scattering viewed as a factorizable process.

1.1.1 Direct Photons

Direct photons [7, 8] are photons that are produced in the hard scattering as opposed to photons from electromagnetic decays of hadrons such as $\pi^0 \longrightarrow \gamma\gamma$. Direct photons can serve as a very important tool in exploring the partonic structure of hadrons for the following reasons:

- To first order only two processes, the Compton and annihilation processes, contribute (see Figure 1.2). They are both of $O(\alpha\alpha_s)$ and thus one of the couplings, the electromagnetic quark-photon coupling, is well understood from QED.

- Contrary to Deep Inelastic Scattering (DIS) and Drell-Yan processes, the gluon is present at leading order in direct photon production. This makes this process especially sensitive to the gluon content of hadrons. The Compton process can be used to constrain the gluon distribution, while the annhilation process provides sensitivity to gluon fragmentation.

- Since the photon emerges from the hard scatter unaccompanied by a jet a study of direct photon production does not suffer from the ambiguities related to fragmentation and jet definition. This statement has to be tempered in light of the fact that some of the 'direct photons' may be coming from quark bremsstrahlung. However, for the E706 energy regime the bremsstrahlung contribution is not as significant as it is for colliders.

- Next to leading log (NLL) theory calculations for direct photon production are available and allow for comparisons between data and theory over a wide kinematic range.

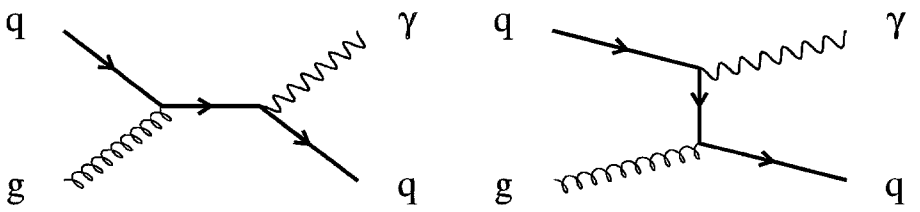

Compton Diagrams

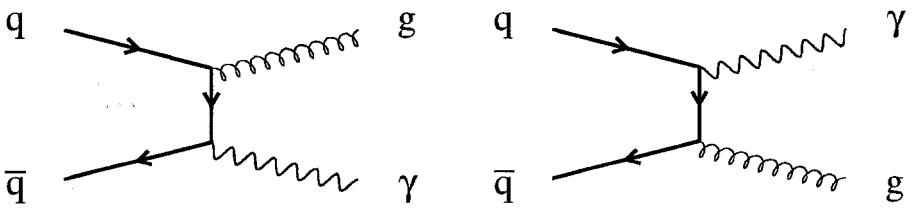

Annihilation Diagrams

Figure 1.2 Feynman diagrams for the two leading order direct photon production processes.

1.2 Challenges

Direct photon physics is not without its challenges though. Some of the major issues associated with this kind of analysis are as follows:

• It is a relatively rare process. Compared to jet production the direct photon production cross section is about three orders of magnitude smaller.

• The cross section is a steep function of p_T. It falls by about an order of magnitude for each GeV in p_T. Amongst other things this steep slope implies that even small uncertainties in the energy calibration of the photon detector translate to large uncertainties in the cross section.

• The 2γ decays of neutral mesons, such as the π^0 and η mesons, provide a significant source of background to the direct photon signal. These photons from neutral meson decay are indistinguishable from direct photons in the detector on a photon by photon basis and therefore a considerable effort has to be invested to remove them from the single photon sample.

1.3 Experimental Techniques

Some of the commonly used techniques to extract the direct photon signal are outlined below:

• Conversion Method: This technique is based on the expectation that the probability for a single photon to convert when passing through a given amount of material is significantly smaller than the probability for at least one of the pair of photons from a meson decay to convert when passing through that material. Experimentally this property is exploited by placing a converter, upstream of the photon calorimeter, between scintillator hodoscopes. The information from

the hodoscopes can be used to determine if a conversion took place inside the converter. The direct photon signal can now be statistically estimated by comparing the measured fraction of detected showers associated with events that have conversions in the converter to the expected conversion probability calculated assuming that there were absolutely no direct photon events present in the sample.

• Shower Profile Method: The transverse profile of showers from the $\gamma\gamma$ decay mode of π^0's and η's is different from that of a direct photon shower. Thus a shape which represents the transverse profile of a direct photon well, will not do the same for showers from a π^0 decay. A fit to the single shower profile, determined from either electron test beam data or a Monte Carlo simulation will therefore, yield larger χ^2 values for π^0 initiated showers than for direct photons. A judiciously placed χ^2 cut can then be used to statistically separate background from the direct photon sample.

• Direct Method: The $\gamma\gamma$ decays of π^0's and η's are fully reconstructed and identified using the two photon invariant mass distribution. Photons that are likely from π^0's or η's (according to the mass distribution) are excluded from the single photon sample. At this point, the candidate single photon sample consists of true direct photons and background. The background is due primarily to photons from misreconstruction of meson decays. The fractional background contribution is estimated by using a Monte Carlo simulation to estimate the rate at which photons from meson decays are misidentified as single photon candidates. This contribution is then statistically subtracted from the candidate single photon sample to extract the direct photon signal. This direct method, which requires a photon detector with superior position resolution, was used by Fermilab experiment E706.

Experiment	$\sqrt{s}$ (GeV)	Beam	Target(s)	x_T Range
E629	19.4	$\pi^{\pm}$, p	C	0.22 – 0.52
NA3	19.4	$\pi^{\pm}$, p	C	0.26 – 0.62
WA70	23.0	$\pi^{\pm}$, p	H	0.35 – 0.61
NA24	23.7	$\pi^{\pm}$, p	H	0.23 – 0.59
UA6	24.3	p, $\overline{p}$	H	0.28 – 0.58
E706	**31.1,31.6,38.8**	**$\pi^{\pm}$, p**	**H,Be,Cu**	**0.21 – 0.77**
R108	62	p	p	0.17 – 0.42
R110	63	p	p	0.14 – 0.29
R806	31,45,53,63	p	p	0.12 – 0.38

Table 1.1 Selected direct photon experiments [9].

1.4 Direct Photon Experiments

Study of direct photon production is a mature field and a number of experiments have published results comparable to those contained in this thesis. Table 1.1 gives a listing of these experiments. The first six experiments are fixed target experiments while the rest were performed with colliding beams. As mentioned earlier, this thesis presents results from the Fermilab fixed target experiment E706. One of the highlights of the E706 data sample is that it spans the x range from the middle of the ISR results through the upper end of most of the other fixed target results in a single experiment. In addition the E706 data sample contains the highest energy π^- beam data.

Chapter 2 The Spectrometer Elements

The E706 experimental apparatus was optimized for a high precision study of large p_T direct photon and associated jet production. A schematic diagram (Figure 2.1) [1] and a listing of the main elements of the Meson West spectrometer is provided below. The coordinate axis chosen for the spectrometer had its origin in the vicinity of the targets. The nominal beam direction defined the Z-axis while the Y-axis was the vertical direction.

Beamline : To transport positively and negatively charged particles in the momentum range 25 to 1000 GeV/c.

Cerenkov Detector : 42.1 meters in length and 24.4 cm in radius for tagging minority particles such as kaons in the beam.

Hadron Shield : Stack of steel 4.3 meters wide, 4.7 meters long and 3.7 meters high to absorb beam halo particles.

Veto Walls : Four walls of scintillator counters (two upstream and two downstream of the hadron shield), each divided into four quadrants, for tagging beamline muons.

Hodoscope : Three planes of tiny scintillator paddles covering a total area of 2x2 cm^2, used to identify beam particles incident on the target.

Target : Approximately 2m downstream of the hadron shield, consisting of two 0.8 mm copper pieces followed by two 1 cm diameter beryllium cylinders of length 3.7 and 1.1 cm.

---

[1] Also shown in the figure is the downstream muon system primarily used by experiment E672, the high mass dimuon study which took data concurrently with E706.

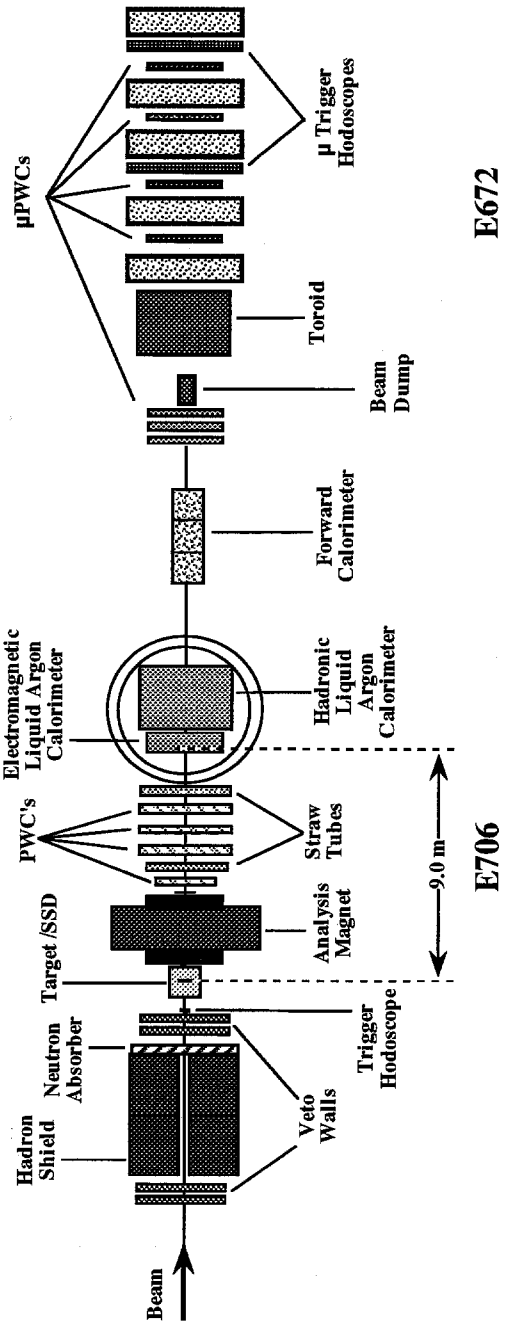

Figure 2.1 A schematic drawing of the Meson West Spectrometer in the 1991 run configuration.

Beam SSD : Three pairs of silicon strip detectors (3x3 cm^2 wafers with 50 μm pitch) located upstream of the target for recording beam track information.

Vertex SSD : Five pairs of silicon strip detectors (5x5 cm^2 wafers with 50 μm pitch except for the first pair which had 25 μm pitch in the central region) located downstream of the target for track and vertex reconstruction.

Beam Hole Counter : Scintillation counter with 1.0 cm hole in the middle used to define the transverse beam size to match the SSD acceptance and veto events with multiple beam particles.

Analysis Magnet : Dipole electromagnet operating at a current of 1050 Amperes producing a field of 6.2 kG used to evaluate the momenta of charged particles produced in interaction in the target.

Interaction Counters : Four scintillator counters (two upstream and two downstream of the analysis magnet) for signalling the occurence of an interaction in the target region.

PWC: Sixteen planes, grouped in four modules, of proportional wire chambers (2x2 m^2 with an anode wire spacing of 2.5 mm) for charged particle tracking.

Straws : Two chambers of straw tube drift chambers (one located between PWC module 1 and 2 and the other downstream of PWC module 4) for better linking and momentum determination.

LAC : Located 9 meters downstream of the target and divided into an Electromagnetic and Hadronic section, the Liquid Argon Calorimeter was used to measure the position and energies of photons, electrons and hadrons produced in the interaction.

FCAL : A scintillator calorimeter located 15 meters downstream of the target. The Forward Calorimeter was used to measure the energy of the fragmentation products of the non-interacting partons travelling down the beam hole.

Chapter 3 The Spectrometer Systems

Groups of elements, outlined in Chapter 2, work in tandem to form systems. Functionally, the parts of the Meson West spectrometer primarily used for E706 can be divided into five systems. An overview of these systems is given below.

3.1 Beamline

The Fermilab "Tevatron" accelerated protons to a momentum of 800 GeV/c. It operated on a 58 second duty cycle with the first 35 being used for accelerating the protons and the remaining 23 for extracting them. The 23 second extraction period is also refered to as a "spill". Since the Tevatron has a 53 MHz RF structure, the primary protons are delivered about 19ns apart, to the switchyard where the distribution of the particle beam to the 'proton', 'neutrino' and 'meson' experimental areas takes place. The meson area in turn has its own switchyard and it is from here that the Meson West Beamline serving E706 draws its beam.

The MWest Beamline was designed to transport both negatively and positively charged particles with momentum up to 1 TeV/c. Due to this versatility E706 could record data with a variety incident of beams. These included primary 800 GeV/c proton (1991) as well as secondary 530 GeV/c proton (1991) and pion (π^-) beams. The seondary beams were obtained by dumping the primary proton beam into a 1.14 interaction length beryllium block, 46.5 cm in length and 2.22 cm in diameter and selecting some fraction of the produced particles for transport to the spectrometer.

By the very nature of their production, the secondary beams are not composed of a single particle type. A 42.1 meter long Cerenkov counter filled with helium gas tagged the majority and minority particles in the secondary beams. The relative

Beam	-530 GeV			+530 GeV		
Particle Type	π^-	K^-	$\bar{p}$	π^+	K^+	p
Beam Fraction	97%	2.9%	0.1%	2.7%	0.5%	96%

Table 3.1 Particle Fraction in Secondary Beams

fractions of the different particles types for the two polarities of secondary beam is shown in Table 3.1.

3.2 Tracking System

E706 employs a charged particle spectrometer for the study of hadronic jets associated with direct photon production. In addition the electrons, from photon conversions, detected in the tracking system serve as a very important tool in LAC energy and position calibration.

The main expectations from the tracking system were:

- Beam track information for p_T determination
- Precise vertex determination for A-dependence studies
- Charged particle tracking and positional correlations with showers detected in the calorimeter
- Momentum determination for charged tracks

Three modules or six planes of Silicon Strip Detectors [10, 11] were used to provide beam track information. The strips of these planes were alternately aligned in the X and Y direction, starting with the X plane. Each module

therefore provides a x and y coordinate of the particle's trajectory at a particular z coordinate.

Five modules of Silicon Strip Detectors, placed downstream of the target, were used for vertex reconstruction (see Figure 3.1). The reconstruction of both the primary (beam interaction point) and secondary (from the decay or interaction of particles produced at the primary vertex) vertices was done.

Four modules of Proportional Wire Chambers [12] were used for the purpose of 3-dimensional spacial tracking of charged particles. Each module consisted of four planes (see Figure 3.2) which were oriented at -90° (X view), 0° (Y view), 37° (U view) and -53° (V view). The PWC chamber planes were composed of 0.8 mm gold plated tungsten anode wires positioned between graphite coated cathode planes. The PWC operated with a gas mixture of 79.7% argon, 18% isobutane, 1.1% isopropyl alcohol and 0.1% freon.

Since the charge and momentum of a charged particle can be determined by observing its behaviour in a magnetic field, a dipole electromagnet delivering a 450 MeV/c p_T impulse was installed between the SSD and PWC systems. The bending angle in the field and hence the momentum of the particle was measured by correlating tracks from the SSD system with those from the PWC system.

To improve the resolution of the tracks reconstructed downstream of the magnet, two Straw Tube Drift Chambers [13] were used. Each of the Straw Tube Chambers had X and Y modules with four planes of drift tubes in each module. The chambers had individual tubes made of aluminized mylar with gold plated tungsten wires running through their centers. They were filled with a mixture of argon ethane gas bubbled through ethyl alcohol at 0°C.

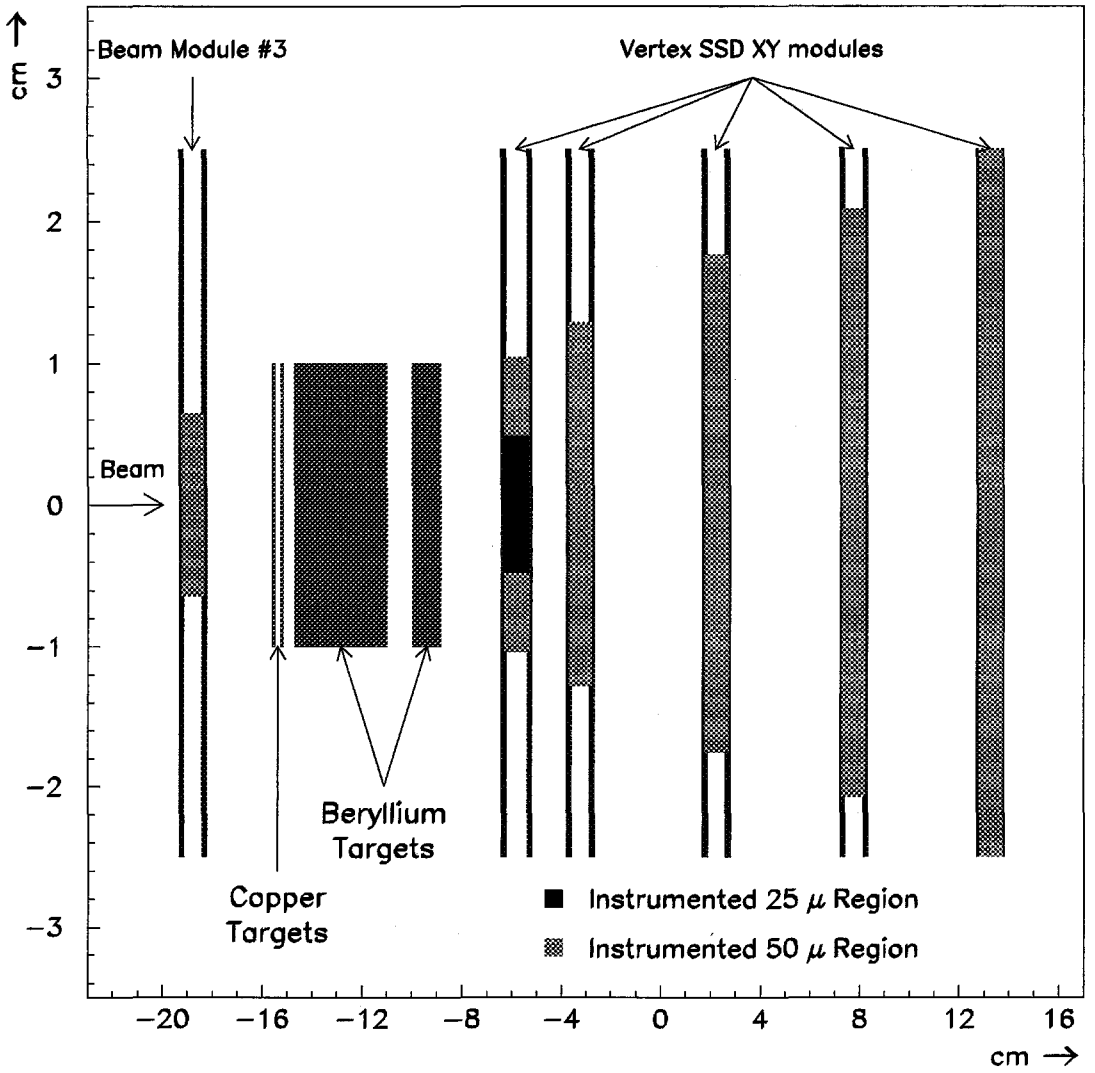

Figure 3.1 The SSD system and target region.

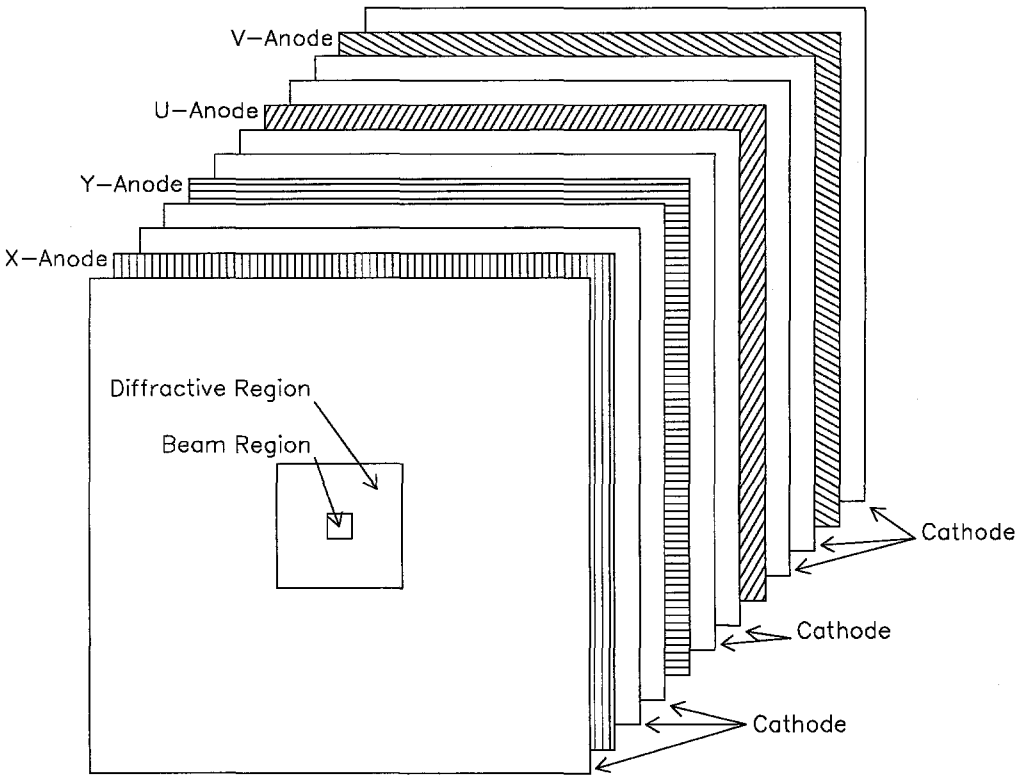

Figure 3.2 The PWC system showing the relative orientations of the X, Y, U and V planes.

3.3 Calorimetry

In order to study and measure the momentum and energy flows in any given event, E706 utilized two specialized calorimeters:

- The Liquid Argon Calorimeter (LAC)
- The Forward Calorimeter (FCAL)

The FCAL was designed to estimate the energy and momentum of the forward jet (fragmentation products of non-interacting partons) while the LAC was responsible for the energy and position determination of photons, electrons and hadrons produced in the interaction.

The LAC [14] consisted of two distinct devices:

- The Electromagnetic Calorimeter (EMLAC)
- The Hadronic Calorimeter (HALAC)

Both the EMLAC and HALAC were suspended from a mobile support or gantry and enclosed in a 17 foot wide, 21 foot deep, cylindrical, stainless-steel cryostat (see Figure 3.3), which was filled with approximately 17000 gallons of liquid argon, kept cool by boiling off liquid nitrogen. The cryostat cap made from mild steel (17 feet in diameter and 6 feet high) housed the cryogenic piping, LAC high voltage distribution system and parts of the calorimeter and trigger readout electronics. Portholes placed around the cap took care of the rest of the cabling and readout needs. Due to the cylindrical geometry of the cryostat, there was a space between its walls and the flat face of the calorimeter. A filler vessel made from 1.6 mm steel shell and filled with low density foam was inserted in this volume to displace argon and thereby reduce showering in the uninstrumented region of

the LAC. The calorimeters had holes down the center to allow the passage of beam that did not interact in the target as well as the beam jets. A 'beam filler vessel' (a steel pipe filled with helium running from the downstream end of the front filler vessel to the downstream end of the cryostat) was installed in this beam hole to reduce showering from the passage of those particles through the calorimeter. The whole cryostat was thermally isolated from its surroundings by encasing it in insulating and fire-proofing materials.

3.3.1 EMLAC

The EMLAC (see Figure 3.4), located 9 meters downstream of the target, had an annular shape with an inner radius of 20 cm and an outer radius of 165 cm. It was a sampling calorimeter with liquid argon as the active medium and lead as the absorber. Liquid argon was chosen as the active medium for its high rate capability, reasonable stability and good energy resolution. The choice of lead as the absorber was dictated by the fact that lead has a small radiation but a large interaction length which enhances the difference in the longitudinal shower development of electromagnetic and hadronic particles.

Structurally the EMLAC was divided into four equivalent quadrants. Each quadrant consisted of 33 cells along the Z axis where a 'cell' is defined to be:

- 0.082 inch Lead sheet
- 0.0975 inch Liquid Argon gap
- 1/16 inch copper clad G-10 R board
- 0.0975 inch Liquid Argon gap
- 0.082 inch Lead sheet

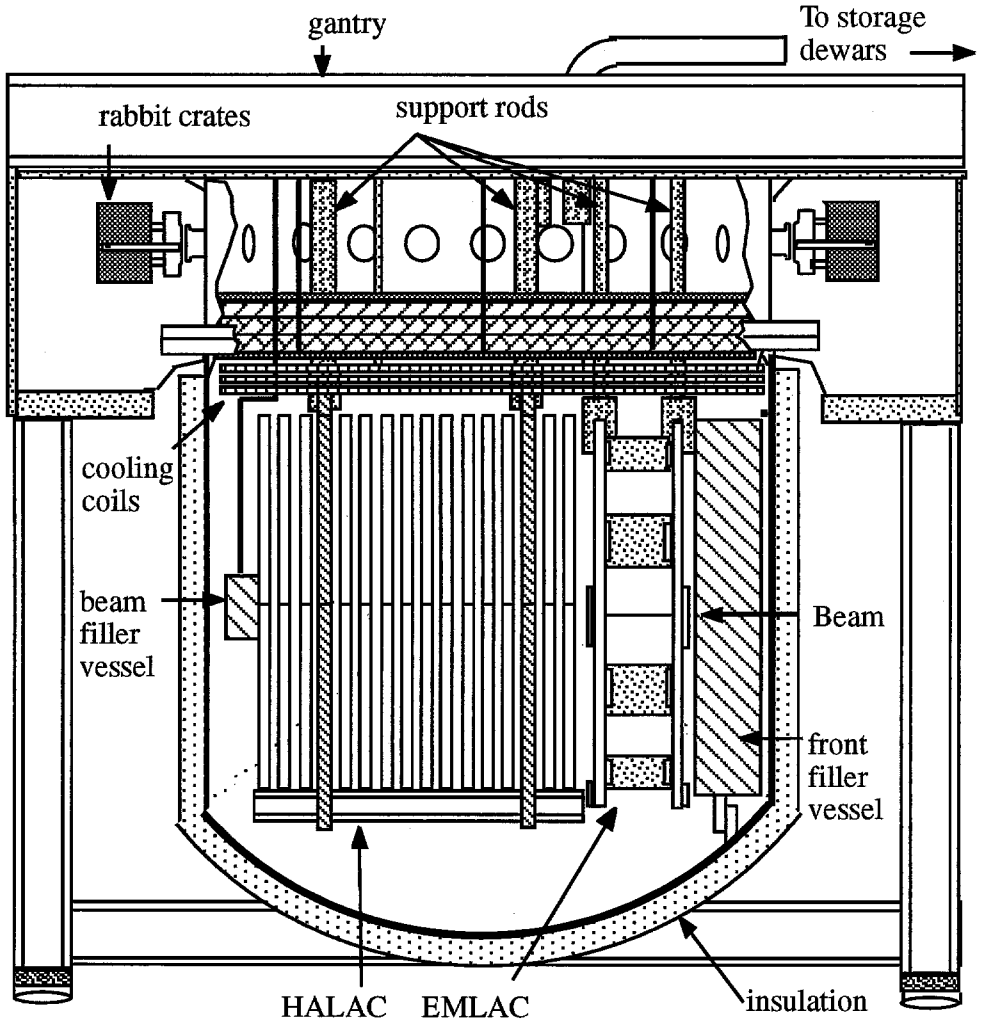

Figure 3.3 A side view of the LAC.

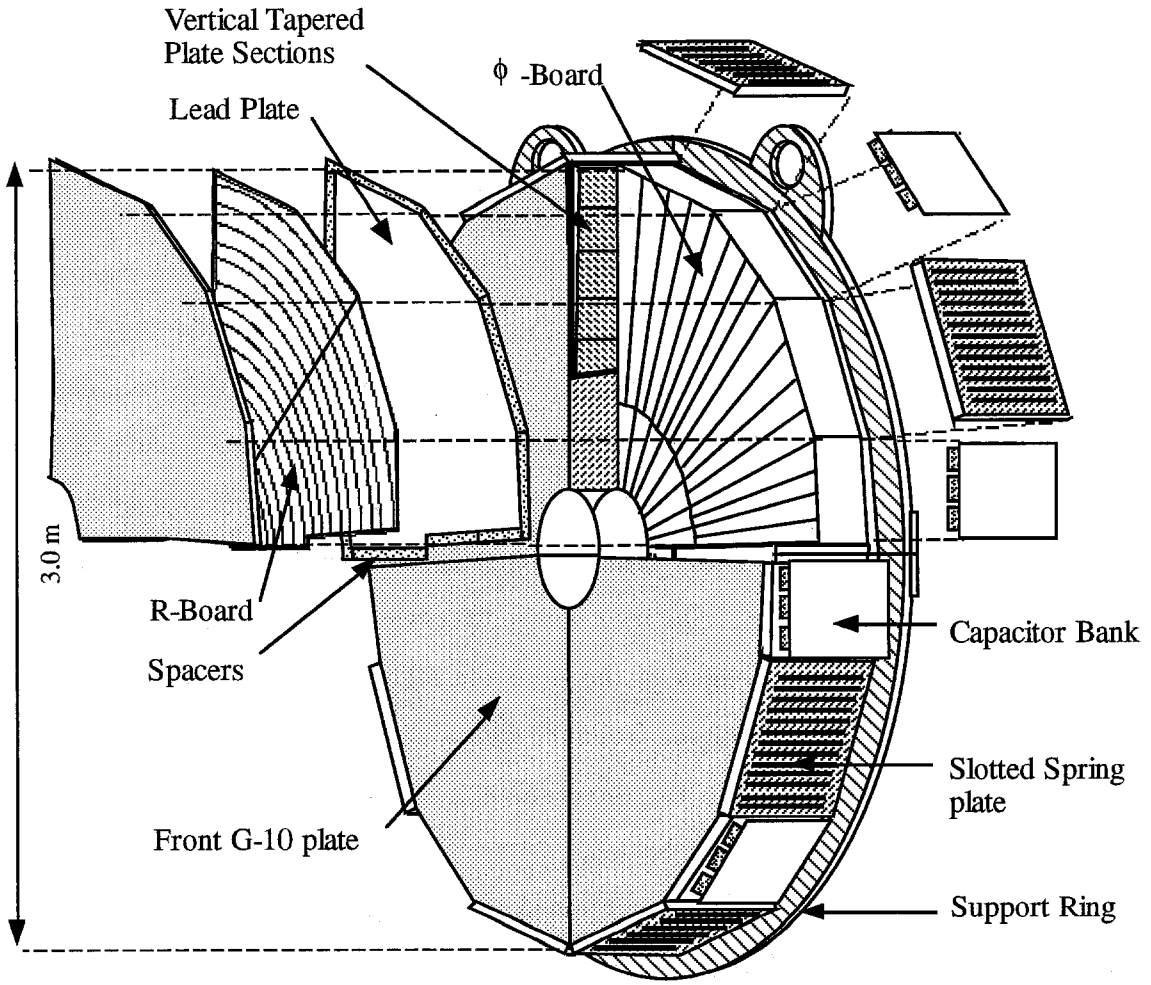

Figure 3.4 A exploded view of the EMLAC

- 0.0975 inch Liquid Argon gap
- 1/16 inch copper clad G-10 ϕ board
- 0.0975 inch Liquid Argon gap

The R and ϕ boards served as anodes while the lead sheets were the cathode. The difference between the R and ϕ boards was the way in which copper was cut to form strips (see Figure 3.4). The R strips were arcs of concentric circles of increasing radius focused on the target. There were a maximum of 254 strips per R-board with the width of the strips on the first R-board being 0.5466 cm. The strip width on sucessive R-boards was increased such that a particle originating in the target region would pass through the same R-strip for each R-board. The ϕ boards were divided into an inner and outer section. The inner-ϕ strips subtended an angle of $\pi/192$ radians while the outer-ϕ strips subtended an angle of $\pi/384$ radians. The division of ϕ strips into inner-outer was done to avoid too narrow or too wide strips at the edges of the detector. This segmentation into strips was used to resolve both photons from the decay of mesons such as π^0 or η and thereby reduce background to the direct photon signal. R-ϕ was chosen as the geometry for this segmentation because it provides a natural coordinate system for the quick estimation of the p_T contained in an event. This feature is essential for selecting a sample rich in high p_T events with minimal deadtime.

For R-strip readout purposes corresponding strips from the first 11 cells (front section) of each octant (half quadrant) were joined together using connector strings. Cells 12 to 33 (back section) were readout in a similar fashion. (This front/back divide helps in resolving closely spaced photons and discriminating against hadrons and muons.) The front and back section connector strings were attached to readout boards which transported the signals via low impedence cables

to LAC amplifier cards or LACAMP's. The LACAMP's provided three types of output: a fast energy measurement (for use in the trigger), a longer-timescale precision energy measurement and a measurement of the shower time-of-arrival via the Time to Voltage Converters. ϕ-strip readout was carried out in the same way except that instead of being done for each octant it was done in the front and back for an inner and outer section.

3.3.2 HALAC

The hadron calorimeter used steel as the absorber material and liquid argon as the active medium. The HALAC had a depth of 8 interaction lengths and was divided into 53 sampling cells or 'cookies' interspersed by 2.54 cm thick steel plates. Like the EMLAC, the HALAC was also divided into a front and back section with 14 cells in the front and 39 in the back.

A typical 'cookie' consisted of a 0.8 mm thick copper clad G-10 board, for which the upstream copper layer was grounded and the downstream was at a high voltage, followed by readout board with triangular readout pads (see Figure 3.5) facing the HV. The charge collected on the pads was read out by a set of traces running between the row of triangles. The pads were focussed on the target and those covering the same solid angle were read out as a single channel for the front and back separately.

3.3.3 FCAL

The Forward Calorimeter consisted of acrylic scintillator as the active medium and steel as the absorber. It could be divided into three identical modules (see Figure 3.6). Each module consisted of 32 scintillator and 32 steel plates, 45 inches in diameter. Holes were punched through these plates and wave shifter rods inserted in them. These acrylic rods redirected the light generated in the

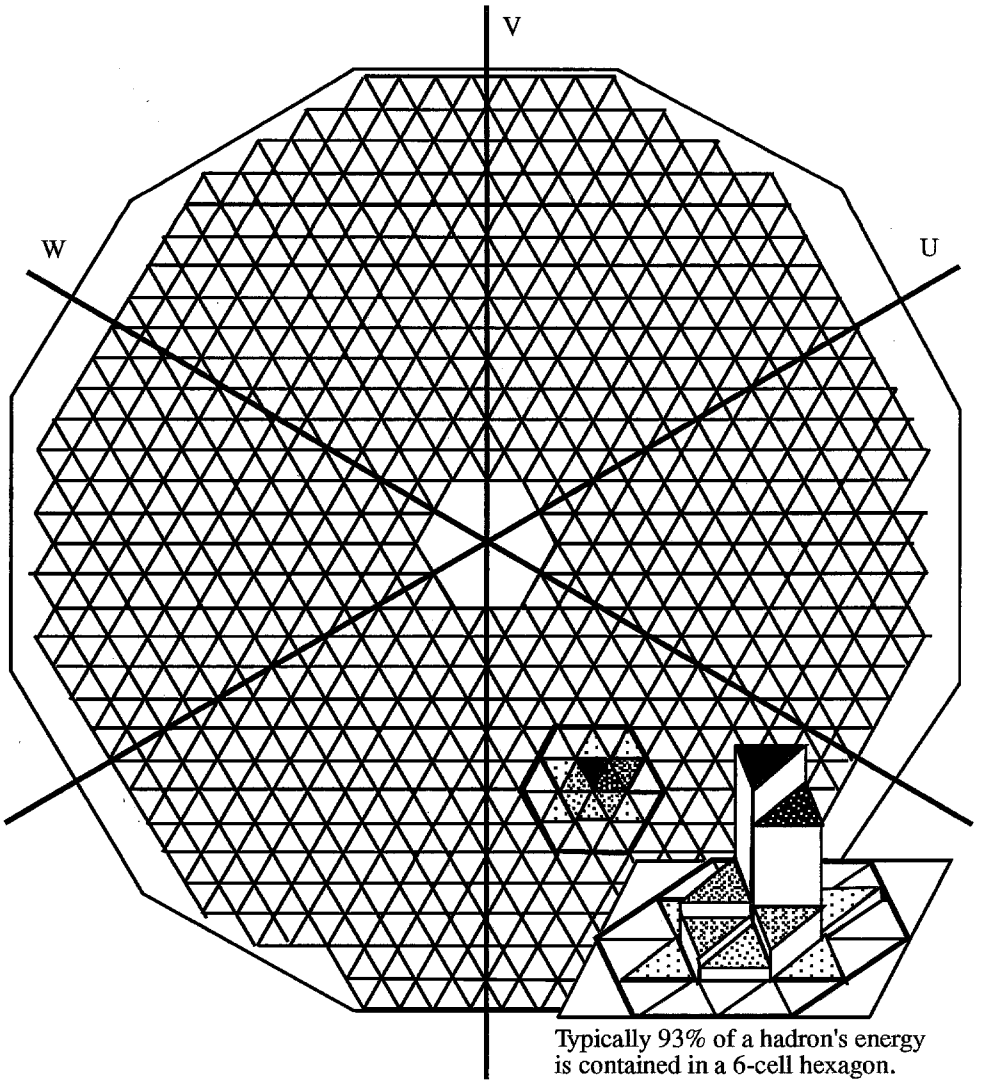

Figure 3.5 The pad structure of the HALAC.

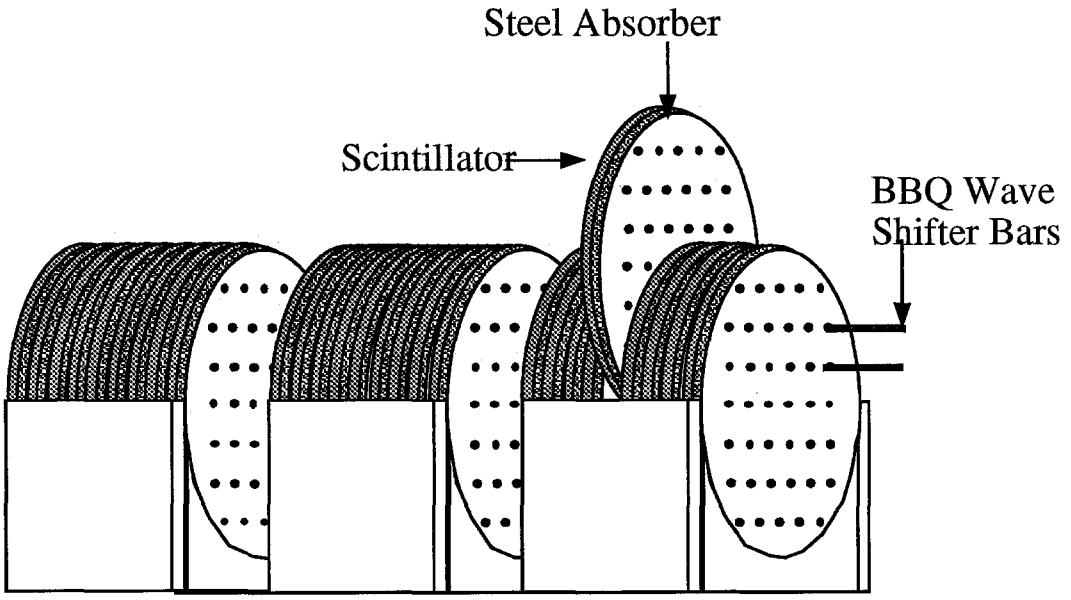

Figure 3.6 The forward calorimeter.

scintillator to the front and back of the module to be read out by photomultiplier tubes. The rods were doped by an organic dye which shifted the blue light, produced due to the passage of particles through the scintillator, to green for which the phototubes had a better efficiency.

3.4 Trigger System

High p_T interactions are a relatively rare occurence. Thus any experiment studying high p_T particle production must sort through a huge amount of data to find the few rare events of interest. Furthermore, to accumulate a reasonable sample of such rare events rapidly, the spectrometer must be capable of handling high interaction rates. This however causes two problems. First the amount of data generated can become cumbersome to handle both online and offline.

Secondly the very high rate of the interactions (most of which will be low p_T) could produce large dead times in the data acquisition system.

A pragmatic response to this challenge is to implement a trigger. A trigger system sifts through the interactions and selects only those which are potentially of interest to the experiment. This not only implies managable sizes for data samples but also more live time for the data acquisition systems as even with a high rate of interaction it only has to latch and read out information for the few events of interest.

For E706, the formation of a trigger [15] was divided into four distinct steps:

- Beam definition
- Interaction definition
- Pretrigger definition
- Trigger definition

$$\boxed{\text{BEAM} = \text{BEAM1} \otimes \overline{\text{BH}} \otimes \text{BM\_GATE} \otimes \text{RF\_CLOCK}}$$

where:

BEAM1 : presence of a beam particle as signified by a hit cluster in at least two of the three hodoscope planes and absence of multiple beam particles in the same bucket as signified by not more than one plane registering multiple hit clusters.

$\overline{\text{BH}}$: beam particle centered on the target and beam SSD system as signified by no hits in the beam hole counter.

BM_GATE : indicated the possibility of beam in the beamline (provided by the accelerator)

RF_CLOCK : pulser running at 53MHz, simulating beam structure

$$\boxed{\text{INTERACTION} = \text{BEAM} \otimes \text{INT} \otimes \text{CLEAN} \otimes \text{COMP\_RDY}}$$

where:

INT : presence of an interaction as signified by hits in at least two of the four interaction counters.

CLEAN : non-occurence of interactions within ± 3 buckets of the given INT.

COMP_RDY : computers are ready to accept the event if triggered.

$$\boxed{\text{PRETRIGGER} = \text{INTERACTION} \otimes \text{PTMIN} \otimes \overline{\text{EARLY\_PT}} \otimes \overline{\text{VW}} \otimes \overline{\text{SCRKILL}}}$$

where:

PTMIN : at least one octant has a p_T deposition of 1.7 GeV/c or greater. The p_T for the octant was determined by summing up the p_T's for each strip.

$p_T^{octant} = \sum_{strips} E_i \sin\theta_i \approx E_i \times R_i / Z_{LAC}$

E_i is the energy measured in the i^{th} strip

R_i is the radius of the i^{th} strip

Z_{LAC} is the distance from the target to the front face of the LAC (9 meters)

$\overline{\text{EARLY\_PT}}$: no significant p_T deposition detected in this octant in the preceeding 200ns

$\overline{\text{VW}}$: no hit registered in the veto wall covering the octant.

$\overline{\text{SCRKILL}}$: no noise spike generated by the LAC power supplies.

After the pretrigger signal was generated the system checked to see if any of the trigger definitions had been satisfied. The triggers could be placed into three categories:

- Local: p_T of a contiguous group of 16 strips above a given threshold. Examples were the Single Local High trigger with a threshold of $\approx$ 4 GeV/c and the Single Local Low trigger with a threshold of $\approx$ 2.75 GeV/c.

- Global: p_T of the sum of all strips in a given octant above a given threshold Examples were the Global High trigger with a threshold of $\approx$ 4 GeV/c and the Global Low trigger with a threshold of $\approx$ 3 GeV/c.

- Prescaled: Mainly beam and interaction triggers so as to provide a sample of low bias data.

3.5 Data Acquisition System

Once an event had been selected by the trigger, it was the responsibility of the Data Acquisition System [16] to collect and concatenate raw data from the various sub-systems of the Meson West spectrometer. The central unit or host node of this Data Acqusition System was a DEC 3200 Vaxstation that communicated with three DEC PDP-11 mini-computers and the FASTBUS system. One of the PDP-11's was devoted to the trigger readout, the PWC's, SSD's and scalers and the other two PDP-11's handled information from FCAL and the downstream muon identification system. The LAC and STRAW event information was channelled through the FASTBUS system. The data collected by the PDP-11's and the FASTBUS system was then concatenated by the host node and written to a 8 mm magnetic tape as one event.

Chapter 4 Event Reconstruction

MAGIC, written in Fortran-77 and using the ZEBRA memory management and PATCHY code management package was the main steering routine of the E706 event reconstruction package. It had the ability, by way of calling the relevant subroutines, to read, unpack, reconstruct and write out data or Monte Carlo events. An important feature of the MAGIC reconstruction program was its flexibility. One could just unpack the data and not reconstruct it, call one reconstructor and not the others, write out raw or fully reconstructed events. These different options were controlled by a set of user selected 'control cards'. To further increase its versatility 'hooks' or interfaces were provided in the code to accomodate user specific routines and tasks.

The six main reconstruction packages or reconstructors, which could be called independently of each other by MAGIC, were:

- EMREC: Reconstruction of shower energy and position in the EMLAC
- PLREC: Vertex and charged track reconstruction
- DLREC: Trigger and Cerenkov logic reconstruction
- HCREC: Reconstruction of shower energy and position in the HALAC [17]
- FCREC: Recontruction of shower energy in the FCAL [18]
- MUREC: Reconstruction of tracks in the downstream muon spectrometer

4.1 Electromagnetic Shower Reconstruction

For reconstruction purposes each quadrant was treated independently. Furthermore each quadrant was organized into views (left R, right R, inner ϕ and outer ϕ) each of which was treated in three sections (front, back and sum).

4.1.1 Unpacking

The first task was to unpack the raw data. This basically meant mapping the data from the crate-amplifier format to the quadrant-view-section-strip format. At this stage what existed was the ADC count associated with each channel. This ADC count was converted to the detected energy as follows,

$$E^i = A^{em} G^i (N^i - N_0^i)$$

where:

- A^{em} is the normalization factor as determined from electron calibration data (3.1 MeV/count)
- G^i is the gain of the amplifier channel i
- N^i is the digitized value or ADC count of the pulse height for channel i
- N_0^i is the pedestal value for channel i

N_0^i or the pedestal value for any particular channel is the ADC count detected by that channel in the absence of any shower or energy deposition in its neighbourhood. In other words, pedestals represent the response of the channels in the absence of a signal. These pedestals were measured individually for each

channel, due to potentially different noise levels from one channel to the other, in a two step process. Initially the pedestals were determined between spills roughly once every eight hours using pulser trigger. But due to differences in sampling rates and pile up effects observed in data, the pedestals were later refined using prescaled beam events. The prescaled beam events were chosen since they typically did not have significant shower activity in the EMLAC.

4.1.2 Groups and Peaks

The reconstruction program now searched for clusters of energy deposition or 'groups' in each of the views. A group was defined to be any cluster which had;

- At least 3 neighbouring strips with energies above 80 MeV (2 with energies greater than 95 MeV for outer ϕ)
- A total energy of at least 600 MeV
- At least one strip with energy greater than 300 MeV (350 MeV for outer ϕ)

Once all the groups had been identified, the position of 'peaks' within the group was evaluated. A peak is the point at which the derivative of the energy distribution changes sign. More specifically what the program searches for is a maximum (peak) bounded by two minima (valleys) as it scans each group from left to right. This peak finding is first attempted in the sum section and then done separately for the front and back sections. Determining the peak in the front section independent of the sum section serves two purposes. First, it allows one to see if what appears as a single peak in the summed section actually consists of one or possibly more showers. Secondly, one can form the ratio;

$$\mathrm{E_{front}/E_{total}} = \frac{\text{peak energy in the front section}}{\text{peak energy in the sum section}}$$

where energy (front or sum) is defined as the sum of strip energies between the valleys. Since this ratio gives an average measure of the longitudinal shower profile it can be used to discriminate against hadrons and muons. It also provides a projection in which data and Monte Carlo can be compared in an effort to tune the shower development in the Monte Carlo to the data. If, in addition to the 'front peak', the position of the peak in the back section is also known, a variable called 'directionality' can be defined as:

$$\delta = R_f - \frac{Z_f^{LAC}}{Z_b^{LAC}} R_b$$

where:

- R_f and R_b are the front and back radial positions of the shower respectively.
- Z_f^{LAC} and Z_b^{LAC} are the z-coordinates of the first EMLAC cell in the front and back sections respectively.

Directionality provides discrimination against muons (see sec. 7.1.4).

4.1.3 Gammas

Single view photons or 'gammas' are reconstructed from these peaks by fitting a predetermined parametrized shower shape. The energy of the gamma is then given by the integral of the fitted shower shape. The shape itself was derived from a Monte Carlo simulation, by studying the energies deposited in the strips versus their distance from the center of the shower, for a set of isolated photon showers. Initially this shape determination was done separately for the front and back sections;

$$S_{front}(r) = \frac{1}{r}(f_1 e^{-f_2 r} + f_3 e^{-f_4 r} + f_5 e^{-f_6 r})$$

$$S_{back}(r) = b_1 e^{-b_2 r} + b_3 e^{-b_4 r} + b_5 e^{-b_6 r}$$

where r is the distance from the center of the shower.

The sum section shower shape (see Figure 4.1), the one used by the program to evaluate the shower energy, was then defined as:

$$S_{sum}(r) = 0.7 S_{front}(r) + 0.3 S_{back}(r)$$

This fitting process is unambiguous for groups having single peaks and the best estimate of energy of the shower is deemed to be one which minimizes a 'chisquare' defined in this case as:

$$\chi^2 = \sum_i \frac{(e_i - z_i E)^2}{{\sigma_i}^2}$$

where:

- the sum goes from the first to the last strip of the group
- e_i is the energy detected by the i^{th} strip
- z_i is the fraction of the shower energy contained in strip i as estimated by the shower shape
- σ_i^2 is the expected EMLAC resolution for that signal

For 'multiple peak' groups, a global fit is done first and then the constituent shower position and energies are estimated by a slightly modified chisquare minimization process:

$$\chi^2 = \sum_i (1/\sigma_i{}^2)(e_i - \sum_j E_j z_{ij})^2$$

where:

z_{ij} is the fraction of the shower energy from shower j contained in strip i as estimated from the shower shape and the χ^2 minimization determines the individual shower energies E_j.

4.1.4 Photons

R and ϕ view gammas are now correlated to form the final 'photons'. The basic strategy is to match the gammas from each view based on the energy and the longitudinal shower profiles. This technique is appropriate because the R and ϕ boards are interleaved in the detector and thus the energy and shower development in both R and ϕ should be very similar. The division of the EMLAC into different views reduces the potential combinations. Inner ϕ gammas are only correlated with r-view gammas that have radii less than 40 cm while outer ϕ gammas are only correlated with r-view gammas having radii greater than 40 cm.

Because of the potential for overlap of showers in a single view a number of 'correlation types' [19] were investigated. The simplest and the most frequently encountered type was the one to one (1-1) case in which one R-gamma was matched to one ϕ-gamma to form a photon. The 2-1 and 1-2 correlations arose when two gammas which were separate in one view (say the r-view) overlapped

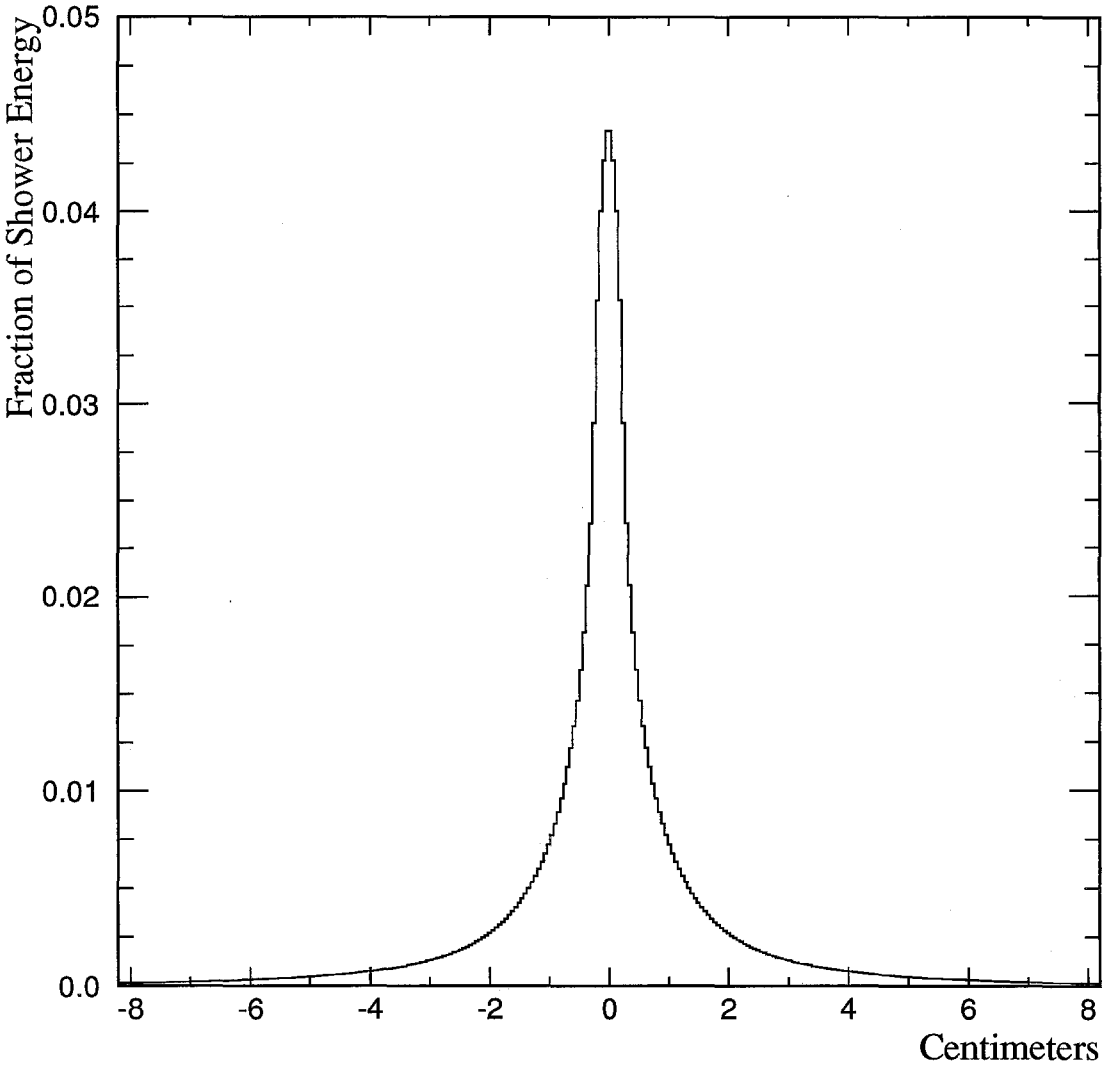

Figure 4.1 The EMREC shower shape.

in the other (ϕ view). In such situations, the reconstructor used the energies of the r-view gammas to split the ϕ-view gamma into two. An analogous procedure was invoked when the gammas overlapped in the r-view but were separated in the ϕ view. Higher order correlations accomodated instances when the gammas happened to fall near the inner/outer ϕ or octant boundaries. Once gammas were correlated they were removed from the subsequent correlation process and the resultant photon information was stored in the data banks.

4.2 Track Reconstruction

The hits detected in the various tracking chambers are used to reconstruct the charged particle tracks as described below [20];

4.2.1 Beam Tracking

The reconstruction of incident beam tracks was performed independently in the X and Y views using the information from the three upstream SSD chambers. The first stage was identifying all 3-hit beam tracks. Hits from the most upstream and downstream beam chambers were used to define candidate track segments which were projected to the middle plane to determine whether there was a hit in that plane within 75μ of the projected segment. A least-squares fit was then done for all such 3-hit combinations and if the χ^2/DOF was < 3, the track was accepted as a legitimate beam track. Once all such 3-hit tracks had been identified, a search was made for 2-hit tracks after removing all hits associated with the 3-hit beam tracks. These beam tracks (2 or 3-hit) measure the trajectory of the incident beam particles and can be used to improve the transverse resolution of the primary vertex and to improve the p_T measurement of particles, emerging from the interaction.

4.2.2 Downstream PWC Tracking

First view tracking was performed independently in the X, Y, U and V views. Since there were four planes per view, the first and the last planes were used as seed planes and the middle two as the search planes. Candidate track segments were formed using the hits on the first and fourth planes and the middle planes were searched for hits within one wire spacing of the projected line. A view track was accepted if it had 3 or more hits associated with it and had a χ^2/DOF less then a predetermined value. Once all the 3 and 4-hit view tracks in each of the four views were reconstructed space tracking was performed. Combinations of X and Y view tracks were used to search for hits in the U and V views within 1.5 wire spacings of the position predicted by the XY pair. The procedure was then repeated, starting now with the U and V tracks. At this stage tracks with 13 or more hits and a good χ^2/DOF were accepted as 'space tracks'. Hits used in these space tracks were removed from further consideration.

View and space tracking was then repeated using the left-over hits. The only difference in this iteration was a lower minimum hit requirement (at least 11 hits for 4 planes and at least 10 hits for 3 planes). As before hits used in these tracks were excluded from further consideration. One last iteration was performed using the remaining hits. This was done to get the wide angle tracks which were clearly visible in the first two PWC modules but went outside the acceptance of the PWC system after that. For acceptance as a two-module space track there had to be at least 6 hits on the track with its Y-view pointing back to the target.

4.2.3 Straw Tracking

To improve the resolution of the downstream tracks, information from the drift tube chambers was used. The PWC tracks were projected into the STRAW planes

and the closest hit pairs were stored. A refitting of the track, using information from all 32 (PWC and STRAW) planes, was now done resulting in a more accurate determination of the space track information.

4.2.4 Upstream Tracking and Linking

The information from the X and Y planes of the five SSD modules downstream of the target were used to form upstream tracks. First to be reconstructed were the five and four-hit view tracks which were then projected to the center of the magnet. The previously reconstructed downstream space tracks were also projected to the center of the magnet. A "link" or association was established between an upstream SSD track and a downstream space track if the spatial difference in their projected positions (after accounting for the effects of the magnetic field) was within a momentum dependent window. Due to the lower number of constraints on the upstream tracking up to five SSD view tracks could be associated with a single downstream space (PWC/STRAW) track with the closest view track being called the "best link".

After all the five and four-hit SSD tracks were reconstructed, all the hits associated with those tracks were excluded from further consideration. Three hit SSD view tracking was then performed followed by linking to the PWC/STRAW tracks.

4.2.5 Vertex Finding

Vertices are first found separately in the X and Y views and then matched to determine the 3-D position of the vertex. Linked three, four or five-hit tracks are preferred for forming view vertices. At least three tracks are required. If there are not enough linked tracks available, unlinked five and four-hit tracks are also used.

Once a group of SSD tracks have been selected, the vertex position is calculated by minimizing the chisquare defined as;

$$\chi^2 = \sum_i b_i^2/\sigma_i^2$$

where:

- b_i is the impact parameter of the i^{th} track
- σ_i is the uncertainity in the projection of the i^{th} track

A success, as far as vertex finding is concerned, is declared if the χ^2 is less than 5. The tracks associated with this vertex are now removed from further consideration and vertex finding is now attempted with the remaining tracks.

4.2.6 Relinking

Once the vertex location has been established, the process of linking the upstream SSD tracks to the downstream PWC/STRAW tracks is repeated with preference given to those SSD tracks which project closest to the vertex. After relinking is finished, the physics parameters of all the tracks are recalculated and written out.

4.3 Discrete Logic Reconstruction

The Discrete Logic Reconstruction involved the manipulation of bit-packed data. This manipulation, which was done inside DLREC [21], provided information regarding the trigger logic and the Cerenkov detector. Information such as the time histories (± 7 buckets on either side of the trigger) of the status of various counters including the beam counters, interaction counters, beam

hodoscope elements, veto walls, Cerenkov phototubes and the hole counter was decoded and stored. The program also determined which octants satisfied the triggers and for which trigger type.

Chapter 5 Energy Scale

A precise and accurate calibration of the energy response of the calorimeter is essential when studying processes with steeply falling cross sections in p_T. This is because even a small uncertainity in the calibration can produce relatively large uncertainties in the magnitude and shape of the measured cross section at any given p_T (see Figure 5.1).

Since E706 had both a charged particle spectrometer and a calorimeter, two general approaches could be taken to calibrate the response of the EMLAC. One can use electrons since they are detected in the tracking system as well as the EMLAC. Their momenta can be determined from the tracking system and by projecting the track to the EMLAC one can find the shower which matches the electron. The EMLAC energy calibration now basically amounts to comparing the shower energy as reconstructed in the EMLAC to the momentum measured for the matching track by the tracking system. There are, however, certain issues involved with this procedure. The most important being that the electron shower shape does not match the photon shower shape in the EMLAC since the electrons start showering earlier than the photons. A resultant bias can therefore be introduced in the photon energies which is not acceptable since photons are the primary focus of this experiment. The second option is to use the mass of pairs of photons from meson decays to calibrate the EMLAC response directly. In this method the tracking system is primarily used to reconstruct the interaction location which is employed in the evaluation of the photon four vectors. This procedure has its complications too, since one is calibrating the energy response of the calorimeter based on the mass of the photon pair which depends not only on the energy but the position determination as well. Also, the mass measurement can be

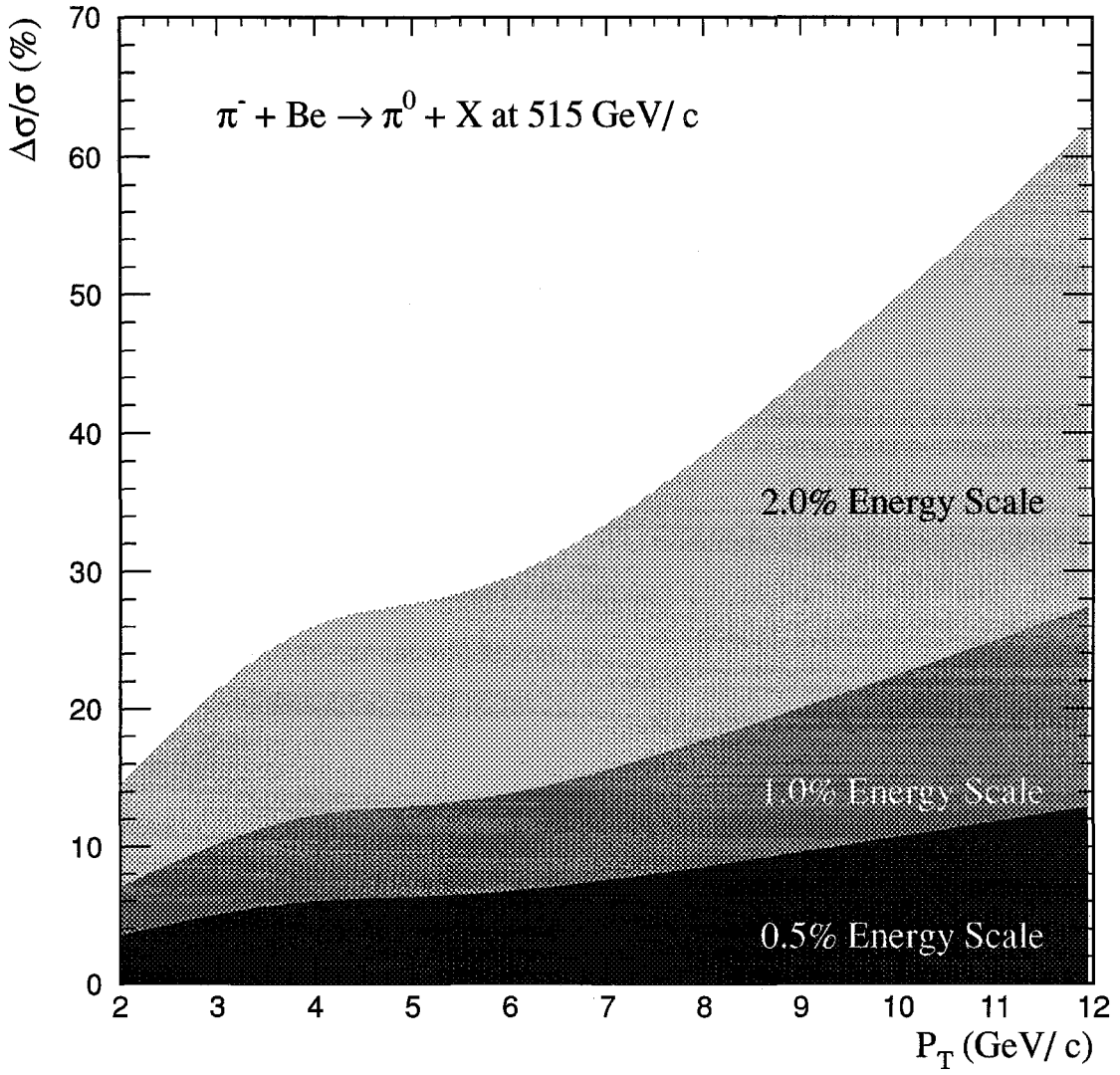

Figure 5.1 Sensitivity of the π^0 cross section to uncertainity in the energy scale.

sensitive to the degree of spatial overlap between the showers generated by the photons. Since these features were more readily studied and controlled than the features associated with the electron sample, the $\gamma\gamma$ sample was used for the final calibration of the EMLAC shower energy. The electron samples provided valuable independent cross checks on this calibration procedure.

5.1 The $\gamma\gamma$ Sample

The basic idea here was to use the π^0 and η mass constraints to calibrate the EMLAC energy response. The $\gamma\gamma$ sample was selected using the following criteria:

- Reconstructed vertex was within the target region.
- Veto wall did not fire.
- Both photons were in the "fiducial" (see sec. 7.1.2) region of the EMLAC.
- Both photons were within the same octant.
- Both photons have $E_{front}/E_{total} > 0.2$.
- The energy asymmetry of the photon pair, defined as $\frac{|E_{\gamma 1}-E_{\gamma 2}|}{E_{\gamma 1}+E_{\gamma 2}}$, is less than 0.5. This requirement was applied to reduce the background and to have comparable energy photons.

An invariant $\gamma\gamma$ mass distribution with the preceding cuts applied is shown in Figure 5.2. The π^0 and η signals are clearly visible and therefore their invariant masses can be used to evaluate the following calibration corrections [22, 23]:

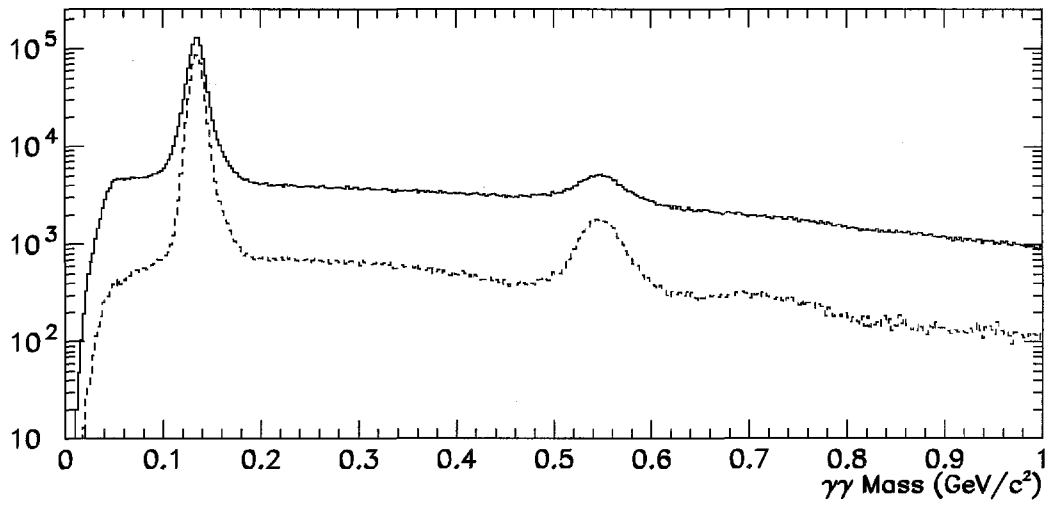

Figure 5.2 The $\gamma\gamma$ mass plot with (dashed) and without (solid) the asymmetry cut.

• Time Dependence: The uncalibrated π^0 and η masses were found to increase as a function of beam days (see Figure 5.3). The term "beam days" refers to those days on which the beam interacted in the experimental hall. Thus days corresponding to accelerator shutdowns have been squeezed from the plot since no change in the π^0 or η mass was observed across a shutdown period. Currently there is no satisfactory explanation which can account for this rise. The dependence was fitted to a curve and the energies of individual photons were adjusted based upon that parameterization such that the ratio of the reconstructed π^0 mass to its nominal value was 1.0.

• Octant-to-Octant: A preliminary octant-to-octant scale correction rescaled the reconstructed π^0 masses in each of the octants to the nominal (Particle Data Group [24]) value. The octant-to-octant variations, prior to this correction are

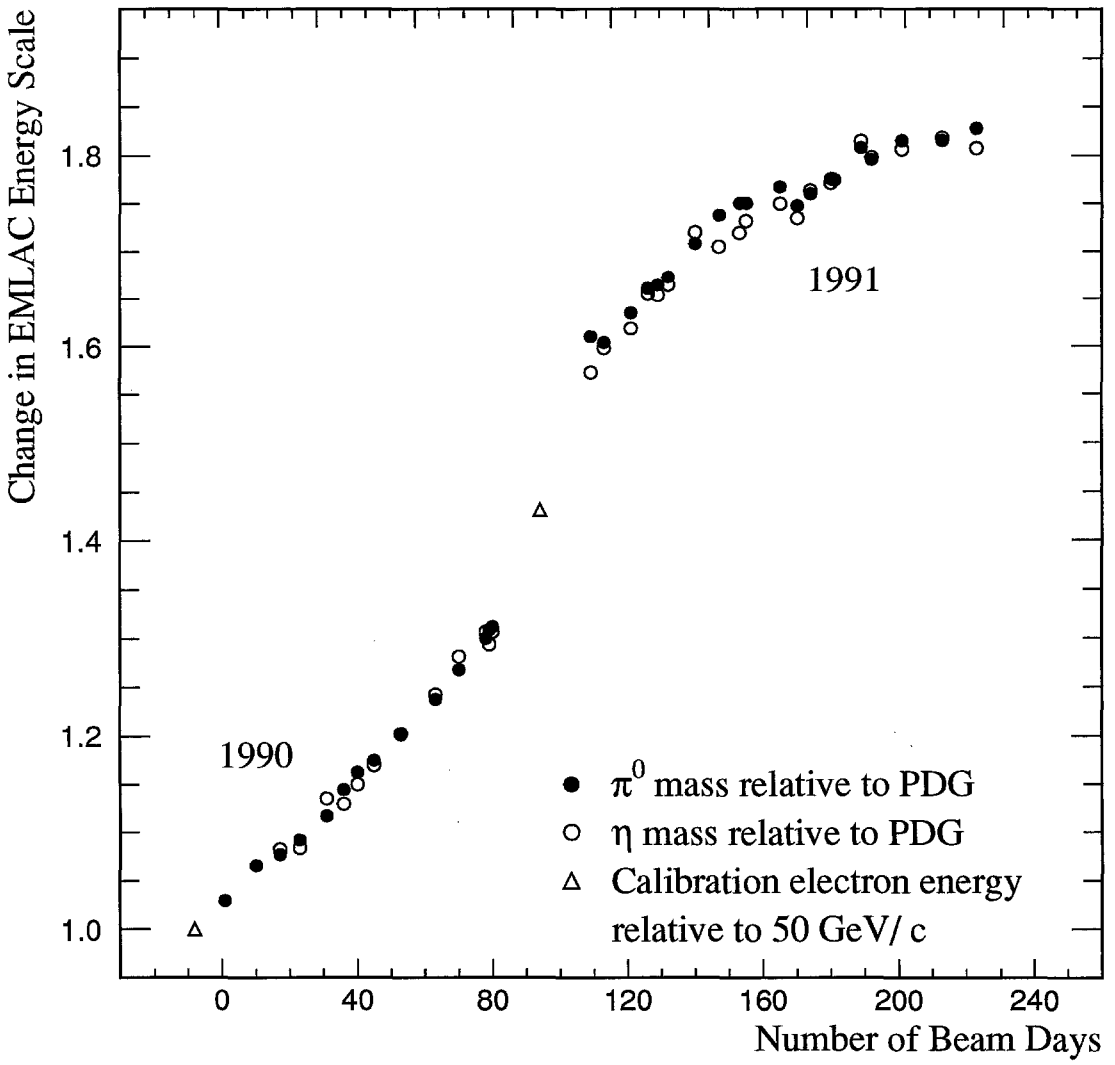

Figure 5.3 Time dependence of the uncalibrated π^0 and η masses shown here as a ratio to their standard values.

shown in Figure 5.4 and might be attributed to differences in construction (e.g. lead thicknesses) and operation (e.g. readout electronics, high voltage variations) among the octants.

• Boundary: If a photon was within ± 5 cm of the inner/outer ϕ boundary, its energy was determined using $2E_R$ rather than $(E_R + E_\phi)$ as the ϕ-view energies near the boundary are less reliable.

• ELOSS: A correction to account for energy lost due to showering in the material in front of the LAC was applied to each of the photons. This correction was determined from a Monte Carlo simulation independently for photons and electrons (see Figure 5.5).

• Radial Dependence: The radial dependence of the reconstructed π^0 and η mass is shown in Figure 5.6 where the 'radial' position of the π^0 or η refers to the energy weighted average of the R-positions of the photons of the decay. The π^0's satisfy the "Two Gamma" trigger with $p_T > 2.0$ GeV/c, while the η's are drawn from the "Single Local High" trigger sample with $p_T > 3.5$ GeV/c. A lower p_T cut is imposed on the π^0 sample so that the photons are generally well separated photons which reduces the sensitivity of the reconstructed mass to possible issues in reconstructing overlapping photons. The variation of the mass with radius is attributed to differences in shape between the calibration pulses used to evaluate the amplifier gains between spills and the actual data pulses. To correct for this, the r-dependence of the π^0 mass is parameterized individually for each of the eight octants. Based on those parameterizations the energies of showers are adjusted as a function of their radial positions.

• Octant-to-Octant: A final scale correction for each octant was evaluated using the measured η ($p_T > 4$ GeV/c) mass in each of the eight octants.

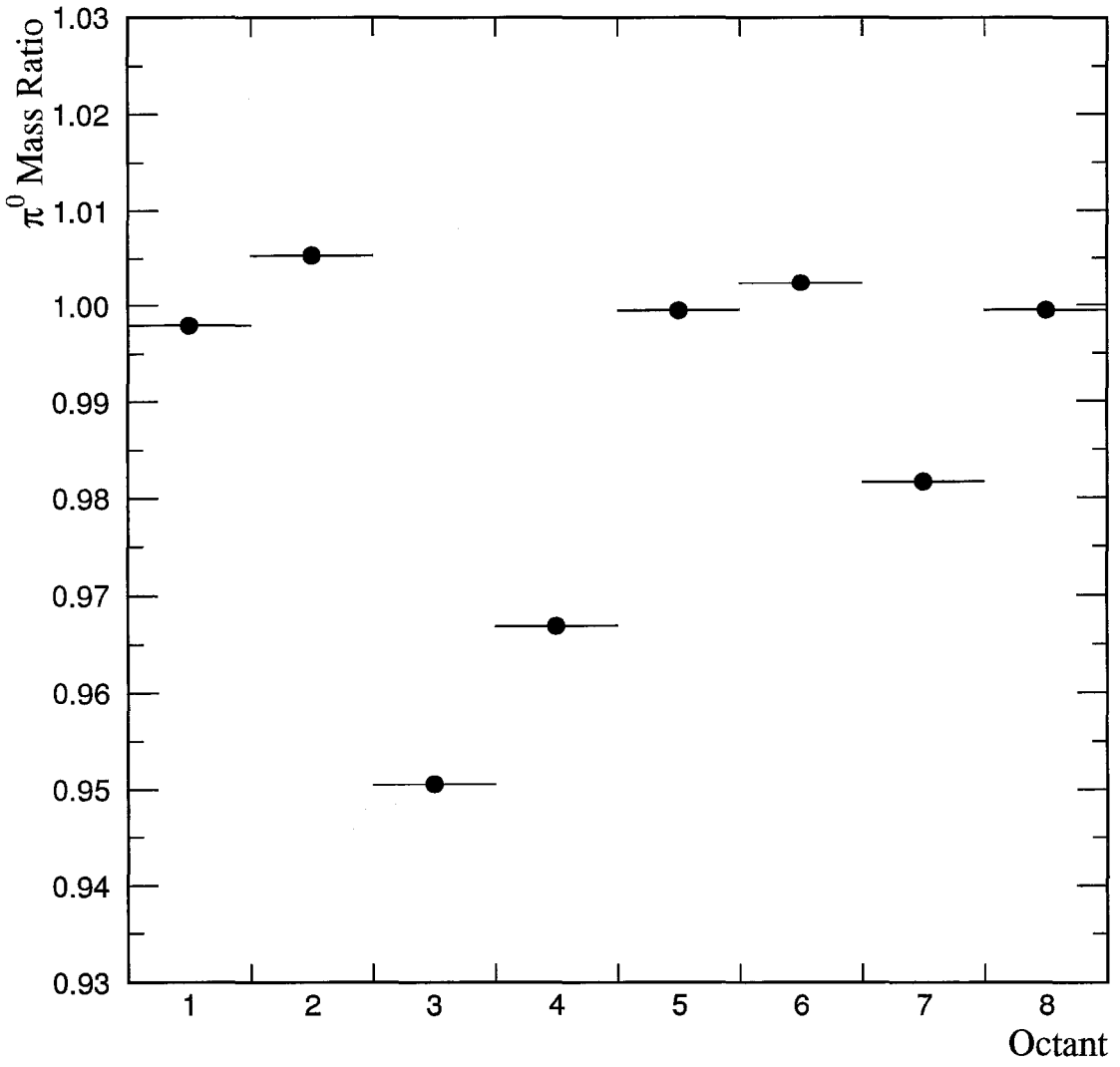

Figure 5.4 Octant to octant variations of the uncalibrated π^0 mass shown here as a ratio to its standard or PDG value.

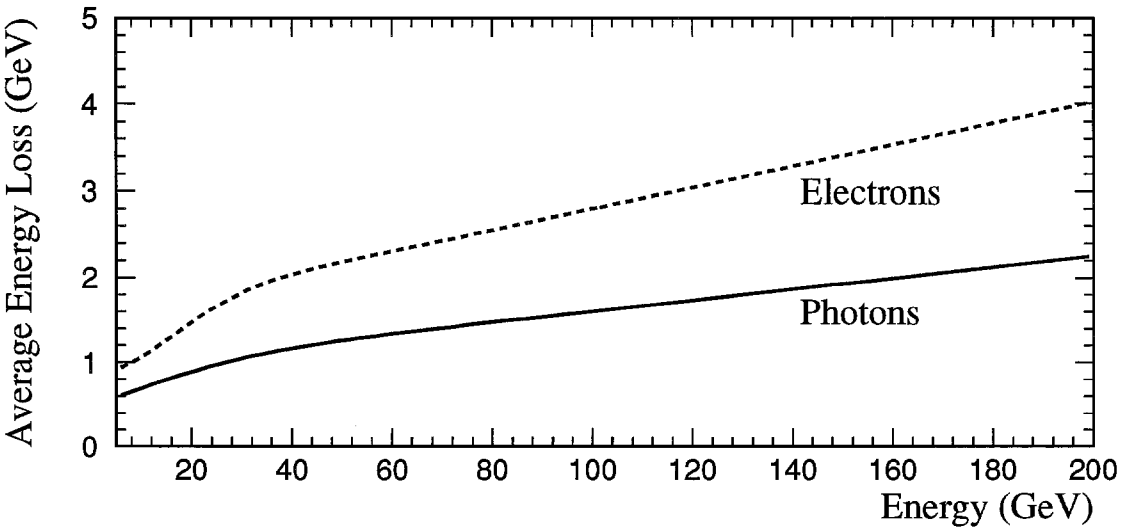

Figure 5.5 Average energy loss in the material in front of the EMLAC, for photons (solid) and electrons (dashed) as a function of their energy

From the point of view of the $\gamma\gamma$ sample the energy scale calibration process is now complete. However an independent sample can be used to study any residuals. For such an independent cross-check, E706 used the γe^+e^- sample where the idea is to select those events where one of the photons from the electromagnetic decay of a meson converts to an e^+e^- pair in its passage through matter. The γe^+e^- sample serves as a good cross-check since the kinematic variables of the electron pair can be determined by the charged particle tracking system, which means the energy and momentum of one of the photons from the meson decay can be measured independent of the EMLAC. In this case the shower shape issue associated with electrons is irrelevant since one is not using the EMLAC energy information for the electron pair.

However, to carry out this exercise, the momentum scale of the charged

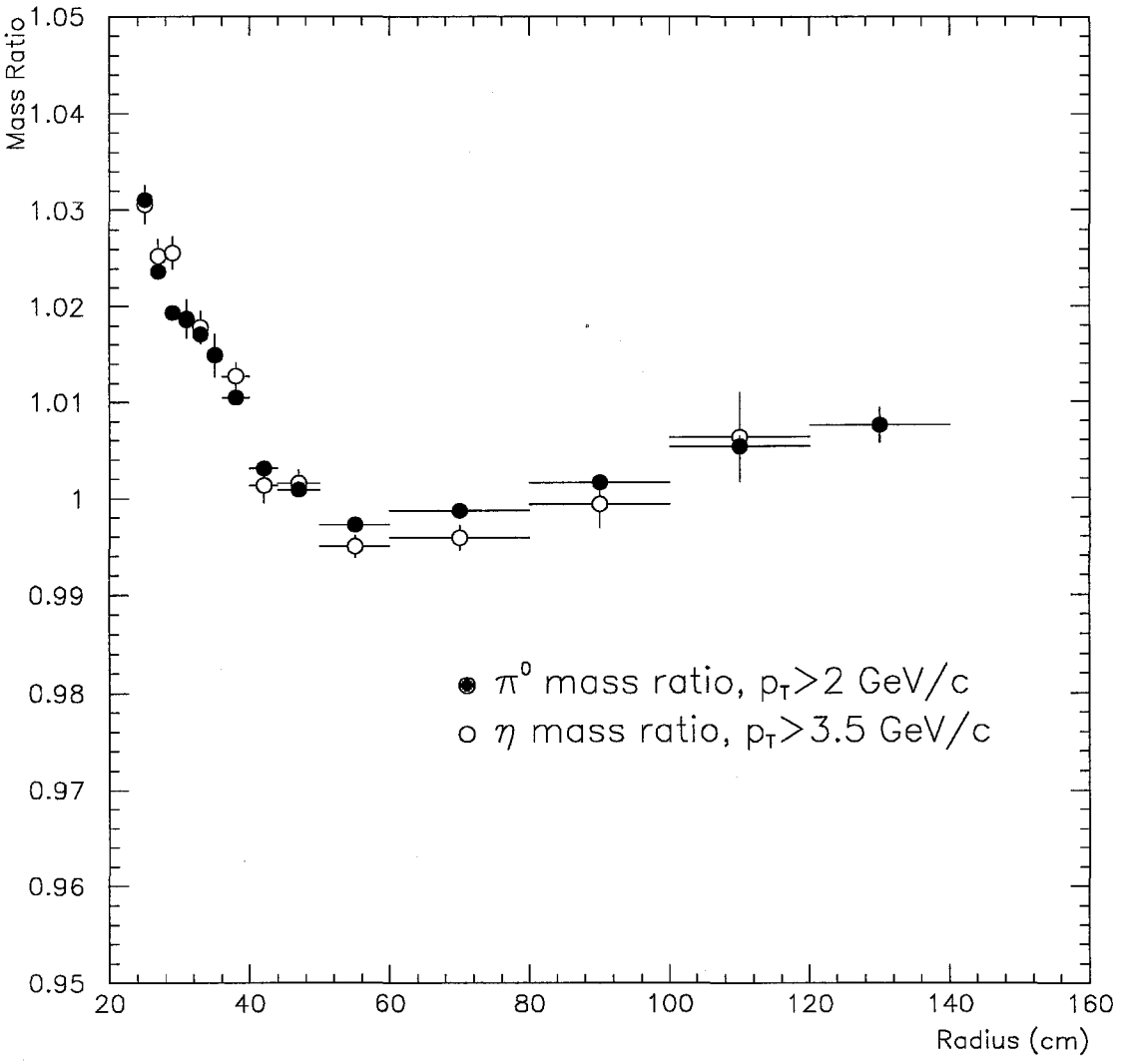

Figure 5.6 Variation of the uncalibrated π^0 and η mass versus radius shown here as a ratio to their standard values.

particle spectrometer must be calibrated. The momentum scale was calibrated using $K_s^0 \longrightarrow \pi^+\pi^-$ and $J/\psi \longrightarrow \mu^+\mu^-$ decays. The reconstructed K_s^0 and J/ψ mass peak are shown in Figure 5.7. Their values are within 0.1% of the nominal values.

5.2 The γe^+e^- Sample

A certain fraction of the time one of the photons from a meson decay will will convert to an e^+e^- pair as it passes through matter. For E706, most of the conversions occur in the target and SSD region. Due to their small opening angle, the e^+e^- pair are generally reconstructed as a single track in the SSD system. However, when they pass through the magnet, the e^+ and e^- get bent in opposite directions making them visible as separate tracks in three of the four views of the downstream PWC system. Due to the orientation of the magnetic field the bending is primarily in the X-Z plane. Thus, the conversion electrons are visible as two distinct tracks in the X, U and V views while frequently only one track is reconstructed in the Y view.

The following criteria were used to identify these conversion pairs or ZMP's (Zero Mass Pair since $2m_e << E_\gamma$):

- Oppositely charged tracks
- Similar slopes in the Y-Z plane for both tracks
- Intersection of the two tracks near the center of the magnet in the X-Z view
- Both ZMP tracks match showers in the EMLAC whose $E_{front}/E_{total} > 0.4$

A three particle (γe^+e^-) invariant mass spectrum (see Figure 5.8) is evaluated using the four momentum of the ZMP electrons (as determined from the tracking

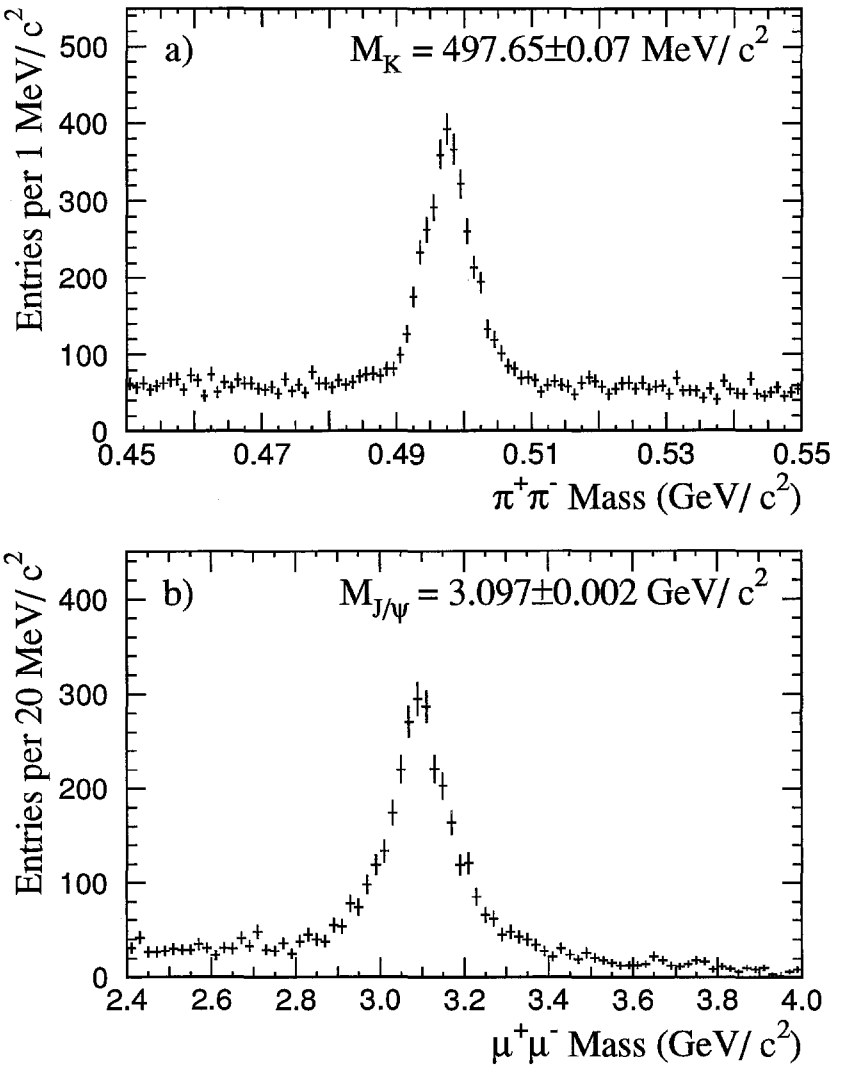

Figure 5.7 The K_s^0 and J/ψ peaks, reconstructed via the tracking system, after calibration.

system only) combined with the four momenta of each of the reconstructed showers in the EMLAC (except for those which matched the ZMP electrons). The clearly visible π^0 and η signals provide the opportunity to use this γe^+e^- sample to check for any residual corrections to the energy scale.

As indicated by the values written on Figure 5.8, the reconstructed π^0 and η mass in the γe^+e^- mode turn out to be about a percent low compared to their nominal values. This is independent of the energy of the photon (see Figure 5.9 [top]) and can be attributed to the electron energy loss due to bremsstrahlung in the target and SSD material. Evidence for this can be seen in Figure 5.9 (bottom) where the ratio of the measured mass to its PDG value is plotted for π^0's in the $\gamma\gamma$ and the γe^+e^- mode as a function of target radiation length the particles traverse. The π^0 mass from the $\gamma\gamma$ sample remains flat at one while the γe^+e^- mass shows a 2% variation over the target radiation length. This amounts to the mass in the γe^+e^- mode being a percent low when integrated over the target length as in Figure 5.9 (top).

With the one percent offset understood in terms of electron bremsstrahlung the γe^+e^- and $\gamma\gamma$ sample give consistent answers. This was interpreted to signify the absence of any significant residual energy scale corrections. Figure 5.10 shows the ratio of the η mass to its nominal value as a function of energy and p_T after all the energy calibration corrections outlined section 5.1 have been applied to its constituent photons. The ratio is flat in energy and p_T and within 0.5% of the PDG value illustrating the linearity and precision of the energy scale calibration. To independently verify the accuracy of the energy calibration the $\omega \longrightarrow \pi^0\gamma$ decay was reconstructed. Figure 5.11 shows the $\pi^0\gamma$ invariant mass distribution in the vicinity of the nominal ω mass. A clear ω signal with mass within 0.5% of the PDG value confirms the establishment of an internally consistent energy scale with less than 0.5% uncertainty.

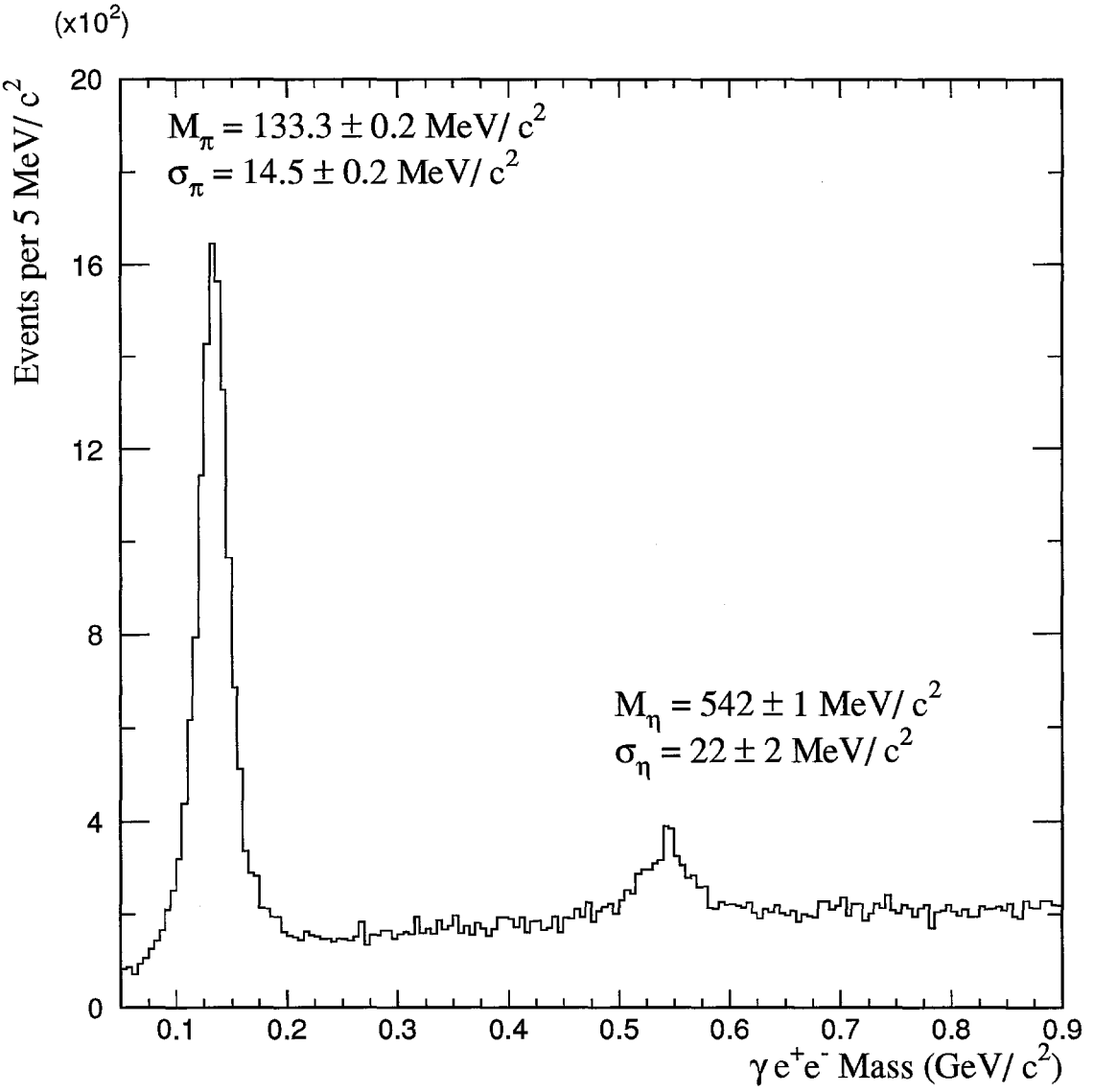

Figure 5.8 γe^+e^- invariant mass distribution. The e^+e^- four vector is determined from the tracking system while the γ four vector is from the EMLAC and has all corrections discussed in section 5.1 applied to it.

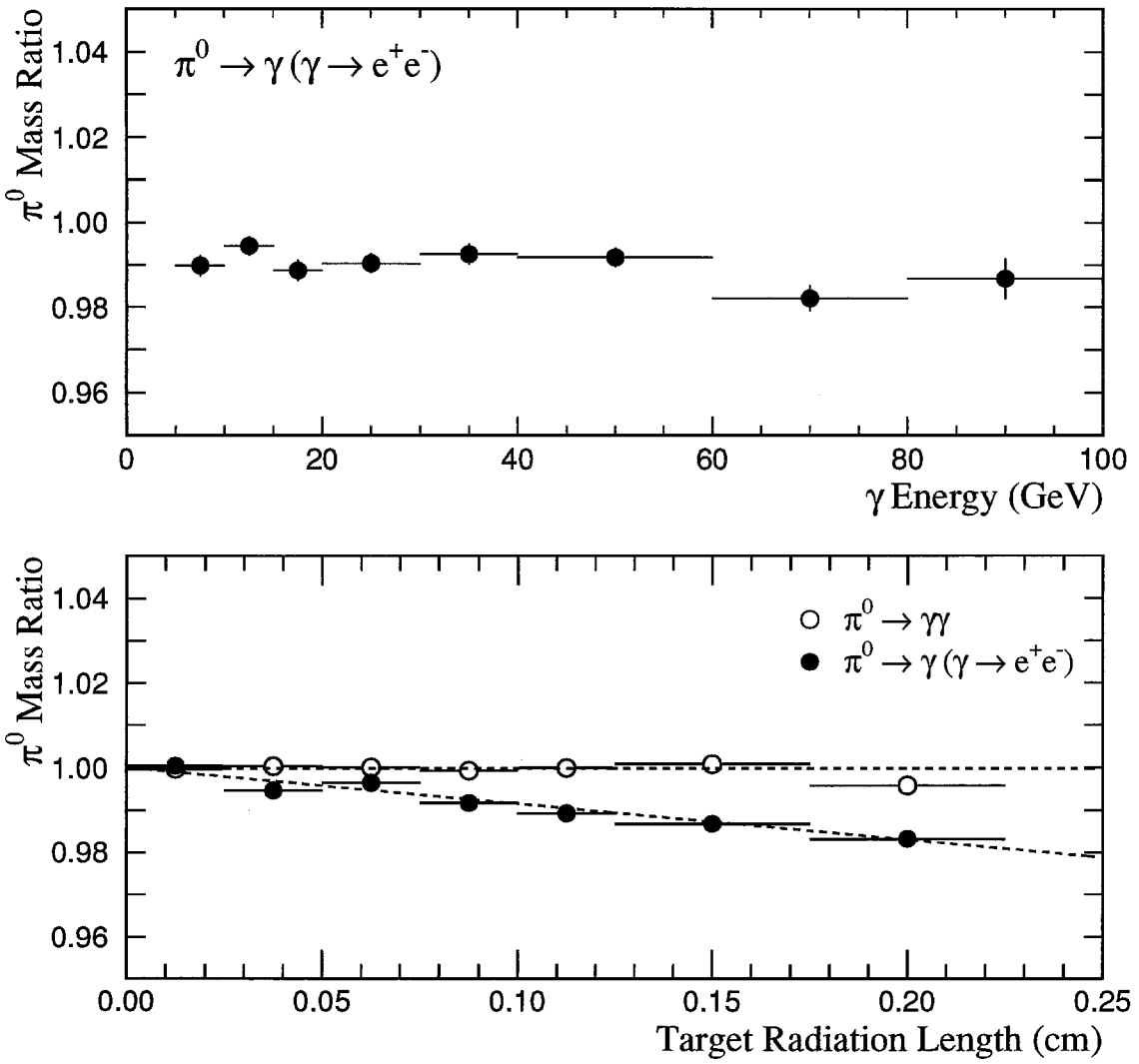

Figure 5.9 Ratio of the π^0 mass to its standard value:top) in the γe^+e^- mode versus the energy of the unconverted photon bottom) in $\gamma\gamma$ and γe^+e^- mode versus the target radiation length traversed.

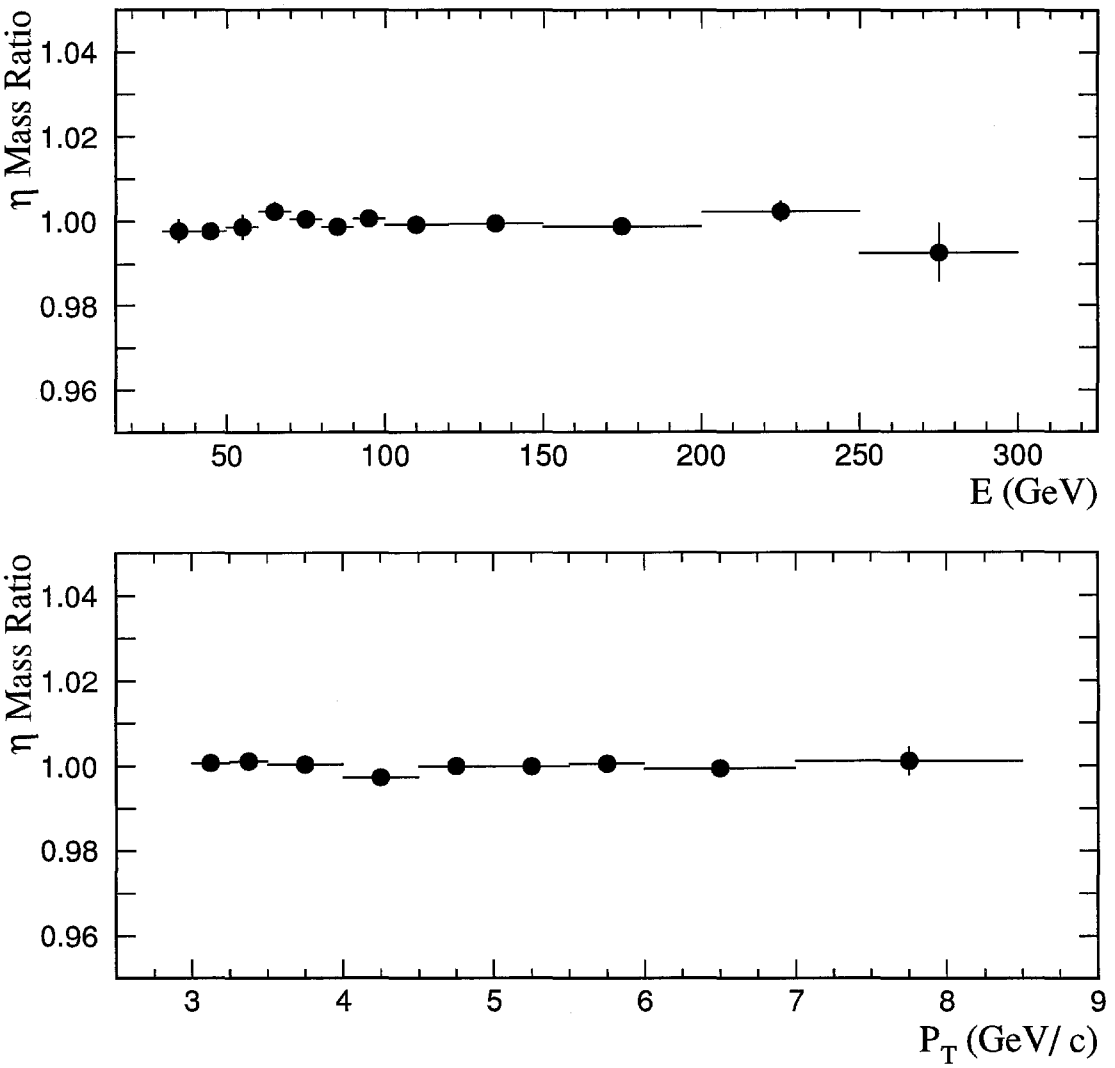

Figure 5.10 Ratio of the η mass to its standard value: top) versus energy of the η bottom) versus p_T of the η

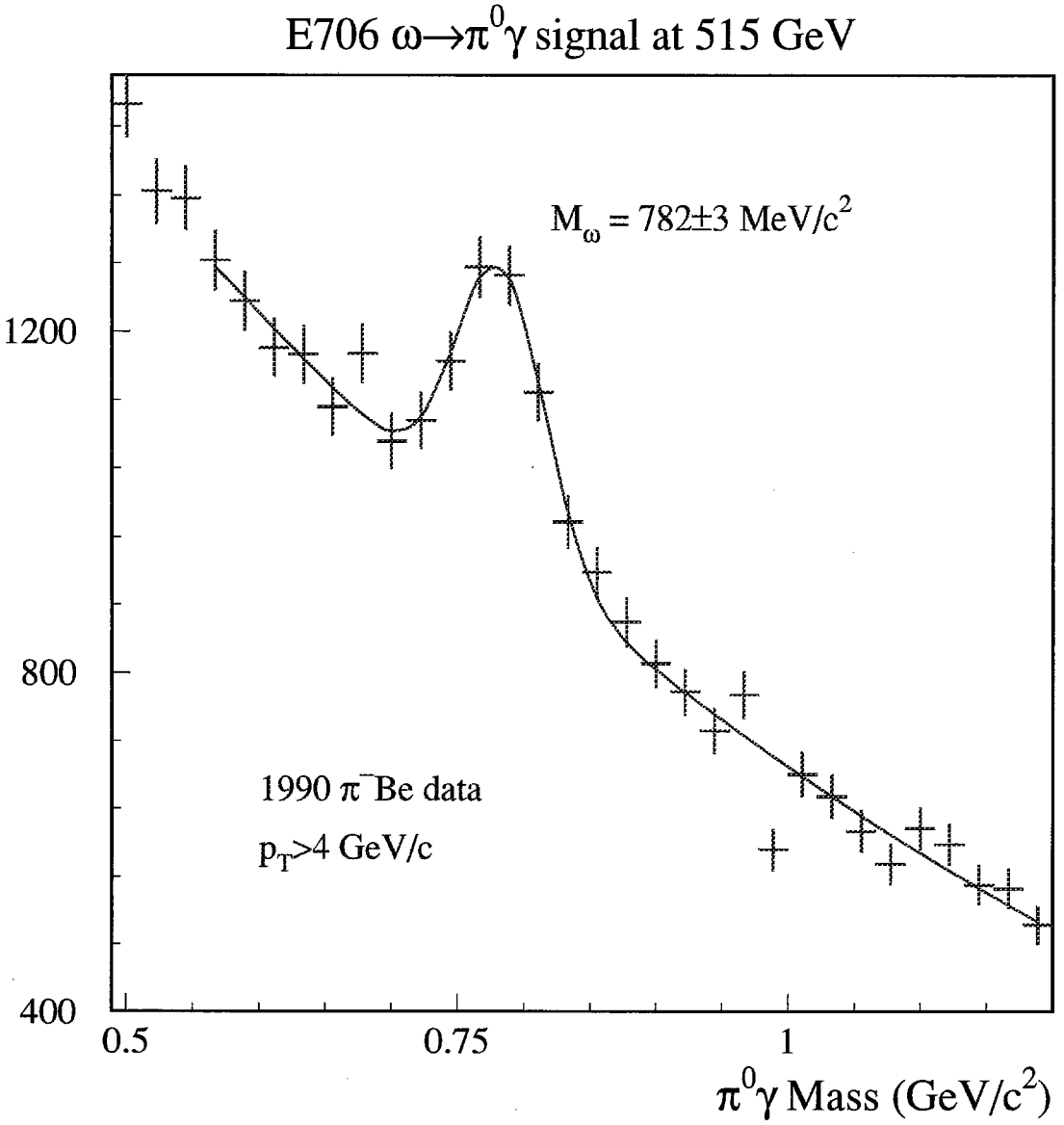

Figure 5.11 $\pi^0\gamma$ invariant mass distribution

Chapter 6 Monte Carlo

The tasks entrusted to the E706 Monte Carlo were twofold:

• Background Estimation: In principle any particle which has a photon as one of its decay products can serve as background to the direct photon signal. In practice, however, the $\gamma\gamma$ decays of π^0 and η account for more than 99% of the background. Photons from these decays of high p_T π^0 or η mesons contribute to the direct photon background in any one of the following situations:

a) one of the photons from the decay is outside of the acceptance of the detector

b) one of the photons from the decay cannot be reconstructed due to its low energy (< 5 GeV)

c) the distance between the two photons from the decay is too small for them to be individually resolved. This occurence is refered to as coalescence.

Since the detector cannot distinguish between direct photons and photons from meson decays on a photon by photon basis, a Monte Carlo is employed to estimate the fractional contribution to the single photon sample in the data that is attributable to misreconstruction of meson decays.

• Efficiency Estimation: A real detection device introduces two main biases into the data.

a) Losses: Some of the showers will not be detected. This may happen when either the energy of the photon is below threshold or when the photon lands outside the acceptance of the detector.

b) Smearing: Fluctuations introduced by a measuring device will invariably smear the energy around its 'true' or generated value.

In addition to the hardware, the software reconstruction program may also introduce similar biases in the data. A Monte Carlo simulation is used to account for these effects in the data so that the underlying physics can be revealed.

6.1 Event Generation

The E706 Monte Carlo used HERWIG [25] v5.6 as its event generator. For the most part, the generator was asked to produce $2 \longrightarrow 2$ QCD hard scatter processes with a certain minimum p_T. This minimum p_T or "PTMIN" is a user specifiable input card in HERWIG which is very useful (especially for steeply falling spectra) in obtaining coverage over a wide p_T range with a reasonable investment in CPU time. Samples were run with the PTMIN set at 0.5, 1.5, 2.25, 3.0, 4.0, 5.0, 6.5, 8.0, 9.0 GeV/c etc.

6.2 Detector Simulation

The E706 detector modelling was based on the CERN software package GEANT [26]. GEANT simulates the passage of elementary particles through matter. To allow the user to customize the 'matter' through which a given particle propogates, GEANT contains a database of standard geometrical shapes and materials so that a complete description of the detector and its material can be made by way of calls to user routines. The detector simulation was performed in two steps. The first step was a painstakingly detailed specification of the E706 spectrometer both in terms of its geometry and its materials. Wherever possible information on the shape and location of any detector element was determined from the original assembly log books and survey measurements. This Monte Carlo

simulation was then run and data from this 'perfect' detector was stored in the appropriate way (space points or hits for the tracking chambers and strip energies for the LAC). The second step involved taking this 'ideal' data and manipulating it to account for detector effects such as inefficiencies, electronics gain variations and noise to get output which was more representative of the real performance of the spectrometer. The Monte Carlo output from this second stage was then reconstructed via the same path as the actual data. After reconstruction, the MC output was compared to data in a number of projections that illustrated shower characteristics, resolution and underlying background levels. Some tweaking to the second stage took place as and when dictated by these comparisons. Up to this point the MC simulation had been run in the 'full shower' mode, i.e., GEANT was allowed to do shower development in great detail taking into account all known sources of energy losses and interaction in each and every layer of material until a cutoff value was reached (1 MeV in this particular case). The problem in running this way was that the time taken to generate events was too long to allow the accumulation of any decent size MC sample in any reasonable period of time. Thus two modifications were made to the full shower Monte Carlo to improve its productivity:

- Wherever possible adjacent layers of different materials were replaced by a homogenous layer of material having the same effective density as the two original ones. Thus the number of what GEANT calls 'volumes' was reduced making the MC faster since this meant that GEANT spent less time evaluating the properties of the material it was in and how the particle would respond to that particular material.

- The cutoff value was raised from 1 MeV to 10 MeV. To account for the remaining energy, a simple routine which took this energy and distributed it according to a dE/dX ionization loss in the detector was implemented.

6.3 Event Selection

6.3.1 Stage 1:

Once an event was generated by HERWIG, the p_T's of all the generated particles in that event were checked to see if there was any particle with $p_T \geq$ (PTMIN-0.5 GeV/c). If there was such a particle and it was not a charged pion or proton or anti-proton the event was handed over to GEANT.

6.3.2 Stage 2:

GEANT tracked all the particles in parallel to the front face of the LAC. Before propagating the particles through the EMLAC, the amount of energy that may be deposited in the groups of eight strips of the EMLAC is estimated using the generated positions and energies of the photons and electrons that have survived up to that point. No shower development or deposition of energy in the strips has been simulated at this stage so the estimate is made by projecting the generated GEANT tracks to the EMLAC and summing up the energies as if the total energy of the particle is deposited at the point of intersection. This is done to simulate in an approximate fashion the data trigger selection criteria. An event passes this stage 2 selection if;

- The p_T in adjacent groups of eight strips $\geq$ PTMIN

or

- If the trigger particle (the one with $p_T \geq$ PTMIN-0.5 GeV/c) from stage 1 was a π^0, η, η', ω, K_S, K_L, γ, electron or neutron, and the total p_T from photons and electrons in the trigger quadrant is greater than PTMIN.

If either of these two conditions is satisfied, the event simulation continues and all the particles get propagated through the LAC.

6.4 Comparison to Data

To verify that the Monte Carlo simulation agrees with data, comparisons between the two can be made in certain representative distributions. Some of the distributions which were scrutinized were:

• Kinematics: Comparisons were made between the generated π^0 p_T and y spectrum in the Monte Carlo to the fully corrected data cross sections in the same variables (see Figure 6.1). The Monte Carlo spectra obviously did not agree with data in these projections. This is a direct result of the fact that in our energy regime the default HERWIG does not reproduce the p_T and y shape observed in our data. Furthermore, it is important that these shapes, especially the p_T projection, match between data and Monte Carlo since resolution smearing and the magnitude of the background γ/π^0 ratio are very sensitive to these distributions. Thus, if the results of the Monte Carlo simulation are to be meaningfully applied to data, the p_T and y distributions in the Monte Carlo should be modified to match data. One can try and achieve that by tweaking the HERWIG input parameters. However, this approach was not pursued for expediency and because there was no guarantee of success. Instead, an event weight was ascribed to each reconstructed entry in the Monte Carlo based on the ratio of the generated p_T and y spectrum in the Monte Carlo to the fully corrected data cross section. This was done by fitting a 2-D p_T-y surface (see Figure 6.2) to the MC/data histogram such that the slope differences in p_T and rapidity between the weighted Monte Carlo and data are eliminated.

• E_{front}/E_{total}: Figure 6.3 shows the distribution of the ratio of the reconstructed energy in the front section of the EMLAC relative to the total energy for both data and Monte Carlo. The good agreement in this projection shown

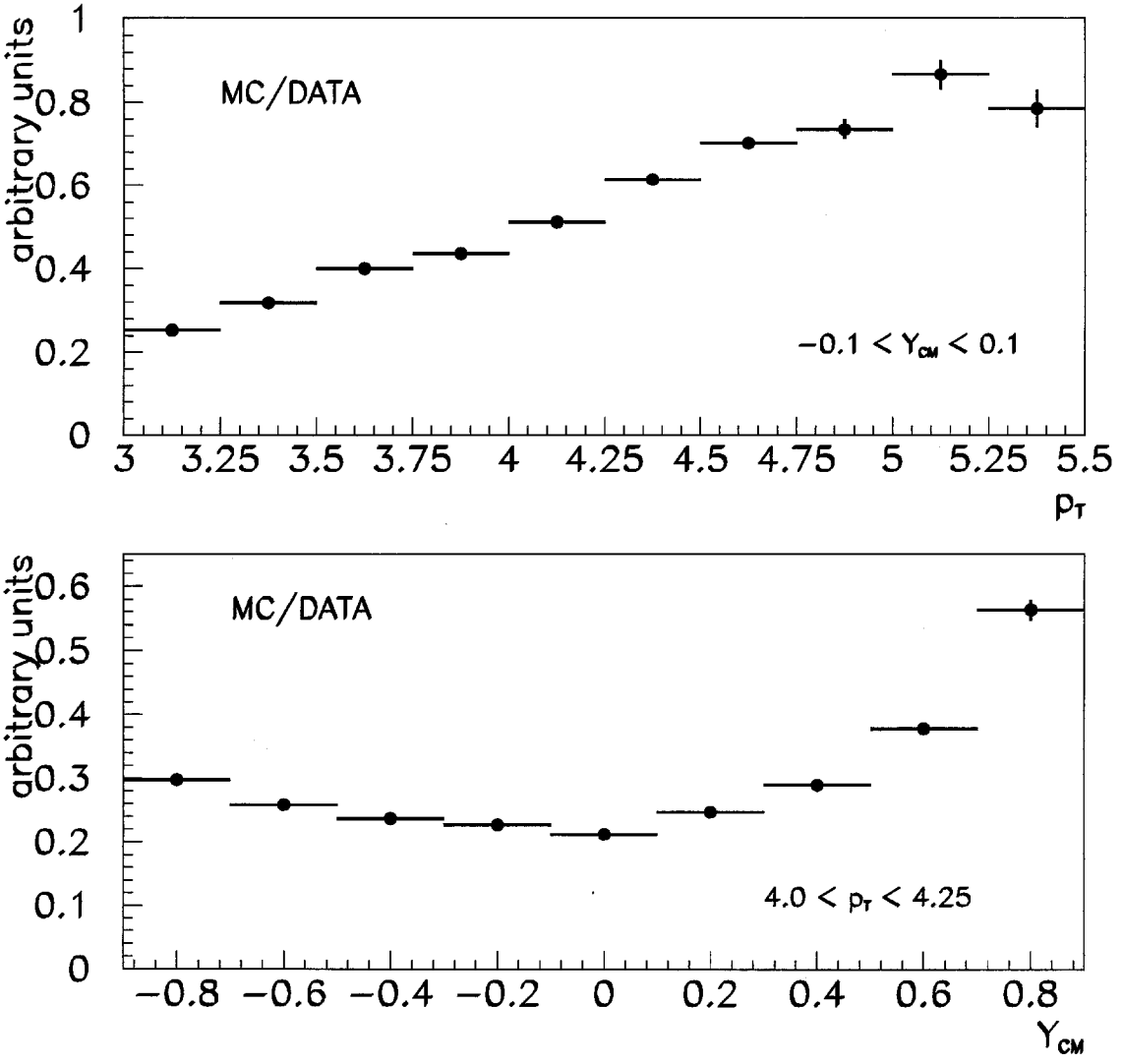

Figure 6.1 Ratio of the HERWIG generated π^0 spectrum to the data π^0 spectrum as a function of the π^0 p_T (top) and center-of-mass rapidity (bottom) for generation threshold 3.0 GeV/c.

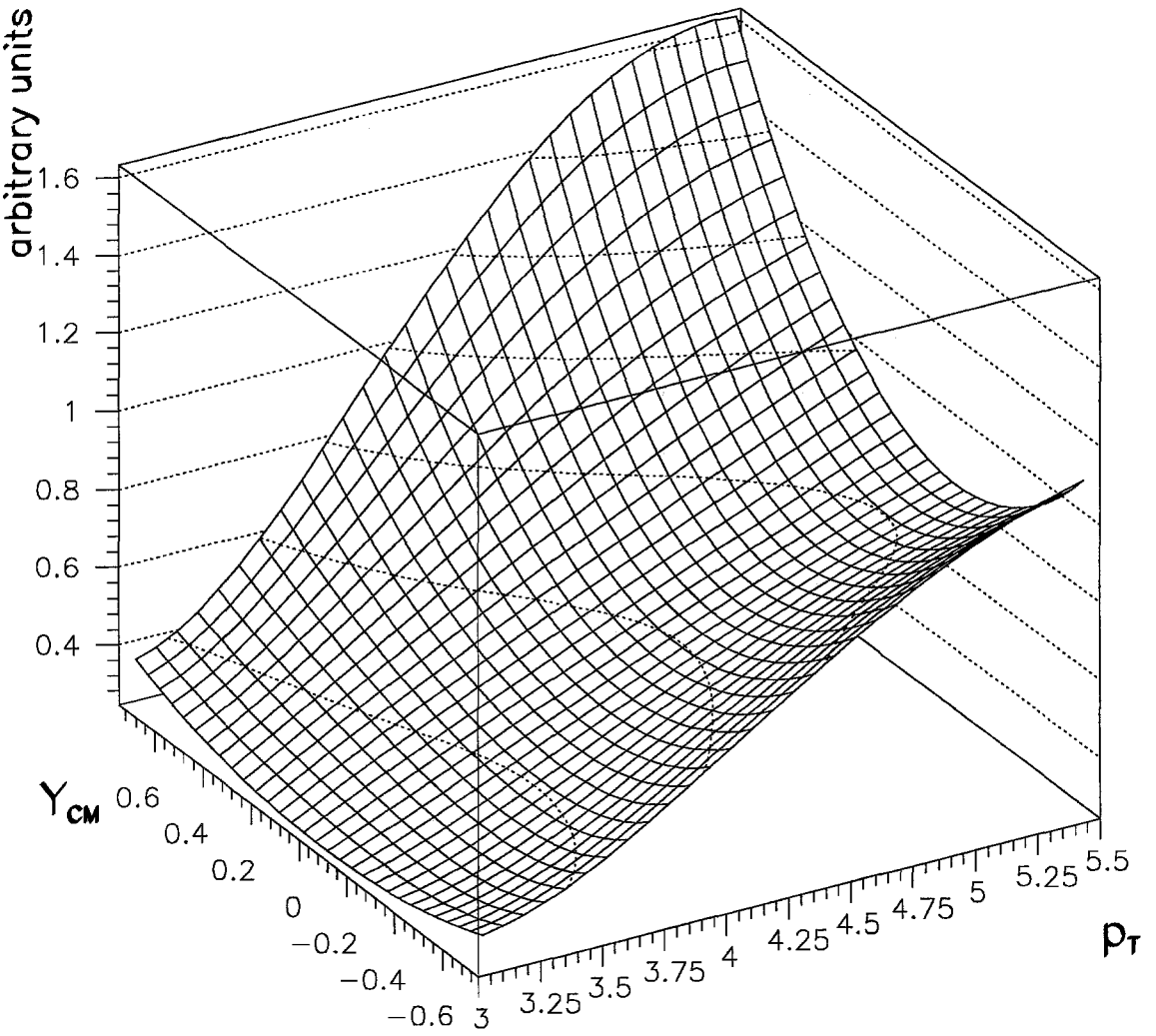

Figure 6.2 The two dimensional π^0 p_T-y weighting surface for threshold 3.0 GeV/c.

in Figure 6.3 indicates that the longitudinal shower development in the Monte Carlo is well simulated. Since the E_{front}/E_{total} ratio is sensitive to the material in front of the calorimeter the good match also signifies that the spectrometer was modelled accurately in the Monte Carlo. It was important to obtain agreement in this projection because the E_{front}/E_{total} ratio influences the identification of π^0's and η's (see chapter 7).

• Mass: Figure 6.4 shows the diphoton invariant mass distribution in the vicinity of the π^0 and η mass for both Monte Carlo and data. The good agreement observed in this projection indicates the successful modelling of the EMLAC resolution and combinatorial background.

• Asymmetry: Figure 6.5 shows the energy asymmetry distribution for diphotons in the π^0 signal region for both the Monte Carlo and the data. The energy asymmetry is related to the 'decay angle' in the centre of mass frame of the π^0 as;

$$A = \frac{|E_{\gamma 1} - E_{\gamma 2}|}{E_{\gamma 1} + E_{\gamma 2}} = \beta \cos\vartheta$$

where $\beta = v/c$ and ϑ is the angle of the emerging photons relative to the direction of flight of the parent pion.

Since the π^0 is a spin 0 particle, it decays isotropically in its rest frame resulting in a flat energy asymmetry distribution. The distribution shown in Figure 6.5 is nearly flat for asymmetries less than 0.7 but falls off at high asymmetry. This depletion in the reconstruction of π^0's at high asymmetry is attributed to losses of low energy photons. A good agreement between the data and Monte Carlo asymmetry distributions as shown in Figure 6.5 indicates that the loss of low energy photons from π^0 decays, which is the dominant source of background to the direct photon signal, has been properly simulated.

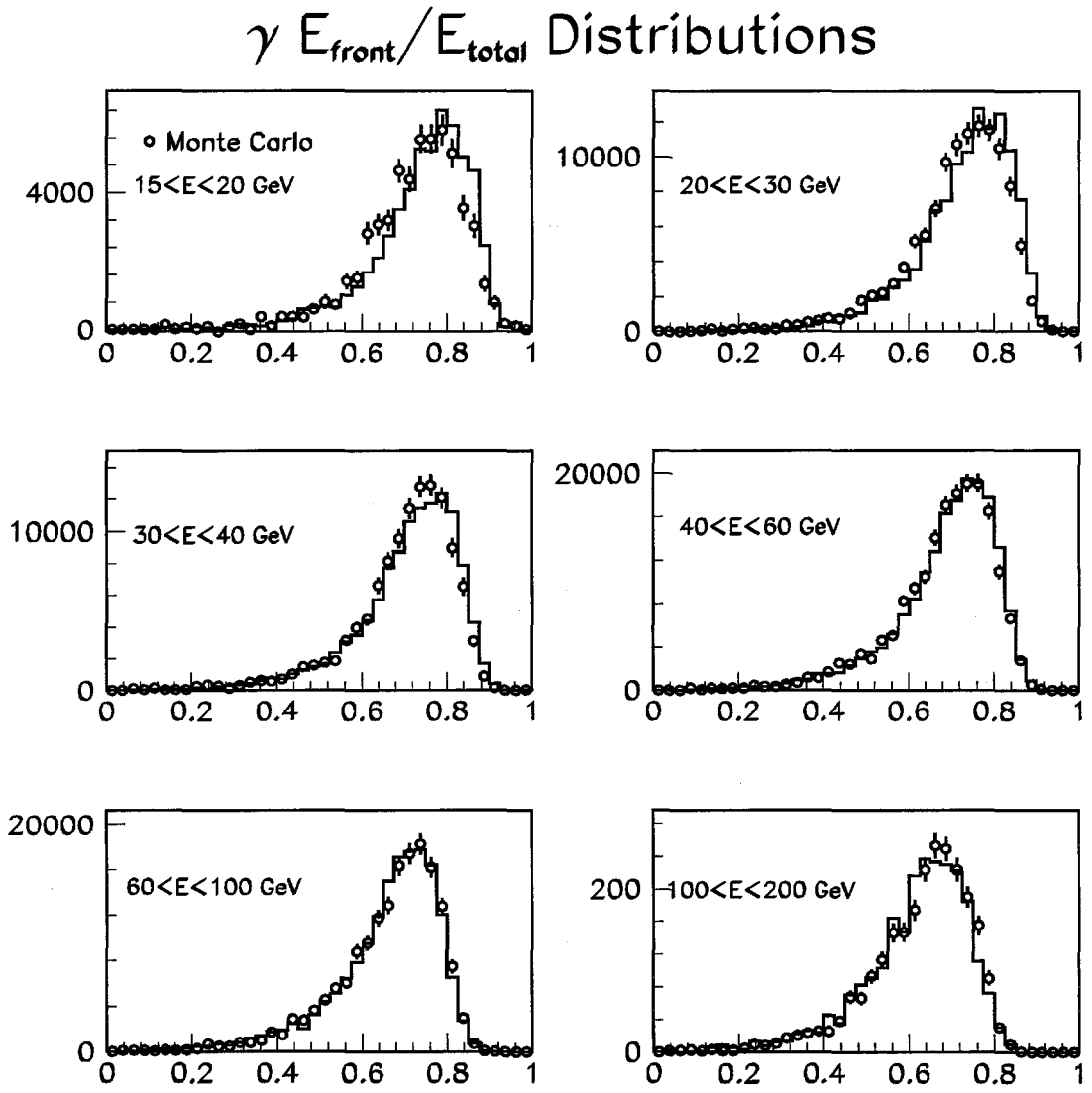

Figure 6.3 E_{front}/E_{total} distributions for data (histogram) and Monte Carlo (open circles) in different energy bins.

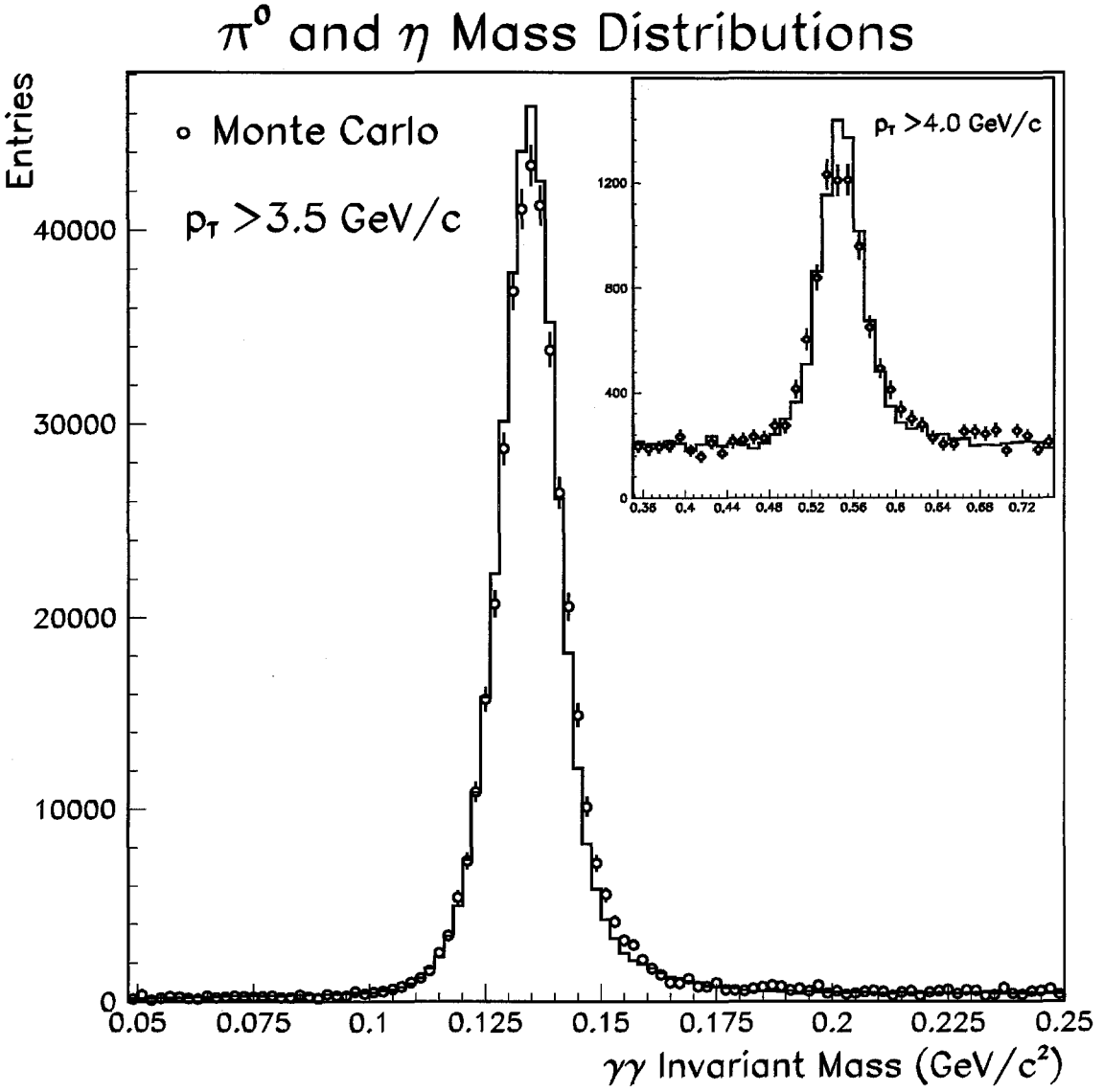

Figure 6.4 Two photon invariant mass distribution for data (histogram) and Monte Carlo (open circles).

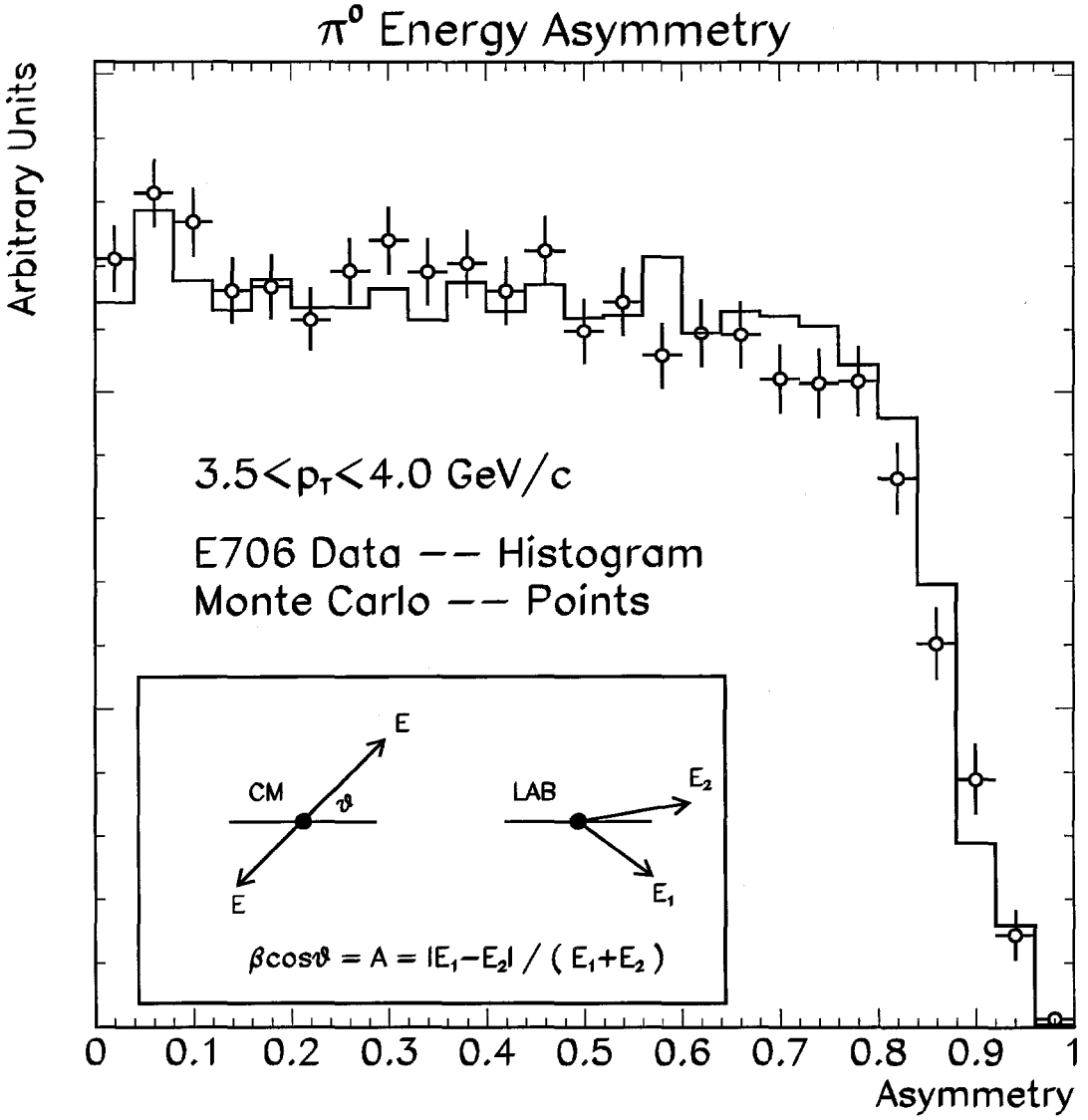

Figure 6.5 Energy asymmtery distribution for data (histogram) and Monte Carlo (open circles).

6.5 Energy Scale

The Monte Carlo energy scale is determined using the same procedure as employed to establish the calibration for the data, which is outlined in Chapter 5. This was done to obtain consistent energy scales between data and Monte Carlo since results from the MC are used to correct the data. By using the same procedure for the MC and data calibration, biases introduced in the calibration process are compensated for. Since the generated energies are available in the Monte Carlo, an additional cross-check can be done. That is to plot the ratio of the reconstructed energy to the generated energy. A ratio of around one as shown in Figure 6.6 implies not only that the MC energy scale has been set properly but also that the procedure of using the π^0 and η mass constraint corrects the energies properly.

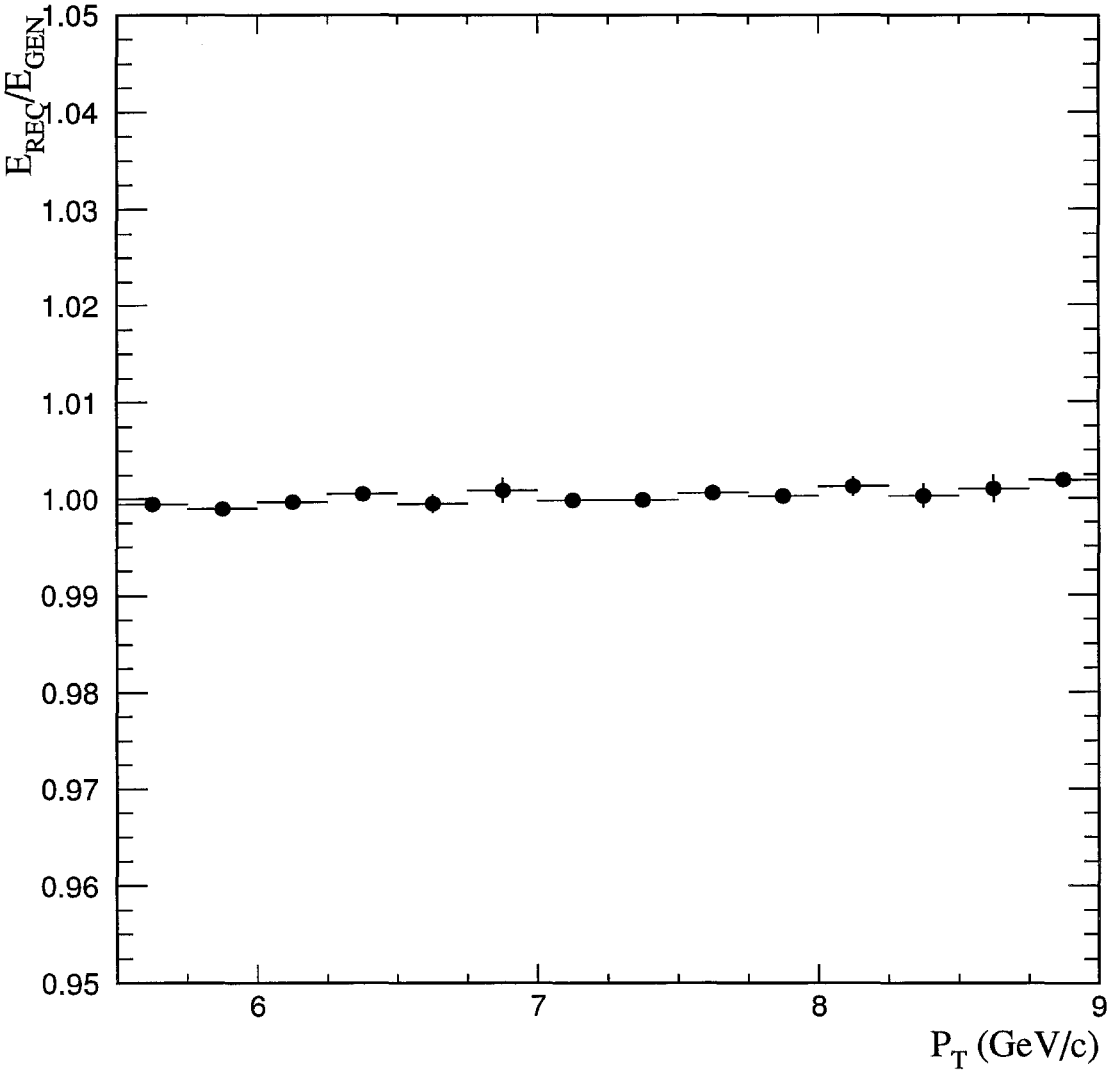

Figure 6.6 The ratio of the reconstructed to generated energy, for π^0's, as a function of reconstructed p_T.

Chapter 7 Data Analysis

This analysis used data accumulated during both the 1990 and 1991 Fermilab fixed target runs of the direct photon production experiment E706. In 1990 the experiment collected data on π^-Be and π^-Cu collisions at 515 GeV/c. In 1991 both 515 GeV/c π^- and 530 and 800 GeV/c proton beam induced data was collected. In addition to beryllium and copper, a hydrogen target was also available during the 1991 fixed target run.

7.1 Data Selection

To ensure the quality of the data, a number of cuts were imposed on the events. This section provides an outline of these selection criteria:

7.1.1 Vertex Requirement

Each event was required to have a reconstructed vertex in the target region. If an event did not have a reconstructed vertex, it was excluded; i.e., no further analysis was done on it. Figure 7.1a shows reconstructed Z-positions of the vertices for events containing a π^0 candidate with $p_T > 3.5$ for data from the 1990 run. The Cu and Be targets and several of the beam and target SSD's are clearly visible.

For the 1990 data sample, Figure 7.1a, b shows the X and Y positions of the vertices as a scatter-plot. The largest square drawn in the plot shows the area covered by the sensitive region of the beam hodoscope, while the circle and truncated circle show the physical locations of the Be and Cu targets, respectively. Evidently the beam hodoscope is centered on the beam but the targets are transversely displaced. Consequently some beam particles counted by

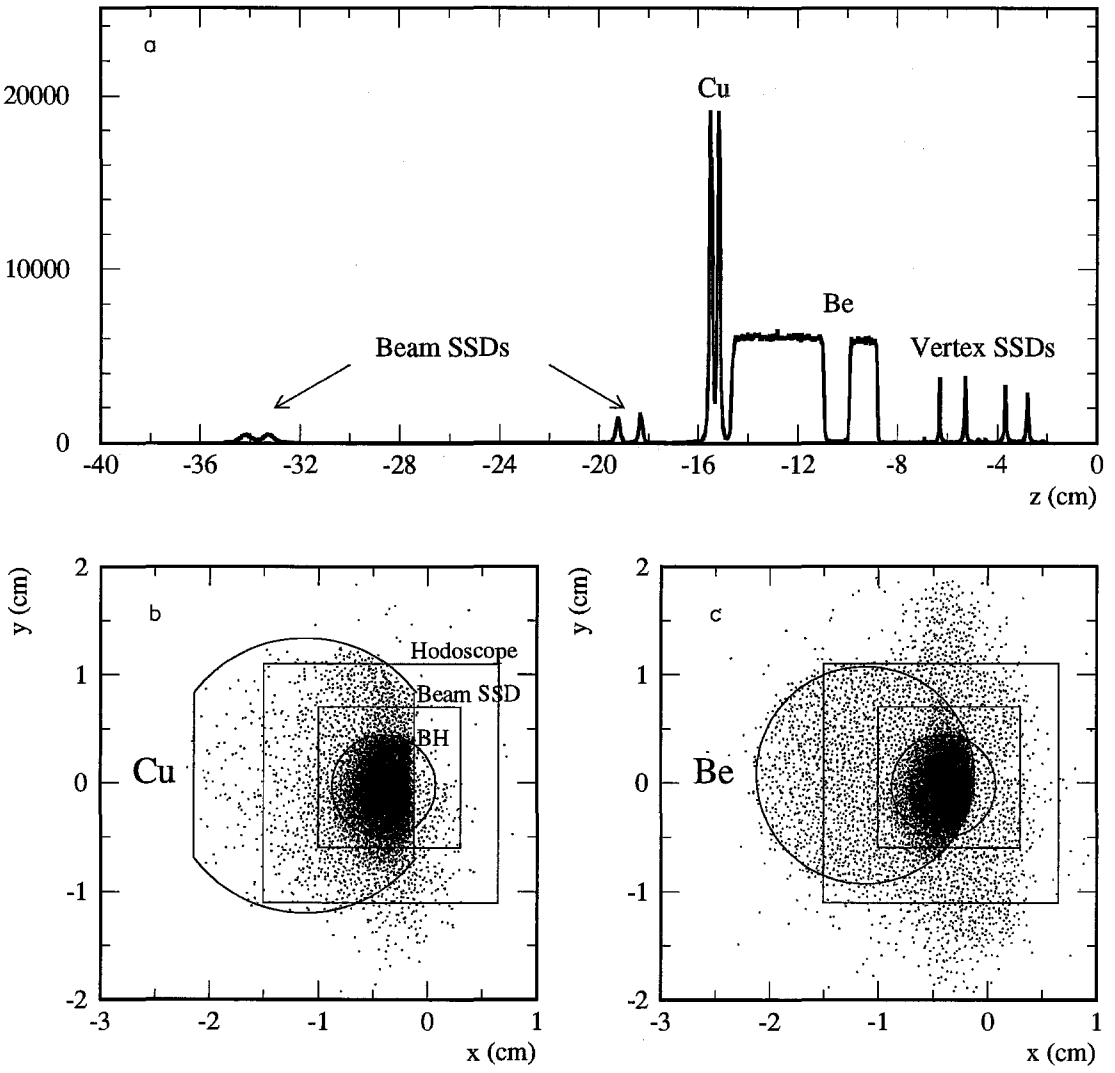

Figure 7.1 Reconstructed location of interactions from events containing high p_T π^0 candidates; a) distribution along the nominal beam or Z-axis, b) X-Y distribution of vertices in the Cu target, c) X-Y distribution of vertices in the Be target.

the hodoscope were not hitting the target. This must be accounted for to get proper normalization. A transverse vertex fiducial region was defined to address this matter.

The beam count correction was made by taking the ratio of the number of vertices reconstructed in the SSD planes immediately upstream of the target within the target fiducial region to the total number of reconstructed vertices in those SSD planes. The process was repeated for the downstream SSD's. The average correction to the beam count was $\approx 35\%$. The systematic uncertainity on this correction, as estimated from the difference in the magnitude of the correction from the upstream and downstream SSD's, was of order 2%. A transverse vertex fiducial region is employed in the analysis of the 1991 data samples too, but the corresponding correction is negligible.

7.1.2 Fiducial Requirement

Showers near the inner and outer edges of the EMLAC were excluded. The photons near octant and quadrant boundaries were also excluded. These showers were excluded since their energy determination was compromised, because for showers near the boundaries, a significant portion of the shower energy can land in the uninstrumented regions of the EMLAC and hence go undetected. Specifically, photons were rejected if;

- their R-position did not lie within $22.7 < \mathrm{R} < 149.5$ cm
- their ϕ position was less than ≈ 2 strips from a octant or quadrant boundary.

The above two conditions define the active or 'fiducial' region of the EMLAC.

7.1.3 E_{front}/E_{total} *Requirement*

Since lead has a high radiation length compared to its interaction length, incident hadrons generally shower later in the EMLAC as compared to showers initiated by photons or electrons (Figure 7.2). Thus an E_{front}/E_{total} requirement is used to discriminate against hadron induced showers. Only showers with E_{front}/E_{total} greater than 0.2 contribute to this analysis.

7.1.4 Muon Rejection

For fixed target experiments using secondary beams, muons may be a significant source of background (particularly if the muons satisfy the trigger used by the experiment to select events). Typically these secondary beams are produced by steering the primary beam (800 GeV/c protons in this case) into a primary target, and then selecting a beam of the desired polarity and momentum from among the particles produced in the interactions in the primary target. In any such hadronic interaction, pions are produced in copious amounts and some of them then decay, in flight, to muons thereby generating a source of beam halo muons. These muons travelling approximately parallel to the beamline can interact in the EMLAC, mimicking high p_T single photon showers. However, contamination from muons is not restricted to the single photon sample and the diphoton signals are also sensitive to this background when, for instance, due to its asymmetric shape (because the detector is focussed on the target) the muon shower may be split by the reconstructor into two photons.

The issue is illustrated in Figure 7.3, which shows the steeply falling π^0 p_T spectrum and the relatively flat muon "apparent" p_T number distribution. For muons, the p_T is "apparent" or fake because it is calculated under the assumption that the shower was caused by a particle originating in the target, which is

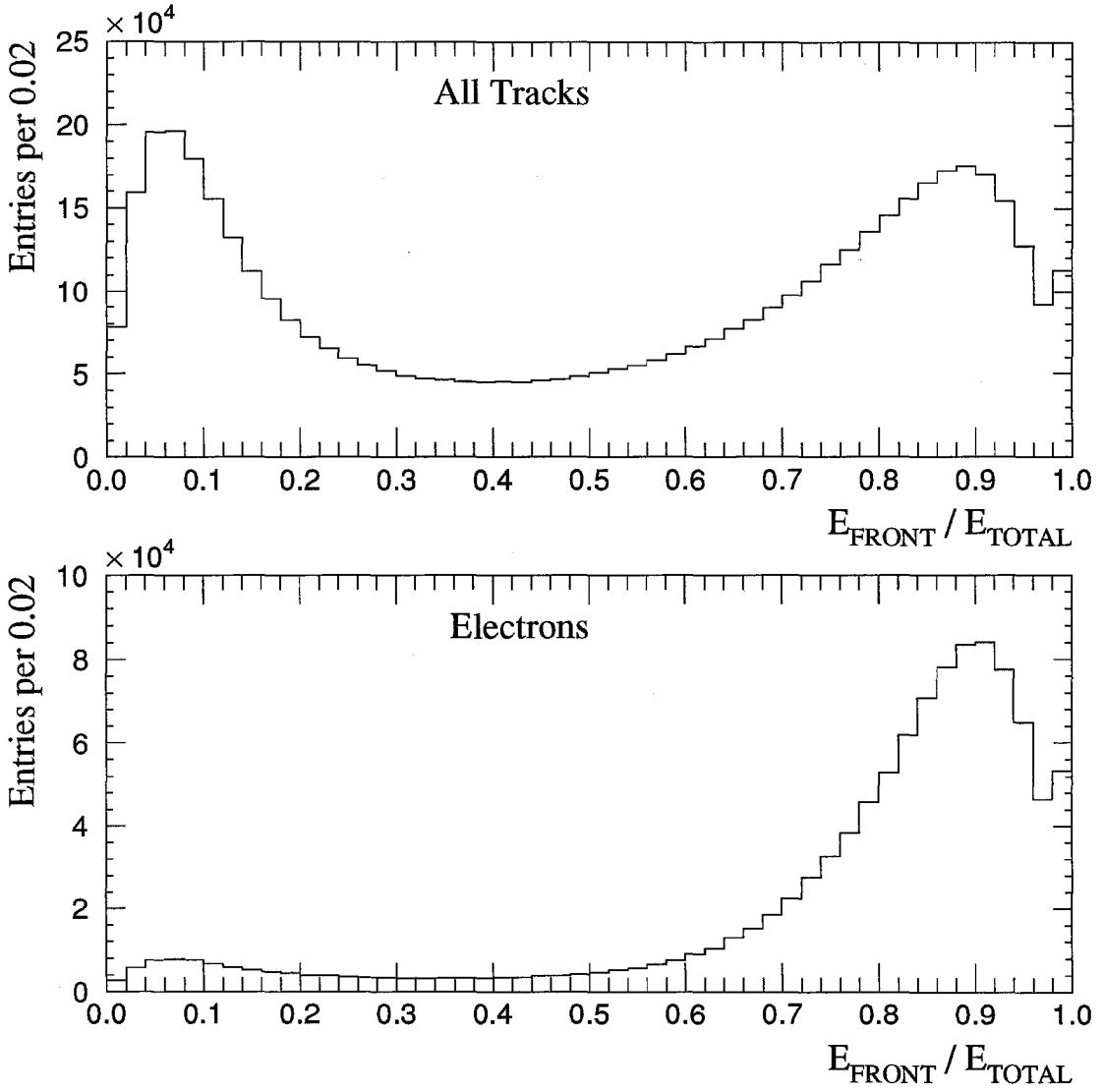

Figure 7.2 The E_{front}/E_{total} distribution for all tracks (top) and electrons (bottom).

clearly not the case for beamline muons. Since the trigger is based on the same assumption, it preferentially selects out these "high p_T" events to be written to tape. So even though the absolute rate of occurence of these muon bremsstrahlung showers is small, the combination of a steeply falling physics spectrum and a trigger enhancement caused by a mis-assessment of p_T (for these muon induced showers) can generate a significant contamination at the high p_T end of the direct photon (or π^0) spectrum.

This muon contamination must be eliminated to achieve the goals of the experiment. Several measures were invoked both online and offline to discriminate against muons. These defenses are outlined below.

- Spoiler Magnets: Installed in the beamline to sweep many of the halo muons away from the spectrometer.

- Veto Walls: Signals from these scintillator walls were part of the trigger logic. If the walls shadowing the trigger quadrant tagged a muon (upstream wall recorded a hit in coincidence with the logical OR of the signals from the downstream walls) within ± 3 buckets of the interaction bucket, the event was rejected. Thus a large fraction of the muon initiated events were rejected online. However, due to inefficiencies and timing issues, some muons could slip through.

As a first step in getting rid of these remaining muon triggered events, the veto wall rejection was expanded offline, to include ± 5 (instead of the ± 3 bucket requirement used in the online veto) buckets on either side of the trigger. In addition, timing jitter between the walls were studied and taken into account when evaluating coincidences. While these steps increased the rejection power of the veto walls they could not eliminate all the muon induced events (primarily due to the sagging of the upstream walls which were exposed to a high flux environment).

• Balance p_T: Due to conservation of momentum, the transverse momentum on the trigger and away side should balance for any scattering process. Since beam halo muons do not come from a scattering in the target, they will generally not be accompanied by a balancing away side jet. Experimentally, the detected transverse momentum will not, in general, exactly balance out even for scatters occurring in the target due to limitations and biases introduced by the detectors. For example, a charged track might lie outside the acceptance of the spectrometer or a neutral hadron might not deposit enough energy in the calorimeter, leading to an underestimation of the transverse momentum on the away side. In addition, if there is some intrinsic transverse momentum in the interacting partons, a perfect balance may not be obtained. However, the fact remains that on average the difference between the transverse momentum of the trigger particle and tranverse momentum on the away side is generally much less for particles coming from an interaction in the target than for beam halo muon triggered events. Figure 7.4 shows the distribution of the ratio of the p_T of all charged and neutral particles lying within a 120° cone on the away side to the p_T of the trigger particle. Only direct photon or π^0 candidates, for which this ratio was greater than 0.3, contributed to this analysis.

• Directionality: For those showers whose position can be measured independently in both the front and back sections of the EMLAC, those position measurements provide information on the incident direction of the particle that caused the shower. Beam halo muons are frequently incident nearly parallel to the beamline and thus these showers are distinguishable from showers coming from a particle originating in the target. We measure this discrimination via the variable δ (labelled directionality), which is defined as:

$$\delta = R_f - \frac{Z_f^{LAC}}{Z_b^{LAC}} R_b$$

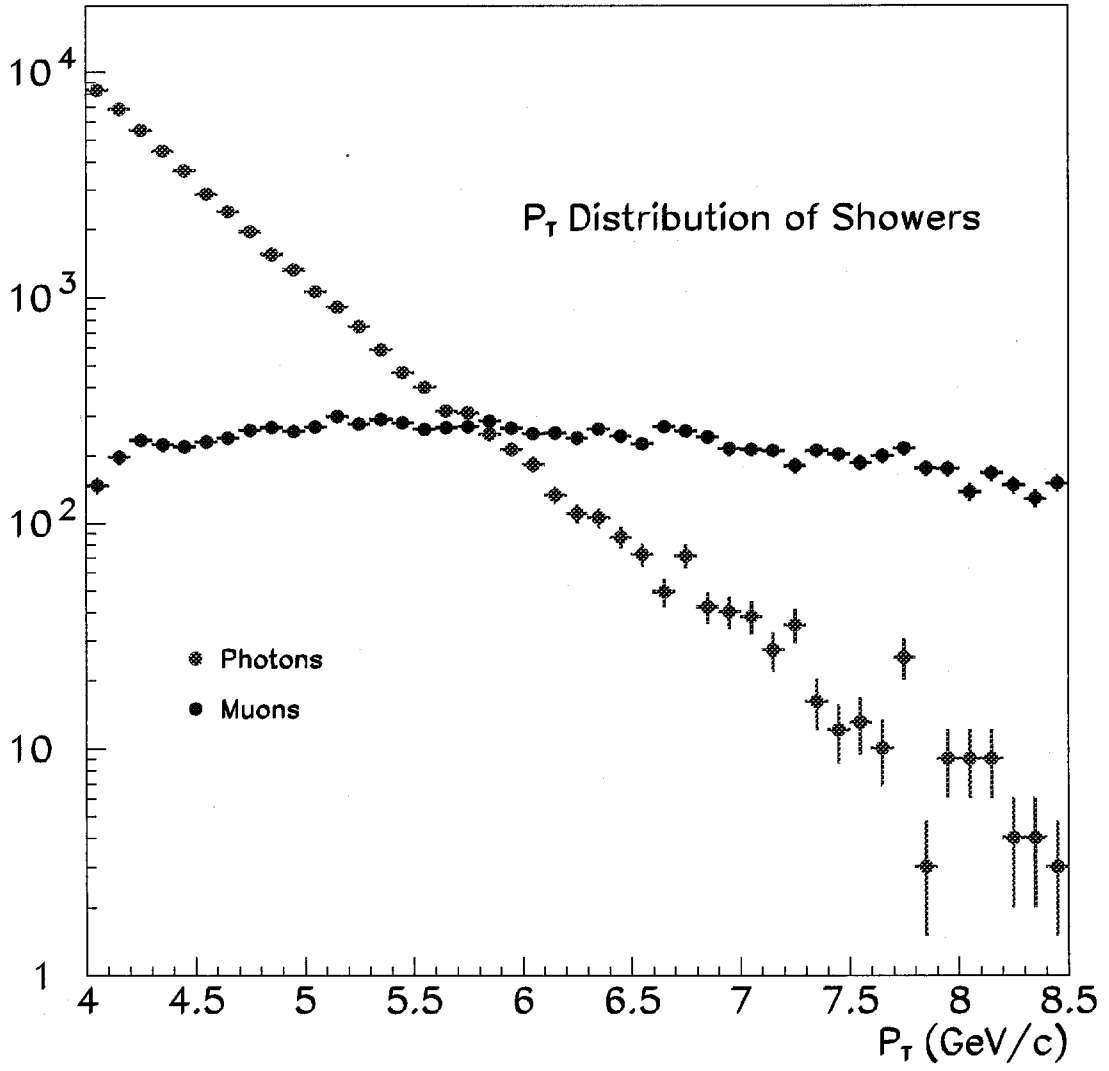

Figure 7.3 The number distribution for 'photon like' and 'muon like' showers as a function of p_T. The p_T has been calculated under the assumption that the particles that generated the showers are coming from the target.

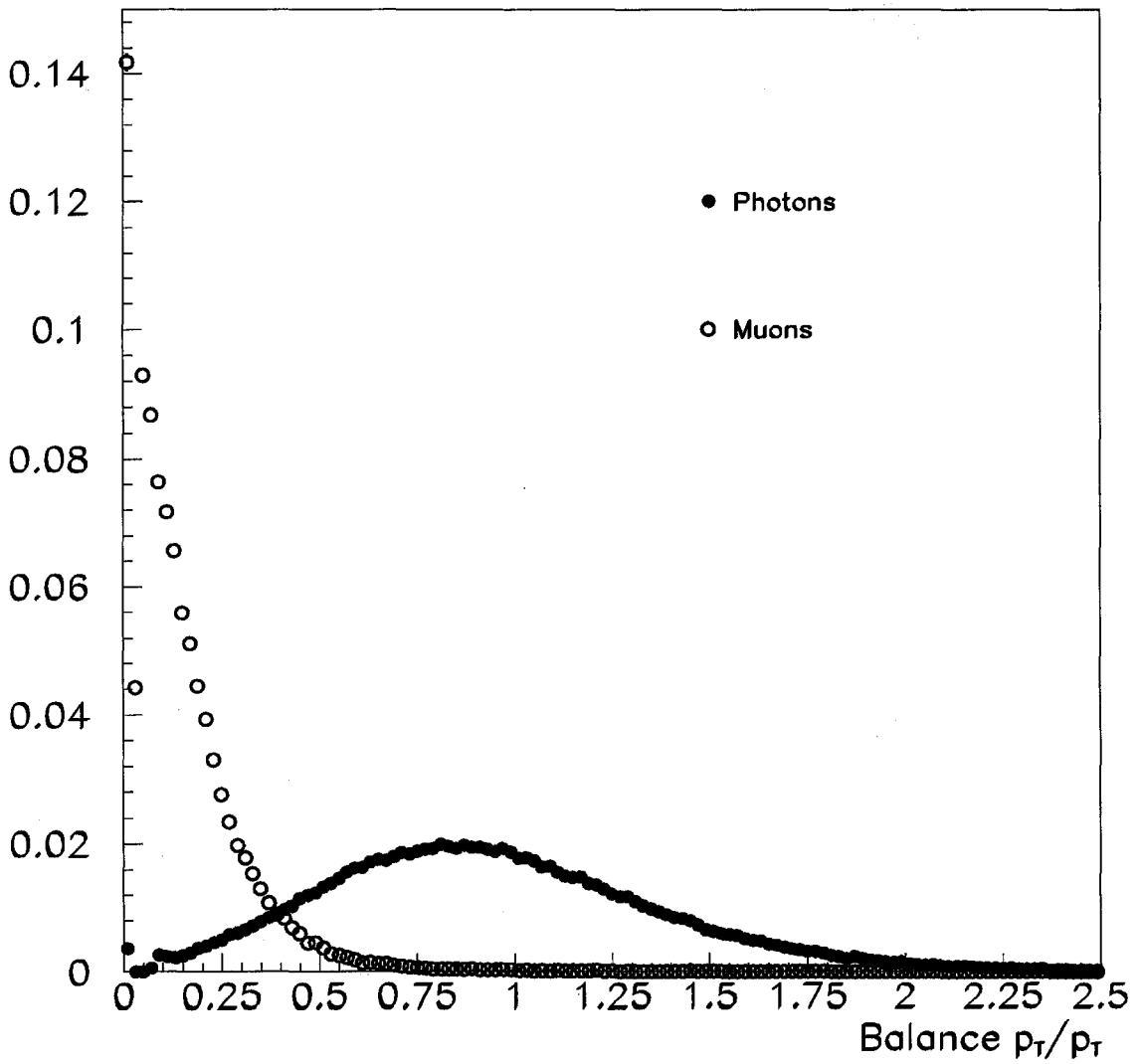

Figure 7.4 The balance-p_T/p_T distribution for photons (closed circles) and muons (open circles). The photons are defined by requiring that the veto wall, directionality and χ^2/energy have 'photon' signatures. The opposite is done isolate the muon sample.

δ will be near zero for showers from particles originating in the vicinity of the target. It will however, be a positive number for showers from beam halo muons that are nearly parallel to the beamline, thus providing discrimination against those muons (see Figure 7.5). To contribute to this analysis the shower directionality had to satisfy the following conditions;

For R $<$ 40.0 cm: $\delta < 0.193$ cm

For R $>$ 40.0 cm: $\delta < 0.0048$ R cm

where R is the reconstructed radial position of the shower in the EMLAC.

• χ^2/Energy: Because of the focussed geometry of the EMLAC showers originating from particles travelling parallel to the beam axis appear asymmetric in the detector, resulting in bad χ^2's when fitted with the fixed symmetric shower shape used by the reconstructor. The shower χ^2's also depends on the energy of the shower, increasing with increasing energy. Thus, a cut is made on the χ^2/Energy variable so as to minimize losses due to the increment in the χ^2 value with energy. The χ^2/Energy distribution for photon and muon induced showers is shown in Figure 7.6. Only showers with χ^2/Energy less than 0.1 contributed to this analysis.

The cut values, for each of the muon cuts, were chosen so as to maximize muon and minimize photon rejection. Nevertheless, some improper rejection of photons does take place on application of the muon cuts. To account for this loss, separate corrections were done for each of the cuts as functions of p_T and rapidity. The basic technique in evaluating these corrections was to isolate a pure sample of photons by using harsh versions of three of the four muon cuts. The fourth muon cut (the one for which the correction is being evaluated) is then applied to

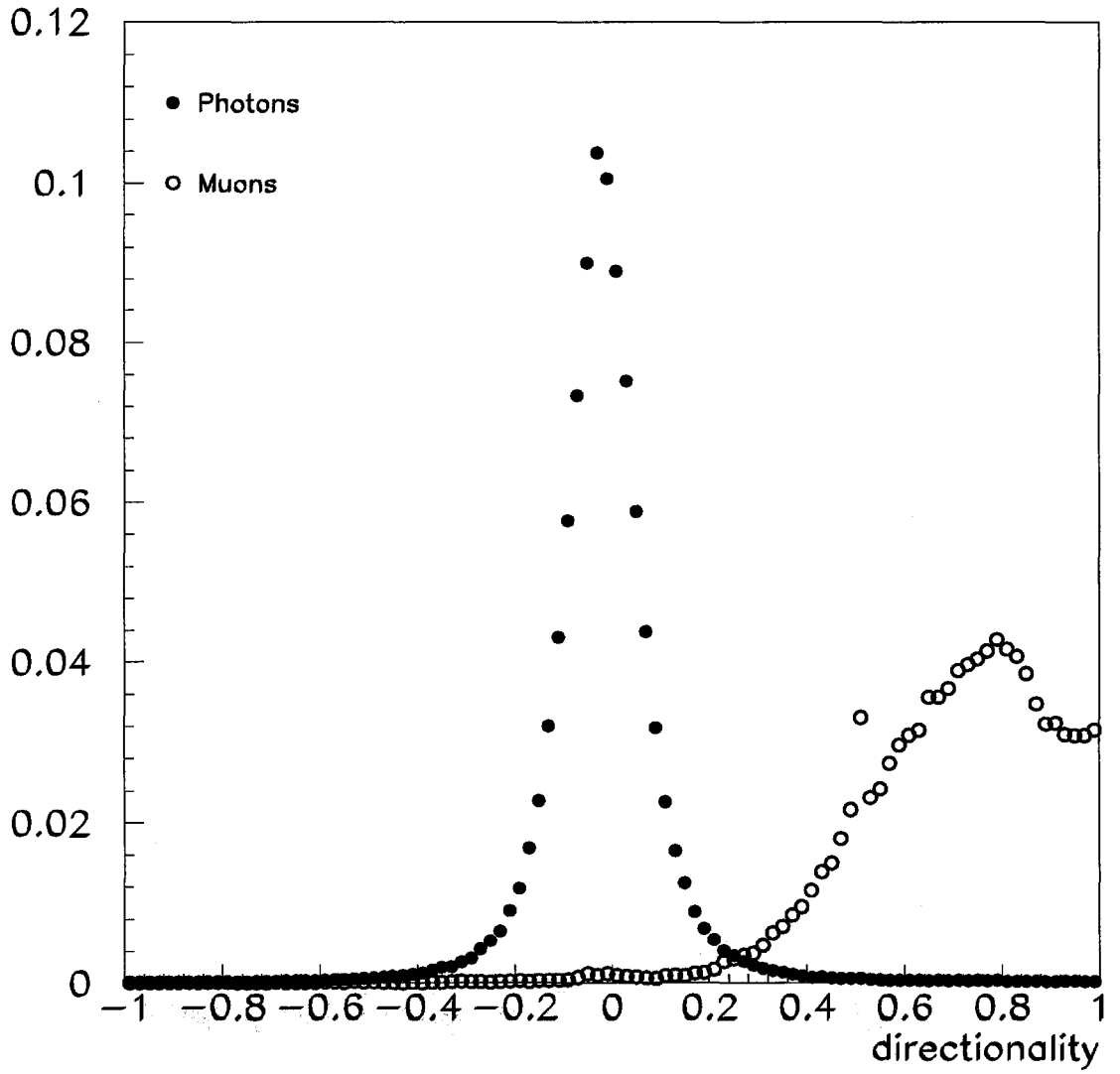

Figure 7.5 The directionality distribution for photons (closed circles) and muons (open circles). The photon sample is defined by requiring that the veto wall, balance-p_T/p_T and χ^2/energy exhibit photon signatures. The opposite is done to isolate the muon sample.

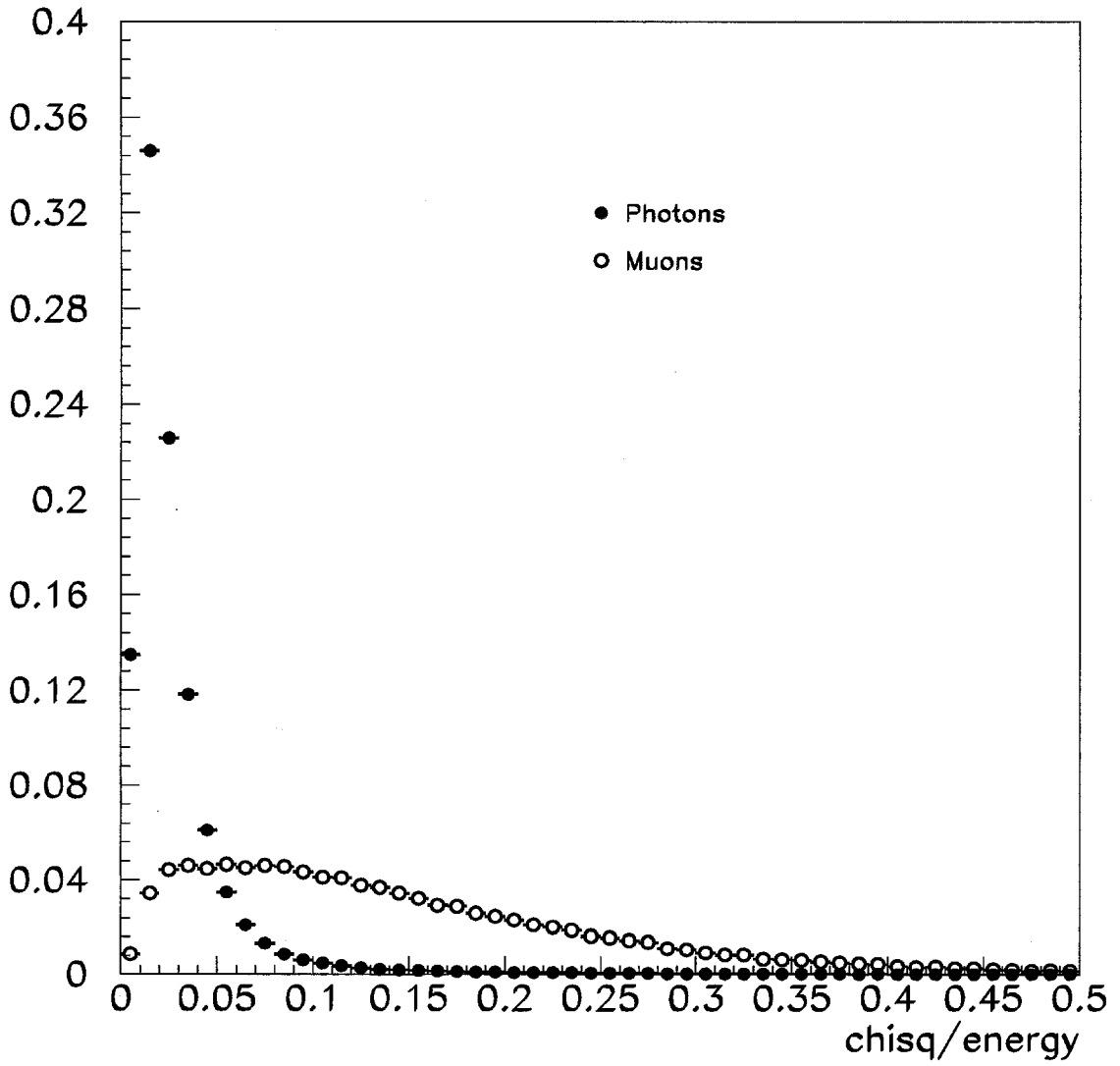

Figure 7.6 The χ^2/Energy distribution for photons (closed circles) and muons (open circles).

this pure photon sample. The correction for the cut in question is given by the fraction of muons cut due its application. The correction for all the muon cuts taken together was $\approx 10\%$.

7.2 Direct Photon Signal

As mentioned earlier, the central issue in extraction of a direct photon signal is the identification and elimination of background. The major sources of this background, after rejection of showers due to hadrons and muons, are the $\gamma\gamma$ decays of high transverse momentum neutral mesons such as π^0's and η's. Chapter 1 outlined some of the experimental techniques used to separate out the contribution of neutral meson decays to the high p_T photon sample. As indicated in Chapter 1, E706 uses the 'direct method'. The strength of this method is that a large part of the potential background is fully reconstructed, and eliminated from the candidate direct photon sample. The remaining background is removed using statistical subtraction. The basic steps involved in extracting the direct photon signal from a sample of high p_T photons via the E706 'direct method' are:

- Neutral Meson Reconstruction: The $\gamma\gamma$ decays of π^0 and η mesons are reconstructed using photons detected in the EMLAC. To do this, an invariant mass is calculated for each diphoton combination within the same octant. The invariant mass distribution has a relatively flat background with peaks around the π^0 and η resonances (see Figure 7.7). The idea here is to eliminate those photons that are associated with π^0 or η decays from further considerations. To be more precise, all photons which participate in diphoton combinations that have an energy asymmetry below a specified cut and yield an invariant mass in the π^0 or η 'mass band' are excluded from the candidate direct photon sample. The commonly used values of the asymmetry cut are 0.75 and 0.9. For π^0's the mass

band is defined as the mass region between $0.1 < \gamma\gamma$ mass < 0.18 GeV/c^2 and for η's as $0.45 < \gamma\gamma$ mass < 0.65 GeV/c^2. However, the peak within this 'signal region' sits on an approximately linear background. It is important to subtract out this background to get a correct count of the number of π^0's or η's. To do this subtraction a 'sideband region' is defined. Any entry which lies within $0.07 < \gamma\gamma$ mass < 0.1 GeV/c^2 or $0.19 < \gamma\gamma$ mass < 0.24 GeV/c^2 is said to be in the π^0 'sideband region'. The sideband region for η's is defined as $0.35 < \gamma\gamma$ mass < 0.45 GeV/c^2 and $0.65 < \gamma\gamma$ mass < 0.75 GeV/c^2. Since the background is approximately linear and the size of the sideband regions correspond to that of the signal region, the $\pi^0(\eta)$ *signal* is given by the number of $\gamma\gamma$ pairs found in the $\pi^0(\eta)$ massband region minus the number of pairs found in their respective sideband regions.

• Photon Definitions: A direct photon candidate is defined as a photon that does not yield (in combination with other photons in the octant) any diphoton object with mass in π^0 or η mass bands having energy asymmetry less than a cut value. Since the asymmetry cut value is a matter of choice a variety of direct photon definitions are possible. The commonly used definitions in this experiment are the '75' and '90' definitions. '75' refers to the direct photon definition which uses the energy asymmetry cut of 0.75 and '90' corresponds to the cut value of 0.9. At this stage, one must take note of the fact that some of the true direct photons are going to be eliminated from the candidate sample due to these definitions. This can happen when a combination of the true direct photon with one of the other photons in the octant happens to yield an invariant mass in the π^0 or η mass band with asymmetry less than the cut value. This accidental loss of direct photons can be treated in two ways. One can either compensate for this loss by weighting the photons whose invariant mass combinations land in the π^0 or η sideband region by a factor of two (the 75s and 90s definitions) or one can leave the

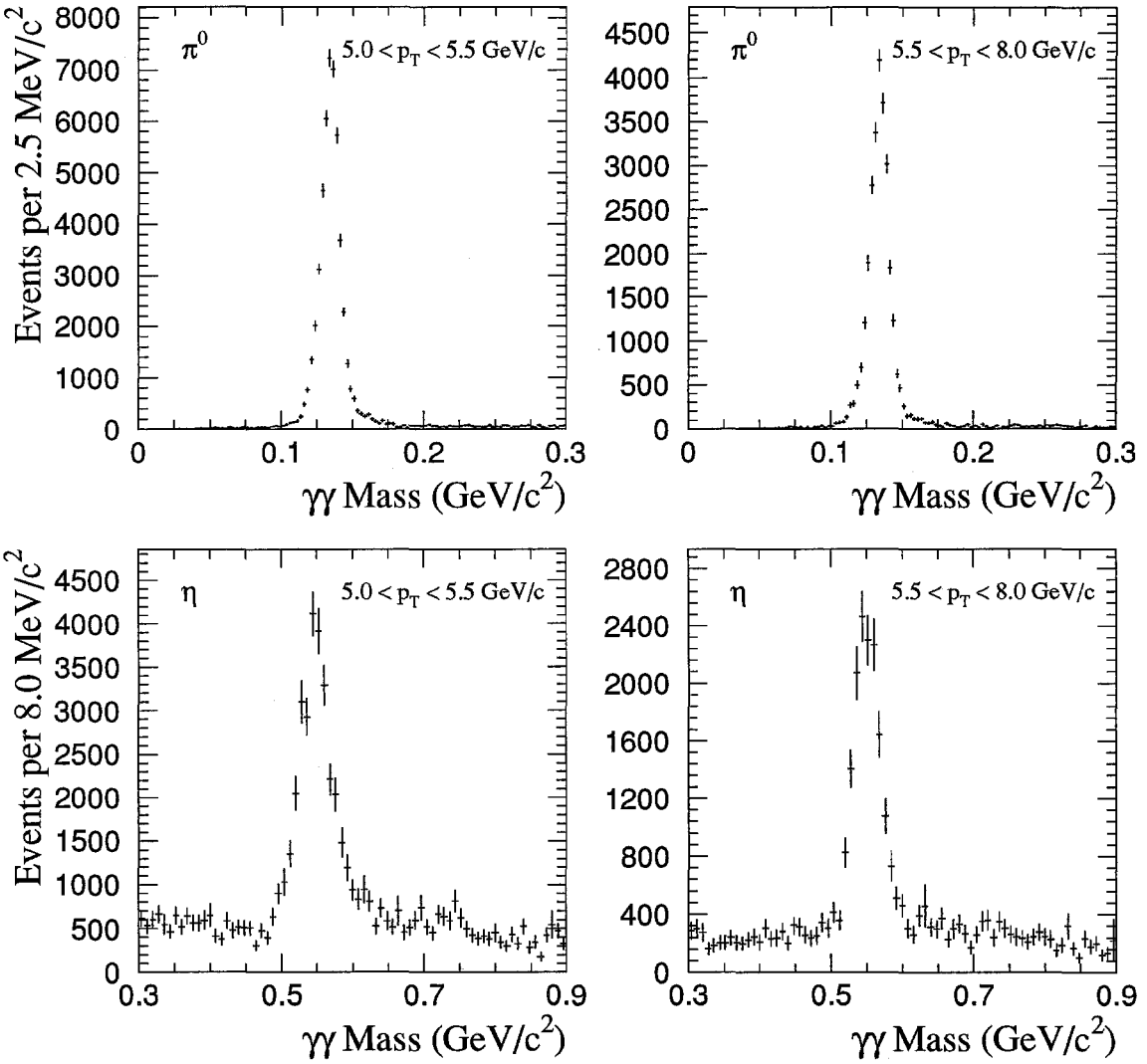

Figure 7.7 The $\gamma\gamma$ mass distribution for two p_T bins showing the π^0 and η signal and sideband regions.

loss alone for the moment (the 75n and 90n definitions). The 's' definitions tend to overestimate and the 'n' definitions underestimate this loss. Their respective biases are taken care of through Monte Carlo corrections for each of the definitions separately.

• Statistical Subtraction: After excluding photons attributed to π^0 or η decays, the direct photon candidate sample now consists of true direct photons and photons from neutral mesons, such as π^0 and η, which could not be fully reconstructed. The circumstances under which such misreconstruction may occur have already been described in Chapter 4. This residual background to the direct photon signal is accounted for by the Monte Carlo simulation. The Monte Carlo used for this specific purpose does not contain true direct photon events. Thus any photon in this Monte Carlo sample that satisfies the direct photon candidate definition is really a shower from a background source. Since the Monte Carlo events go through the same reconstruction and analysis chain as the data and have identical meson and photon definitions applied to them, the number distribution of direct photon candidates from this neutral meson Monte Carlo provides information on the residual background contribution to the direct photon signal from meson decays. In practice this contribution is quoted as a fractional contribution or rate (to do away with normalization issues between the Monte Carlo and data) by taking a ratio of the 'direct photon' candidate sample obtained from the neutral meson Monte Carlo to the number of Monte Carlo π^0's (commonly refered to the as the gamma-to-π^0 ratio: γ/π^0). Figure 7.8 through Figure 7.10 show the γ/π^0 ratio for both data and Monte Carlo. The excess of the data γ/π^0 over the Monte Carlo or background γ/π^0 illustrates the presence of a strong direct photon signal in our data sample.

$$N^{\gamma}_{\text{true}} = N^{\gamma}_{\text{Data}} - (N^{\gamma}/N^{\pi^0})_{\text{MC}}\, N^{\pi^0}_{\text{Data}}$$

where;

N^{γ}_{Data} is the corrected yield of direct photon candidates from the data.

N^{γ}_{MC} is the corrected yield of direct photon candidates from the Monte Carlo.

$N^{\pi^0}_{MC}$ is the corrected yield of Monte Carlo π^0's

$N^{\pi^0}_{Data}$ is the corrected yield of data π^0's

(The corrected yield is obtained by weighting the observed number. These weights correct for muon cuts, fiducial requirement, photon conversions etc. These corrections are discussed in the next section.)

In practice, the statistical subtraction described above is done by first fitting the Monte Carlo γ/π^0 ratio as a 2-D surface in p_T and y (see Figure 7.11). The resultant function is then multiplied by the measured data π^0 cross section and the product is subtracted bin by bin from the weighted data direct photon candidate sample.

7.3 Cross Sections

The π^0 and direct photon invariant cross sections per nucleon are written as:

$$E\frac{d^3\sigma}{dp^3} = \frac{1}{2\pi p_T \delta p_T \delta y_{cm}} \frac{1}{\rho l N_a} \frac{N^{corr}(p_T, y_{cm})}{(LTB)}(ABS)$$

where $N^{corr}(p_T, y_{cm})$ is the corrected yield of π^0's or direct photons per p_T-y_{cm} interval.

- For π^0's: $N^{corr} = N^{\gamma\gamma}_{massband} - N^{\gamma\gamma}_{sideband}$

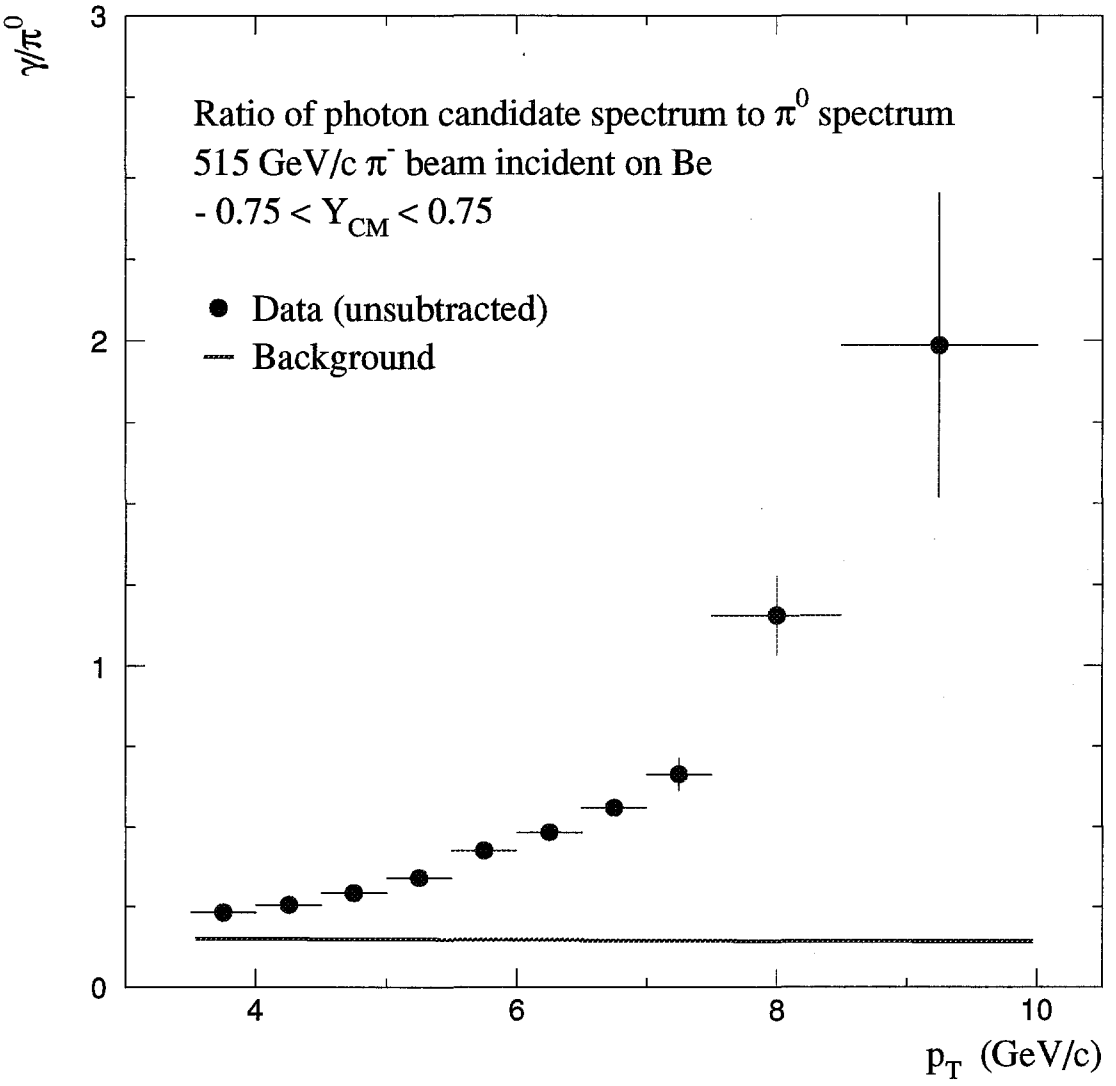

Figure 7.8 The data (points) and Monte Carlo (curve) γ/π^0 ratio as a function of p_T for 515 GeV/c π^- beam incident on a beryllium target.

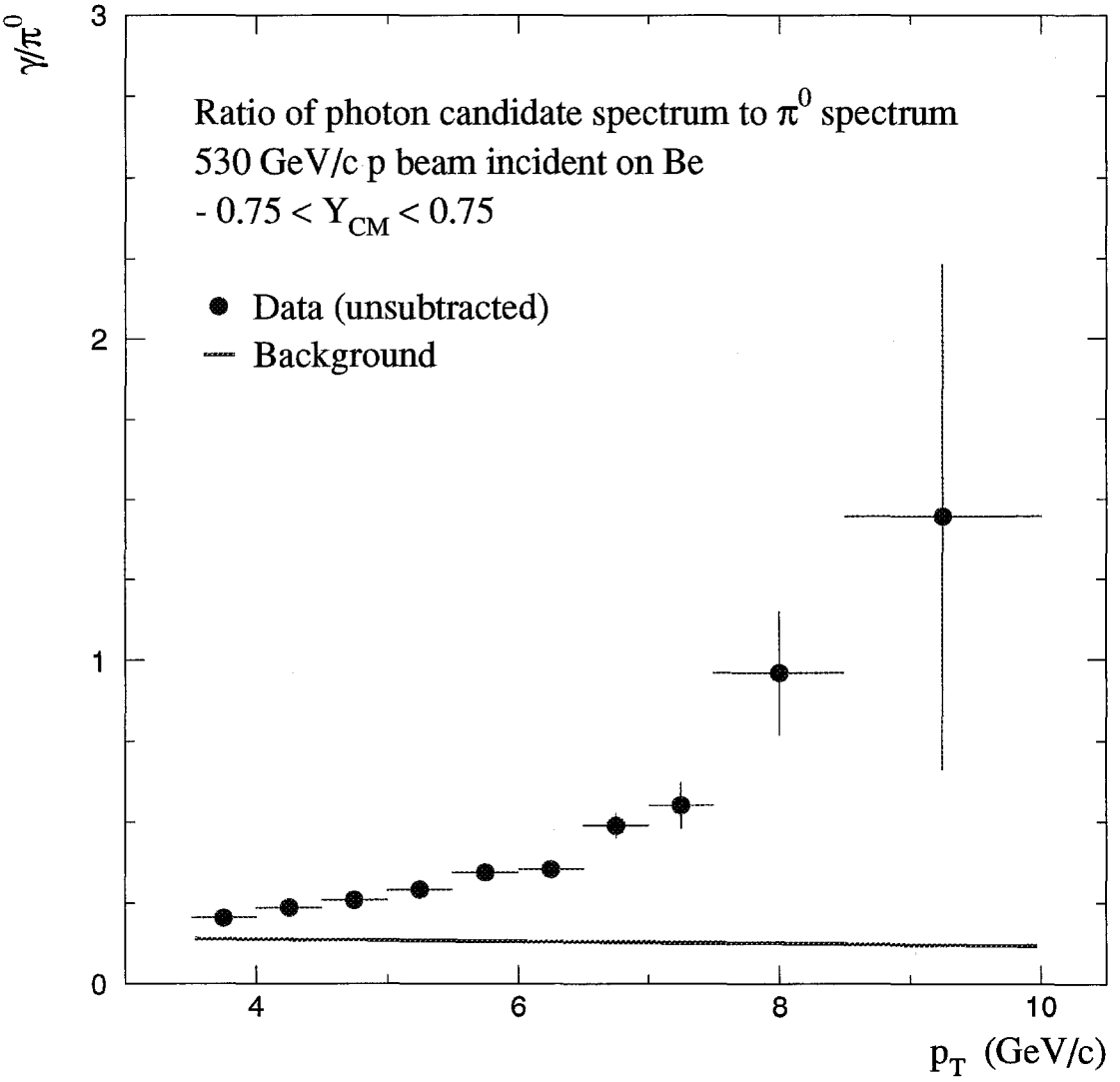

Figure 7.9 The data (points) and Monte Carlo (curve) γ/π^0 ratio as a function of p_T for 530 GeV/c proton beam incident on a beryllium target.

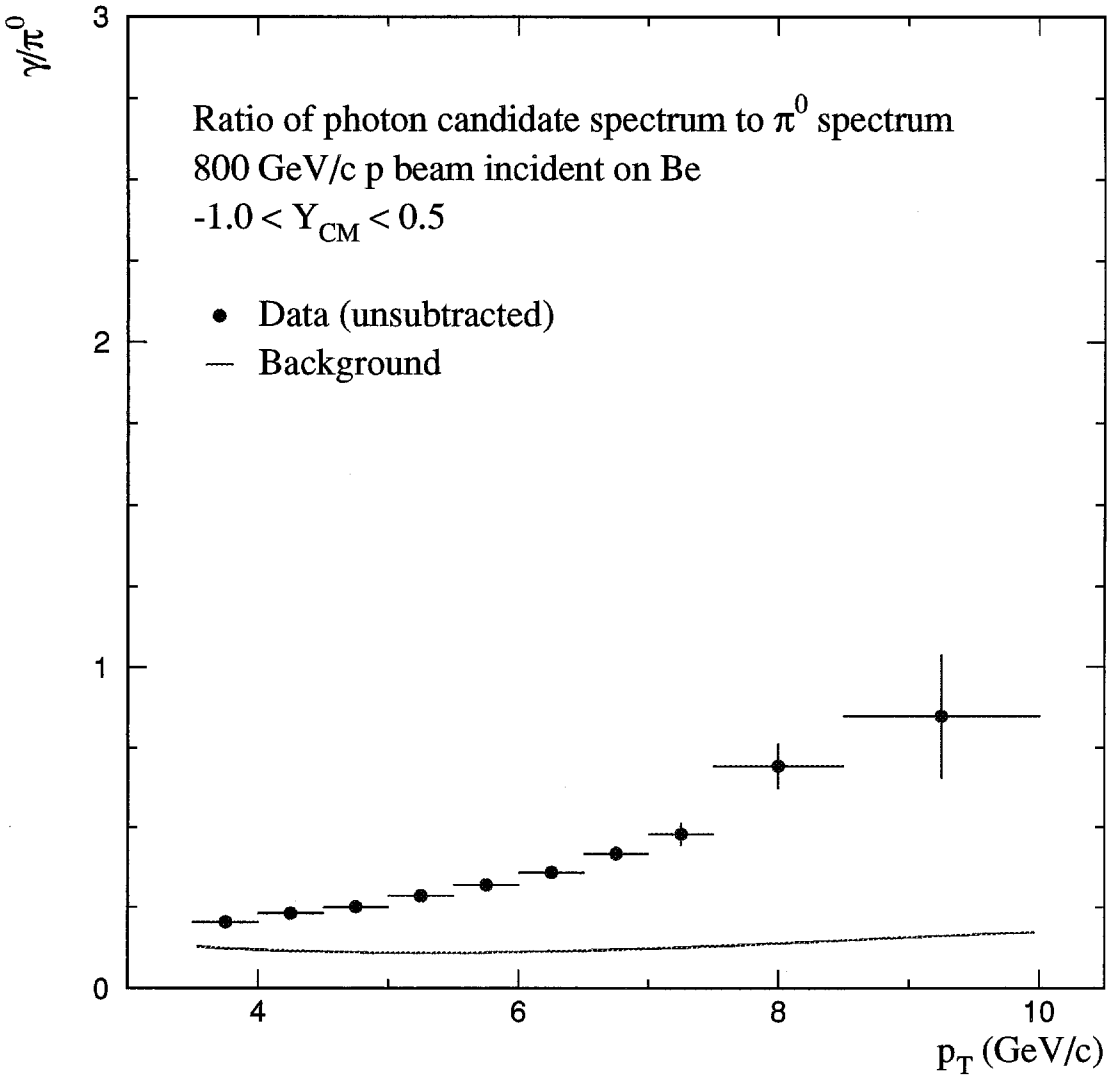

Figure 7.10 The data (points) and Monte Carlo (curve) γ/π^0 ratio as a function of p_T for 800 GeV/c proton beam incident on a beryllium target.

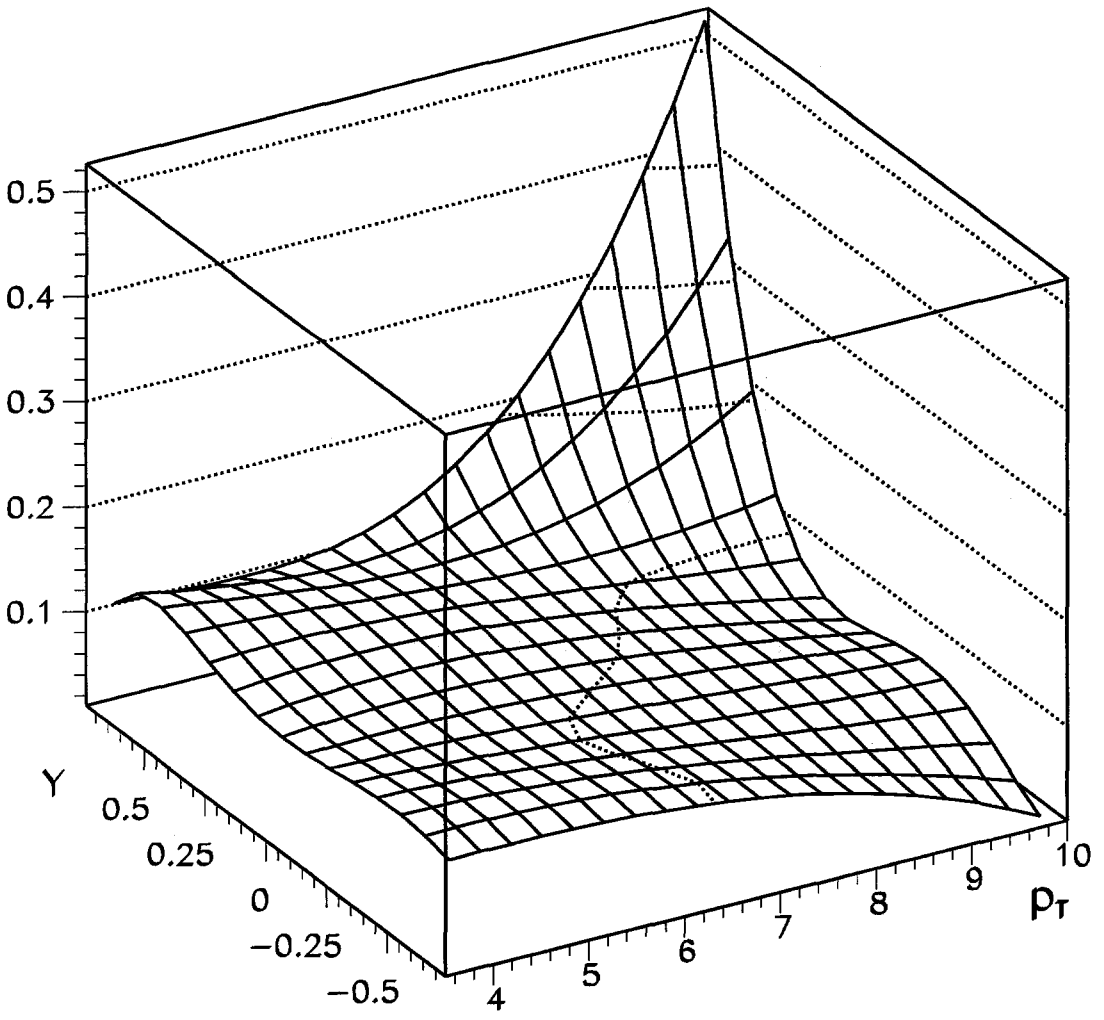

Figure 7.11 Fit to background γ/π^0 as a function of y_{cm} and p_T.

- For direct photons: $N^{corr} = N^{\gamma}_{true} = N^{\gamma}_{Data} - (N^{\gamma}/N^{\pi^0})_{MC} N^{\pi^0}_{Data}$
- ρ is the density of the target material
- l is the length of the target
- N_a is Avogadro's number
- ABS is the beam absorption correction
- LTB is the live triggerable beam (see section 7.3.1)

In addition to the previously discussed corrections for muon rejection cuts, the following corrections have been applied to obtain N^{corr}:

- The geometric acceptance correction (see section 7.3.2)
- The trigger correction (see section 7.3.3)
- The conversion correction (see section 7.3.4)
- The efficiency correction (see section 7.3.5)

7.3.1 LTB

The live triggerable beam is defined as the number of beam particles incident on the target during the time the spectrometer is ready to accept triggers. The live triggerable beam is determined from various scalers which were readout after each spill during the data taking process. It can be expressed in the form:

$$\mathrm{LTB} = \mathrm{BEAM1} \otimes \overline{\mathrm{BH}} \otimes (\mathrm{LiveFraction})$$

where

Live Fraction = (Clean Interaction Fraction) * (Computer Live Fraction) *

(Pretrigger Live Fraction) * (Veto Live Fraction)

- Clean Interaction Fraction is the fraction of interactions that are not vetoed by the clean interaction requirement in the trigger. This clean interaction requirement rejected interactions within 60 nsec of each other.

- Computer Live Fraction is the fraction of interactions for which the data acquisition system was ready to accept triggers.

- Pretrigger Live Fraction is the fraction of interactions for which the pretrigger logic was not already busy.

- Veto Live Fraction is the fraction of interactions not vetoed by either a hit in the veto walls or the power supply noise spike or the detection of early p_T.

7.3.2 Acceptance Correction

Since showers that fall outside the fiducial region of the EMLAC are excluded, a number of π^0's, η's and direct photons are lost. A simple Monte Carlo program was used to correct for this acceptance loss. No shower development or reconstruction was simulated in this simple program. This Monte Carlo was independent of the Monte Carlo used for the rest of the analysis. Separate corrections were determined for direct photons, π^0's and η's.

Direct Photons: Single direct photons were generated inside the target volume. Their trajectories were projected on to the front face of the EMLAC. The acceptance correction is given by the ratio of the total number of photons generated to the number of photons whose point of intersection with the EMLAC lies within the fiducial region. The correction was determined as a function of p_T,

pseudorapidity, Z-position of the vertex (V_z) and the transverse distance of the vertex from the EMLAC axis. Figure 7.12 shows the geometric acceptance for direct photons as a function of center-of-mass rapidity (the acceptance correction is the inverse of the geometric acceptance).

π^0's: As in the case of direct photons, single π^0's are generated in the target area. Their decay to two photons is simulated uniformly in asymmetry, with A < 0.75. Both photons from the π^0 decay are checked to determine whether they would hit the EMLAC within its fiducial volume. Both photons are required to intersect the same octant to be considered accepted. This requirement accounts for the fact that in reconstructing the π^0 signal in data only same-octant photon combinations are considered. Thus, π^0's whose decay photons land in different octants are "lost". The acceptance correction for π^0's is given by the ratio of the total number of π^0's generated to the number of π^0's for which both photons would intersect the same octant and both photons are within the fiducial volume of the EMLAC. This correction is evaluated as a function of p_T, pseudorapidity, V_z and the transverse distance of the vertex from the EMLAC axis. Figure 7.13 shows the geometric acceptance for π^0's as a function for center-of-mass rapidity for different bins in p_T.

η's: The acceptance correction for η's was evaluated in a fashion identical to that of the π^0 sample.

7.3.3 Trigger Corrections

As described in Sec. 3.4, E706 has a multi-threshold trigger system. The ideal trigger would behave as a step function at a given threshold. However, due to the response characteristics of a real device, a trigger does not exhibit an ideal step function response. The trigger response closely approximates a step function, but

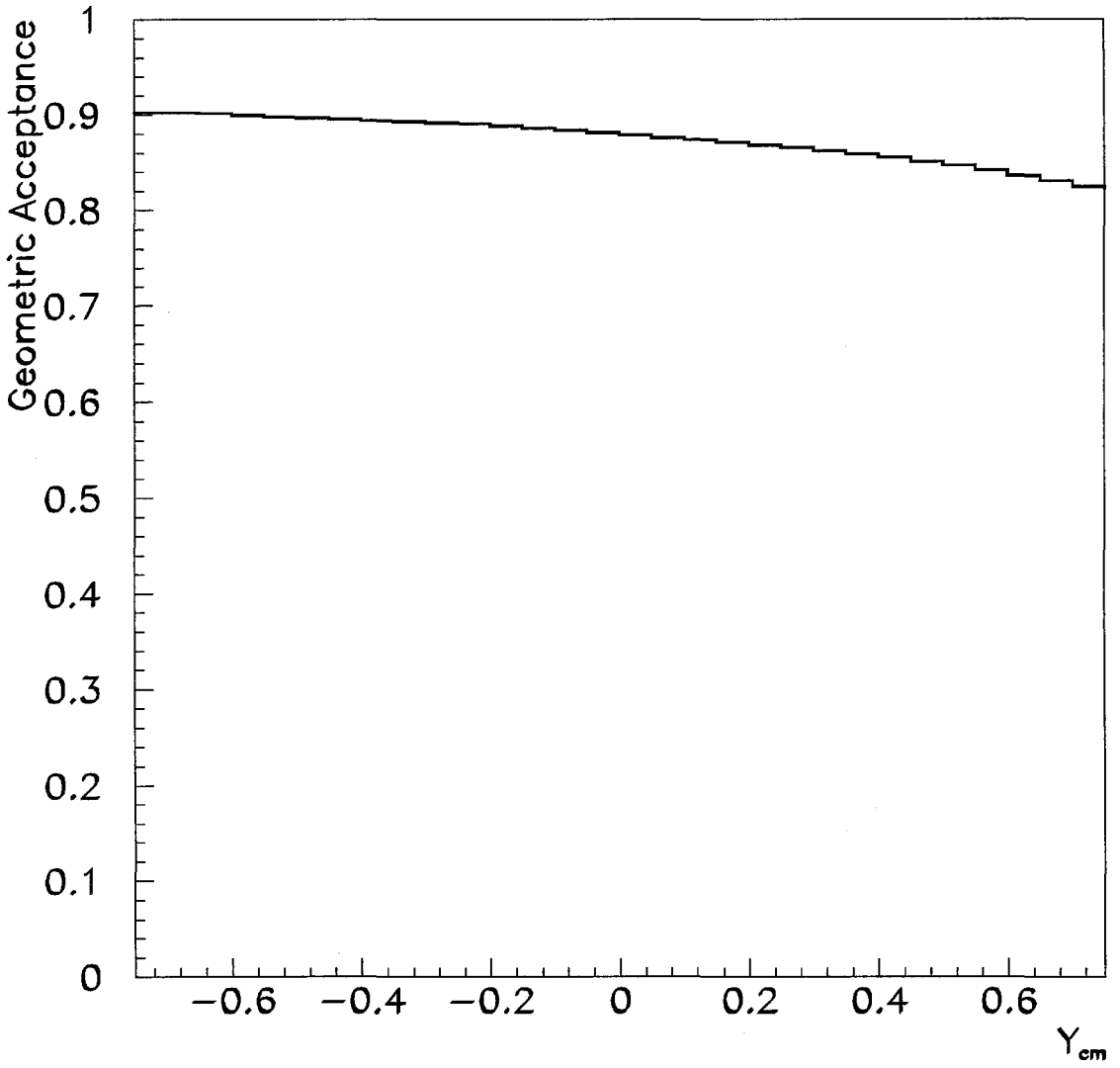

Figure 7.12 The geometric acceptance for direct photons shown as a function of center-of-mass rapidity.

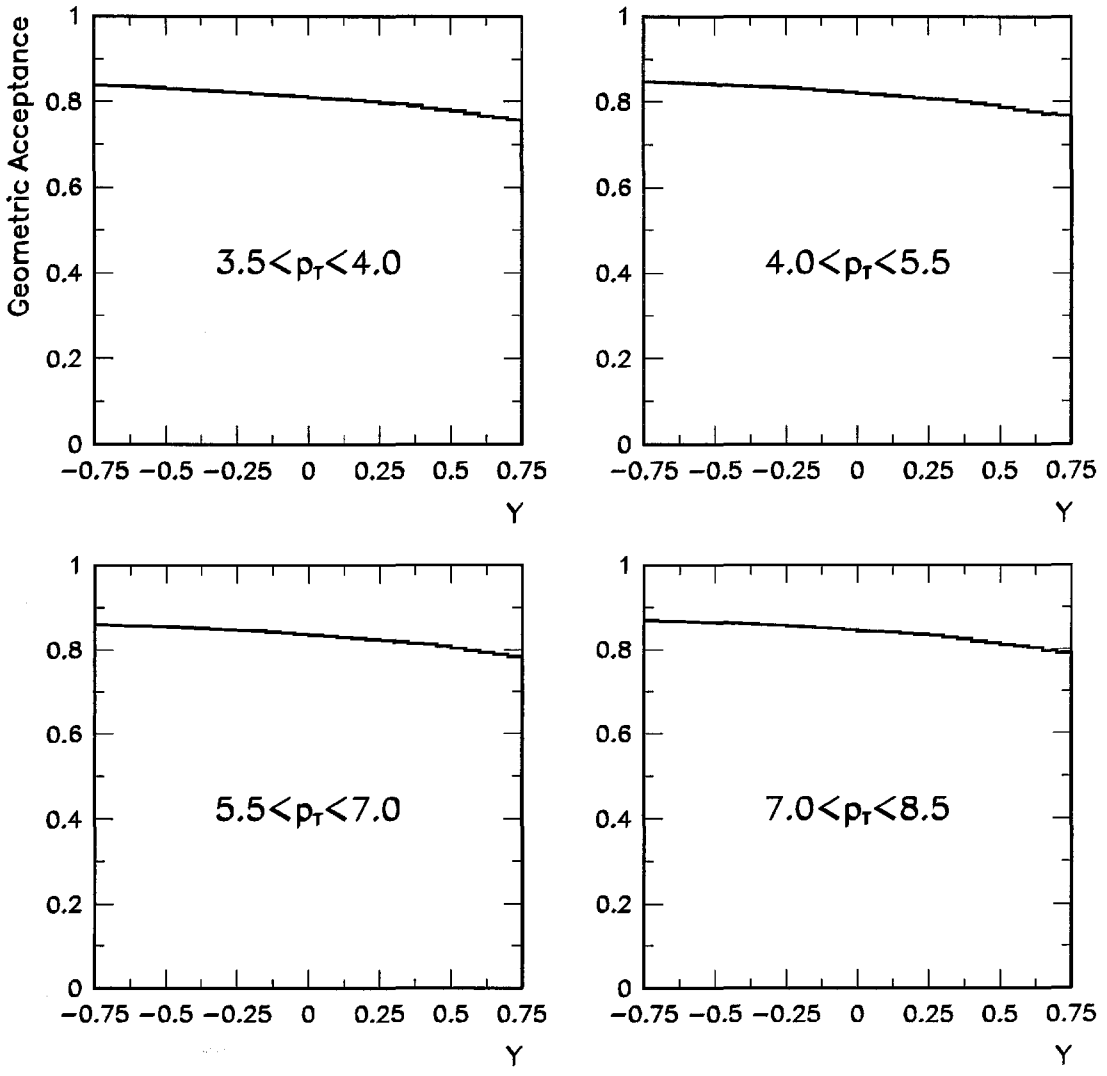

Figure 7.13 Geometric acceptance for π^0's as a function of the π^0's rapidity for several different π^0 p_T ranges.

there is a transition or 'turn-on' region where the probability of firing the trigger and thus accepting the event is neither zero nor 100%. This can seriously bias the p_T spectrum in the trigger threshold region since events are being selected only a fraction of the time they are being produced. Two approaches can be taken to address this issue. One is to cut high enough in p_T so that the trigger probability is 100% and one does not need to worry about the turn-on region (except to verify its extent). On the other hand, one could carefully evaluate the probability that a given energy deposition will satisfy the trigger and then correct for the losses. The first approach is fine as long as there is enough overlap between the triggers, i.e., the lower threshold (generally prescaled) trigger does not run out of statistics before the higher threshold trigger becomes fully efficient. The second approach, which was adopted by E706, affords more flexibility as triggers can be used in both their turn-on and fully efficient regions.

The performance of both the local and global aspects of the triggers were studied independently. For locals, the trigger probability was evaluated for each triggered octant for each event based upon the energy reconstructed in that octant. Each octant was divided into 31 local sections (groups of sixteen strips with eight overlapping) and turn-on curves were measured separately for each of the corresponding local discriminators so that the local trigger probabilities could be evaluated. The basic technique for determining these turn-on curves was the following:

- Runsets: The data sample was divided into subsets of constant trigger performance, in terms of threshold settings and hardware response. Data within such a runset was combined to evaluate a turn-on curve per section, which was valid over the whole range of that particular runset. One turn-on curve per runset was measured for each of the 31 sections in each of the eight octants.

• Sample Selection: A sample of events, unbiased with respect to the trigger being analysed were selected. For the high threshold (around 4.5 GeV/c) triggers this amounted to selecting a sample based upon satisfying the lower threshold (around 3 GeV/c) triggers. For the low threshold triggers a "opposite octant" sample was identified. For each high-triggered octant an evaluation of the p_T contained in the remaining seven octants was done. The octant containing the largest amount of p_T (other than the high-triggered) octant was designated as the "opposite octant". The reason for calling this the "opposite octant" sample is that most of the entries actually come from opposite octants of events selected by the high p_T trigger.

• Sums-of-8: For each section, the strip energies were weighted by the corresponding gain values and summed over the 16 R-strips in that section. The gains applied were the same as those used by the online trigger. Since the gains are approximately set for $\sin\theta$ weighting this weighted sum over 16 R-strips was approximately the trigger-p_T corresponding to the particle which deposited the energy. It is different from the actual p_T of the incident particle because no energy corrections (as described in Chapter 5) are applied to the strips in evaluating the Sums-of-8. This is done to simulate the online trigger response. At the time the trigger decision was made the signals that were sent to the online trigger were uncorrected for the dependences discussed in Chapter 5.

• Trigger Probability: The probability of firing or trigger efficiency is (as a function of p_T) now just the fraction of times the discriminator fired for that trigger-p_T (see Figure 7.14). (The status of the discriminator for each section was recorded in an independent latch readout and written out for each triggered event.) The inverse of this probability provides the weights which can be used to account for events not selected by the trigger at that particular trigger-p_T. To

facilitate this, the trigger probability for each section is parametrized by fitting to an error function which can be queried, for a given octant and trigger-p_T, to yield the probability of firing the trigger. Since the status of the local trigger in an octant is dependent on the status of each of the 31 sections, the probability of firing a local trigger for a given octant is given by:

$$P = 1 - \Pi(1 - p_i)$$

where p_i is the probability of firing section i.

For global triggers the same general technique is employed, however, there are some differences. Apart from the fact that the global trigger turn-on curves are measured as a function of the total trigger-p_T contained in the octant, a cutoff is applied to contributions to each sums-of-8. This cutoff simulates the hardware cutoff installed in this trigger to minimize sensitivity to coherent noise influencing the trigger-p_T estimation.

7.3.4 Conversion Correction

As mentioned earlier some of the photons convert to e^+e^- pairs during their passage through matter. If this conversion occurs downstream of the magnet the position and energy of the resulting showers is approximately the same as that of the original photon. However, if the conversion occurs before the magnet the electron and positron are swept out in different directions splitting the energy of the original photon into two distinct showers resulting in the "loss" of the original particle whether it be a direct photon, or a photon from π^0 or η. To compensate for this loss, a correction based on the conversion probability, evaluated using the position of the reconstructed vertex and the number of radiation lengths traversed

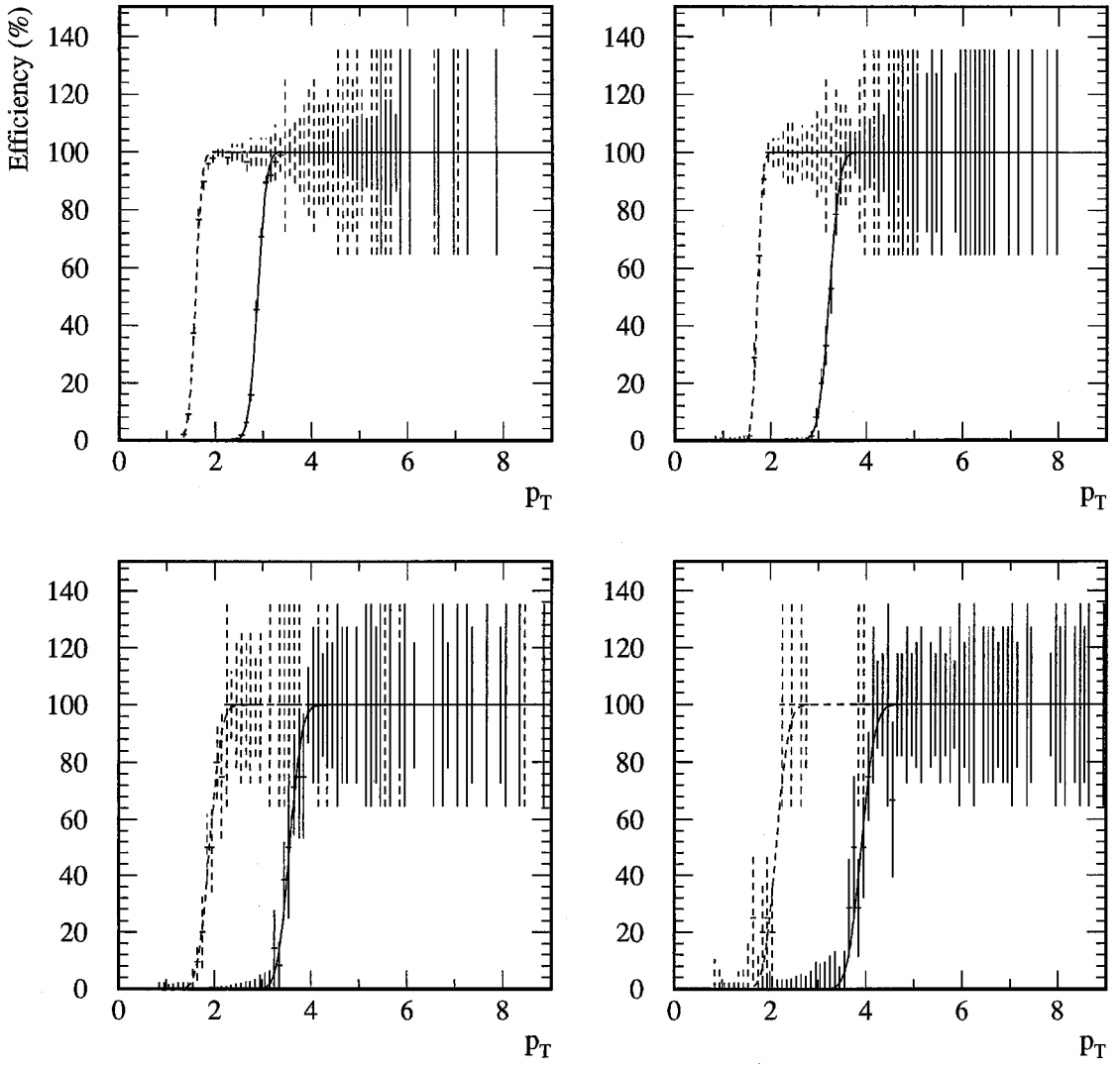

Figure 7.14 Single Local High (solid) and Single Local Low (dashed) trigger efficiency for inner (top two) and outer (bottom two) sections of an octant as a function of trigger-p_T.

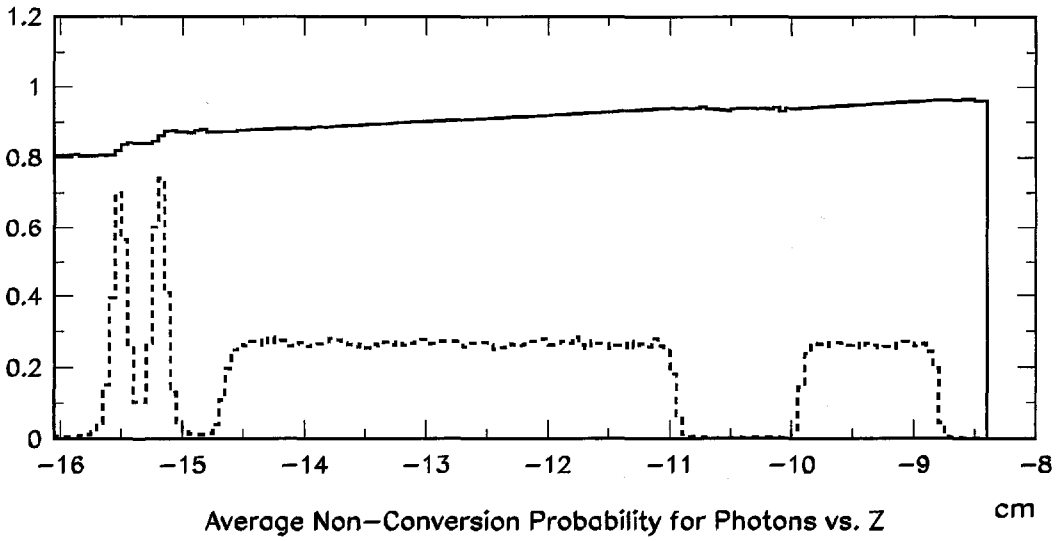

Figure 7.15 Average non-conversion probability for photons as a function of Z in the target region. The target is overlayed for comparison.

by the detected photon, is calculated. Figure 7.15 shows the average probability that a photon will not convert during its passage through the target region of as a function of the location the photon was produced.

7.3.5 Efficiency Correction

The efficiency was evaluated independently for π^0's, η's and direct photons using the detailed Monte Carlo simulation. Let us first consider the π^0 efficiency in detail, as the general procedure is very similar for all three particle species.

The π^0 efficiency is defined as the ratio of the number of π^0's reconstructed in a p_T and rapidity bin to the number generated in that bin. The efficiency defined in this fashion corrects for reconstruction losses and also takes into account the

effects of the EMLAC energy resolution. Alternatively one could have defined the π^0 efficiency as the number of π^0's reconstructed to the total number generated irrespective of what p_T and rapidity they had upon reconstruction. This definition calculates correctly the pure *reconstruction* efficiency but does not account for the effects of smearing on steeply falling cross sections which would then need to be addressed via another correction.

Number Reconstructed

The numerator, or the number reconstructed, was found using the following requirements:

- Presence of a reconstructed vertex within the target region
- Reconstructed mass for the diphoton combination within the π^0 signal region
- Both reconstructed photons of the π^0 within the fiducial region of the EMLAC
- Both the photons should have reconstructed $E_{front}/E_{total} > 0.2$
- Reconstructed energy asymmetry of the pair < 0.75
- Sideband subtraction was done for statistical background removal

Entries which pass the preceding requirements are stored in a 2-D p_T-y histogram.

Number Generated

The denominator, or the number of π^0's generated, is subjected to the following requirements:

- Presence of a reconstructed vertex within the target region
- Both generated photons within the fiducial region of the EMLAC
- Generated energy asymmetry of the pair < 0.75
- Neither of the photons from the π^0 decay converted before the magnet

Entries that satisfy the preceding requirements are stored in a 2-D generated p_T-y histogram.

The reconstructed 2-D histogram is now divided by the generated 2-D histogram and the ratio is fitted to a smooth two dimensional surface in p_T and rapidity (see Figure 7.16). The efficiency correction is given by the inverse of this surface.

The efficiency calculated in the fashion described above is referred to as the "untriggered" efficiency. In addition to the untriggered efficiency, "triggered" efficiencies were also evaluated (see Figure 7.17). To obtain the triggered efficiencies, along with the cuts outlined above, an additional condition is imposed on the number reconstructed. That is to require that the calculated trigger probability for the trigger octant be greater than ten percent. This is done to avoid huge trigger weights on individual data events with very low trigger probability. Thus, the procedure of correcting for the trigger, on an event-by-event basis, is carried out for trigger efficiencies greater than 10%. Below that, the data is rejected and the average trigger corrections are absorbed into the efficiency.

The η efficiencies are evaluated in a fashion identical to the π^0 efficiencies.

The direct photon efficiencies are determined using a specialized Monte Carlo. It is special in the sense that instead of the general $2 \longrightarrow 2$ QCD hard scatter

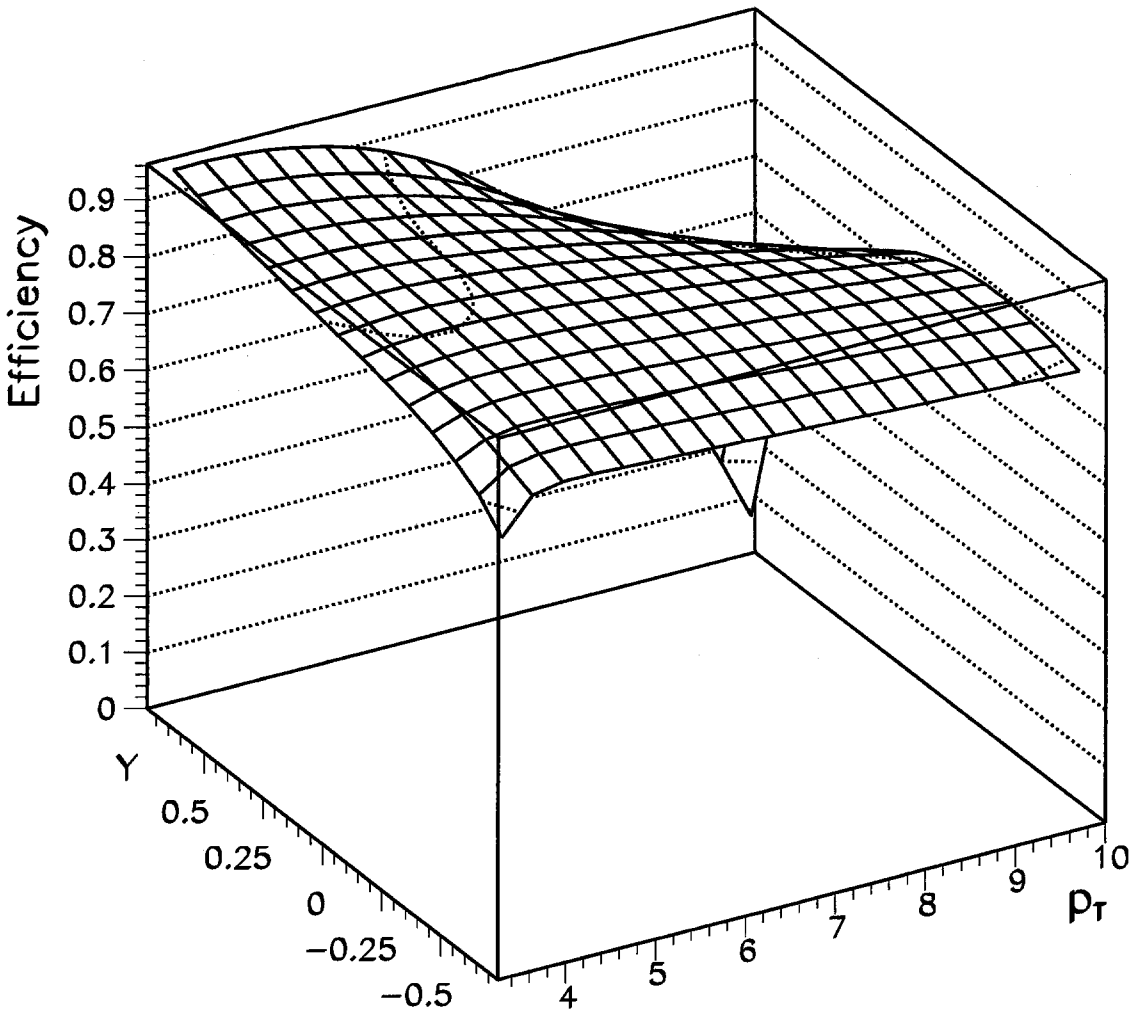

Figure 7.16 Untriggered reconstruction efficiency for π^0's as a function of y_{cm} and p_T.

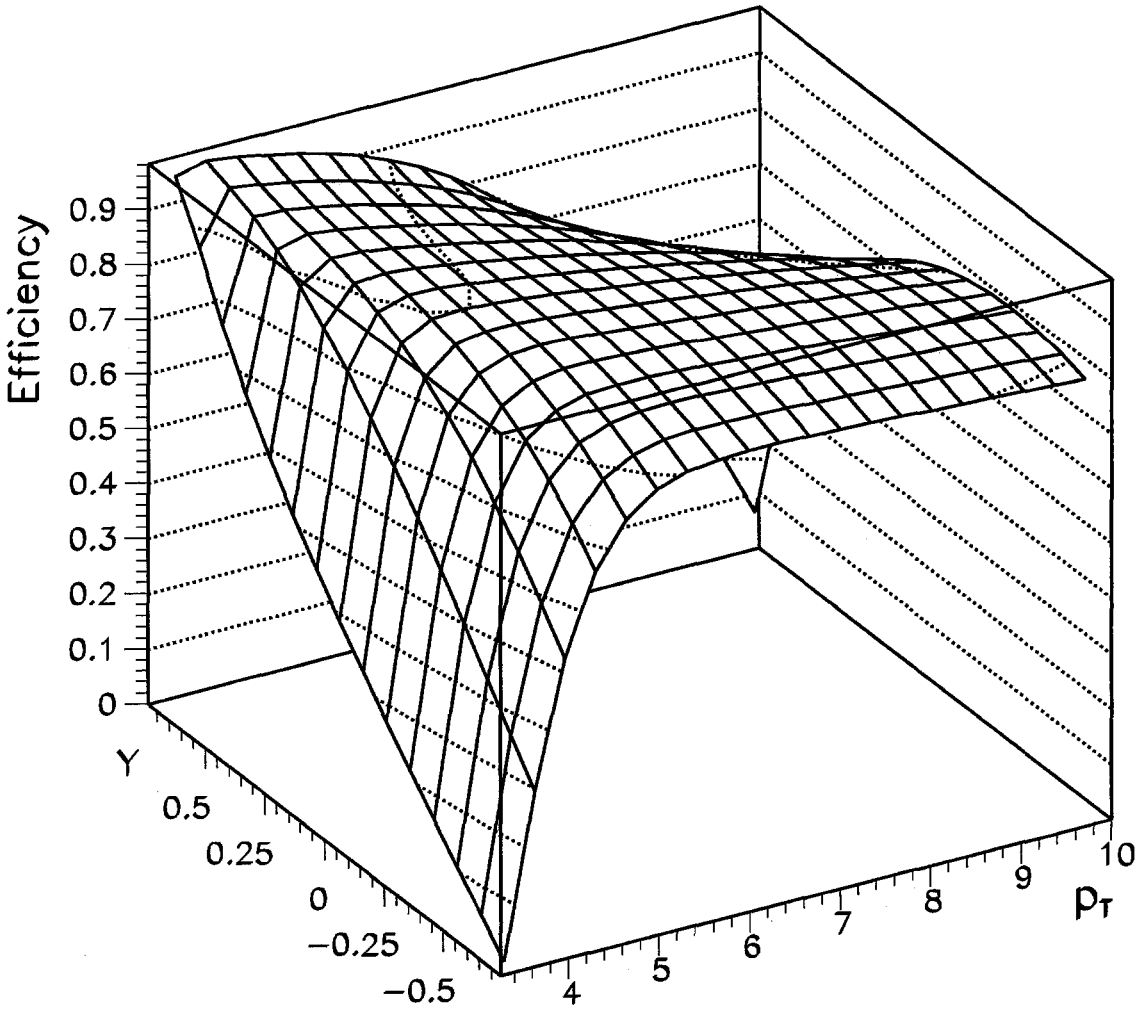

Figure 7.17 Triggered reconstruction efficiency for π^0's as a function of y_{cm} and p_T.

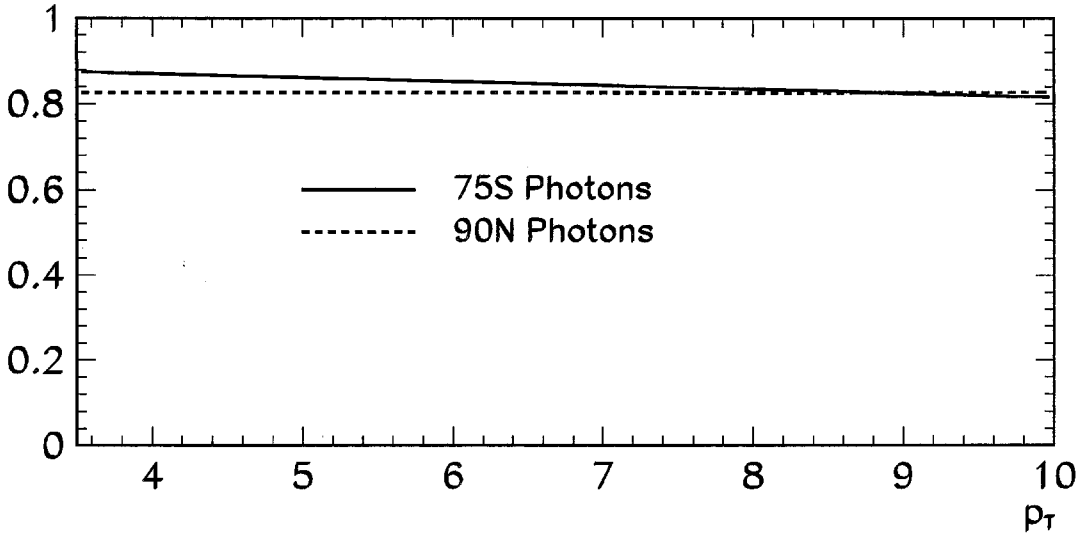

Figure 7.18 The reconstruction efficiency for direct photons as a function of the p_T of the photon for two different definitions of the direct photon.

Monte Carlo, used for evaluating the meson efficiencies and the background contribution to the direct photon signal, the direct photon process is specifically turned on in HERWIG event generator. Figure 7.18 shows the direct photon efficiencies for the 90n and 75s definitions. It may be noticed that the direct photon efficiencies away from the turn on region are lower than the corresponding meson efficiencies. This is due to the fact that the single photon energy scale is $\approx$ 0.75% lower that the diphoton scale. This is largely attributed to a reconstructor effect, having to do with separation between the photons.

Chapter 8 Results

This chapter presents results on direct photon and π^0 production using techniques outlined in the previous sections.

8.1 Cross Sections

This section presents results on inclusive direct photon and π^0 cross sections, in a graphical format, for π^- and proton beams incident on a Be target. (Qualitatively, the cross sections on Cu and hydrogen show very similar trends. A quantitative comparison of the direct photon and π^0 production from various targets is presented elsewhere [27].) The abscissa value for each of the points is determined by calculating the mean p_T in the bin based on an exponential fit to the cross section. The errors shown on the plots are statistical only. (Current estimates of systematic uncertainty are $\approx \pm 16\%$ for π^0's and $\approx \pm 22\%$ for direct photons. The major sources of this systematic uncertainty being normalization, energy calibration, efficiencies, signal definition/background subtraction and the trigger.)

Figure 8.1 shows the direct photon and π^0 inclusive cross sections per nucleon, for the 515 GeV/c π^- beam incident on a beryllium target, as a function of p_T averaged over 1.5 ($-0.75 < Y_{CM} < 0.75$) units of rapidity. The π^0 cross section has been scaled by a factor of 0.001 for purposes of graphical presentation. The curves overlaid on the plots are NLL QCD calculations using as input the ABFKW [28, 29] and CTEQ3M [30] parton distribution functions. The calculations for the direct photon cross sections were performed using the package developed by Qiu (unpublished) which is based on the earlier calculation by Aurenche *et al.* [31]. The π^0 calculation was performed using the package from Aversa *et al.* [32]. In

addition to the parton distribution functions, for π^0's, the BKK [33] fragmentation functions are used. The cross section calculations are shown for two choices of scale, $Q = p_T$ and $Q = p_T/2$. Since beryllium is a nuclear target, the theory has been adjusted for measured nuclear dependence effects. For π^0's the nuclear enhancement is of order 27%, while for direct photons it is of order 12%.

Figure 8.2 shows the direct photon and π^0 inclusive cross sections per nucleon, for the 530 GeV/c p beam incident on a beryllium target, as a function of p_T averaged over 1.5 (-0.75 $< Y_{CM} <$ 0.75) units of rapidity. The π^0 cross section has been scaled by a factor of 0.001 for purposes of graphical presentation. The curves overlaid on the plots are NLL QCD calculations using the CTEQ3M parton distribution functions. For π^0's, the BKK fragmentation functions are used. The cross section calculations are shown for two choices of scale, $Q = p_T$ and $Q = p_T/2$. In addition, the theory has been adjusted for nuclear dependence effects.

Figure 8.3 shows the direct photon and π^0 inclusive cross sections per nucleon, for the 800 GeV/c p beam incident on a beryllium target, as a function of p_T averaged over 1.5 (-1.0 $< Y_{CM} <$ 0.5) units of rapidity. The π^0 cross section has been scaled by a factor of 0.001 for purposes of graphical presentation. The curves overlaid on the plots are NLL QCD calculations using the CTEQ3M parton distribution functions. For π^0's, the BKK fragmentation functions are used. The cross section calculations are shown for two choices of scale, $Q = p_T$ and $Q = p_T/2$. The theory has been adjusted for nuclear dependence effects.

A few comments can be made regarding the comparison of NLL QCD calculations to the measured cross sections:

- The theory predictions are very sensitive to choices of factorization (μ_F) and renormalization (μ_R) scales. In principle, a complete prediction from theory

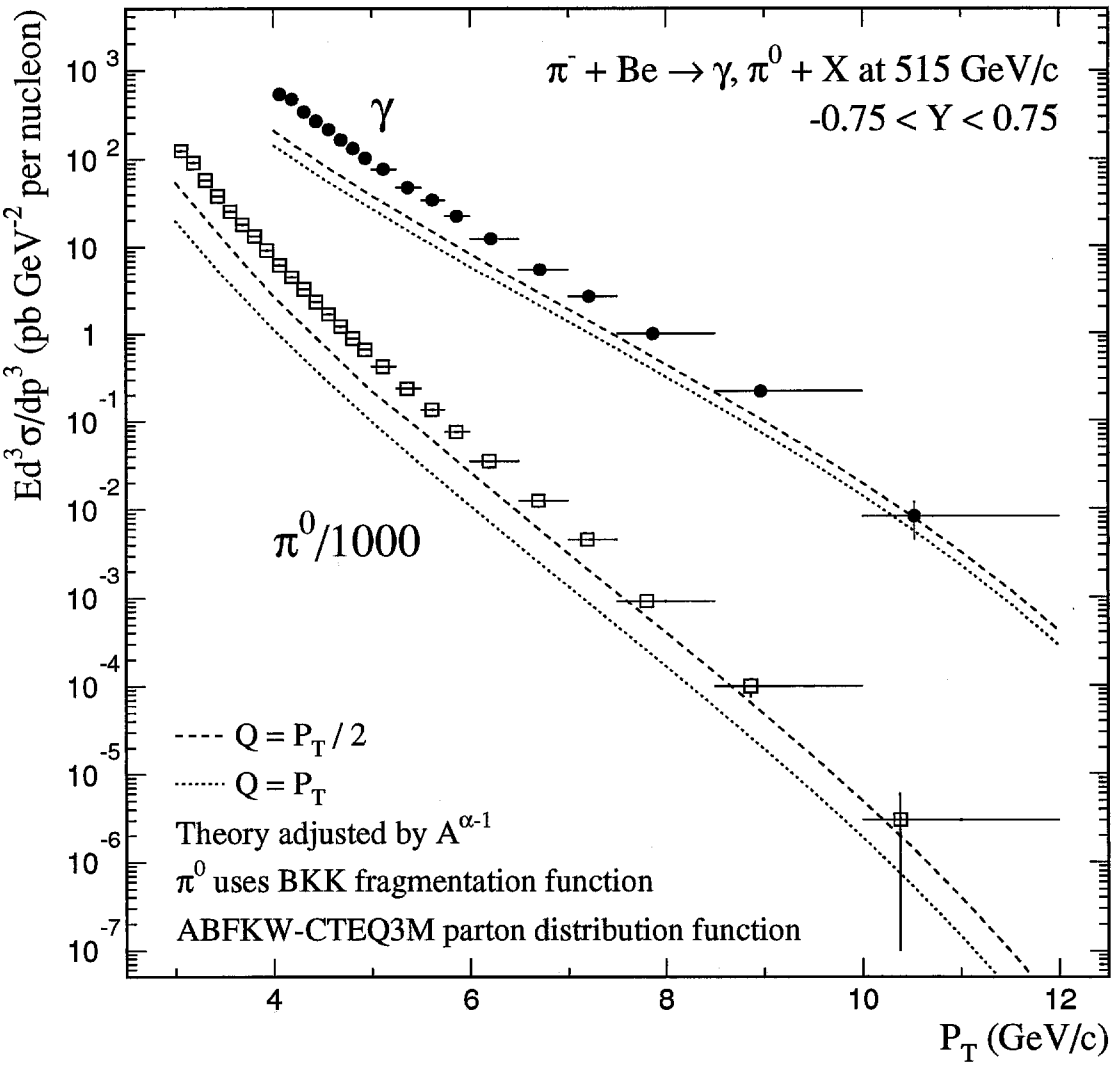

Figure 8.1 Invariant cross sections per nucleon for direct photon and π^0 production from 515 GeV/c π^- beam incident on a beryllium target. The curves are from NLL QCD calculations for two choices of scale ($Q = p_T$ and $Q = p_T/2$).

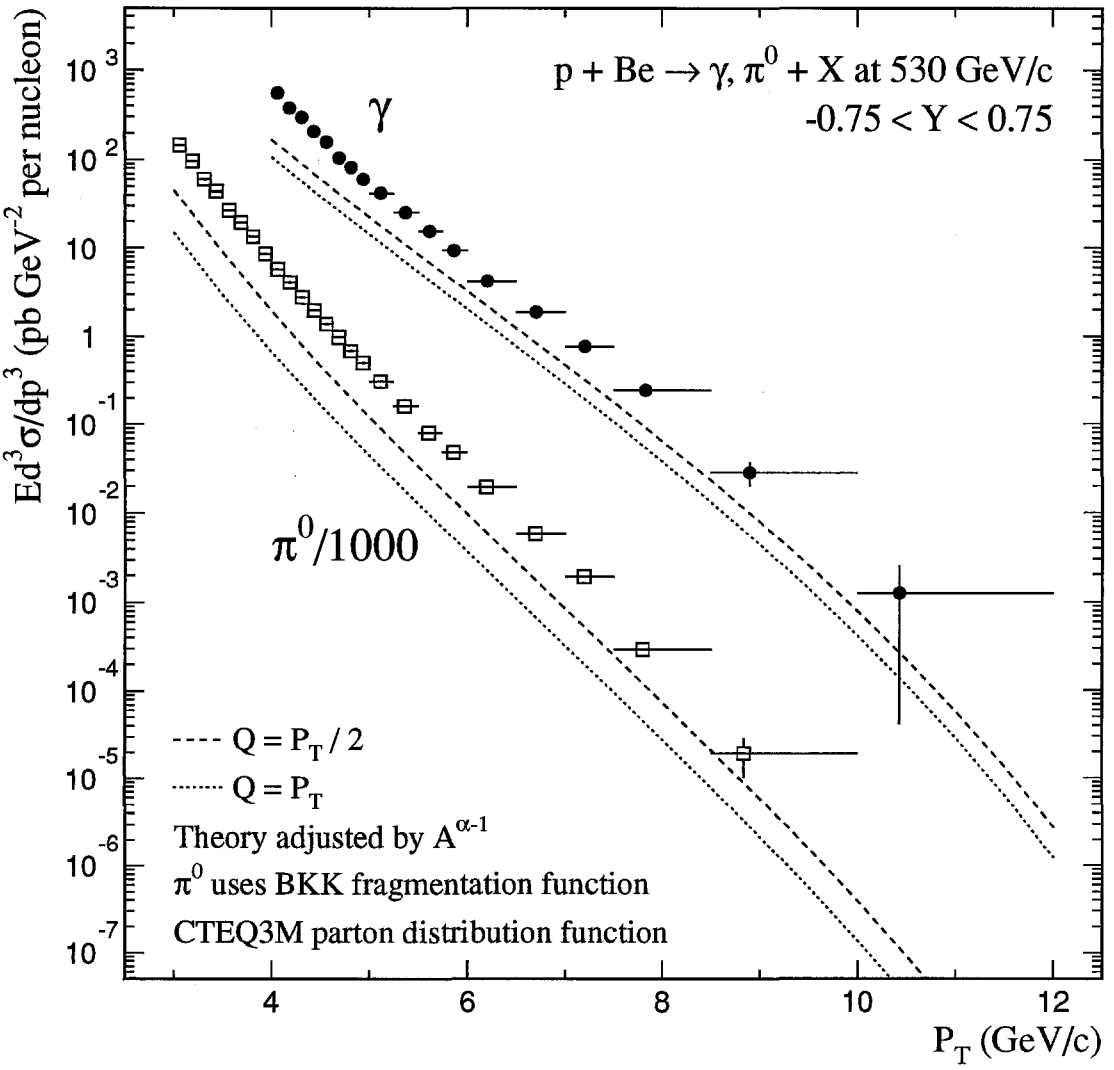

Figure 8.2 Invariant cross sections per nucleon for direct photon and π^0 production from 530 GeV/c proton beam incident on a beryllium target. The curves are from NLL QCD calculations for two choices of scale ($Q = p_T$ and $Q = p_T/2$).

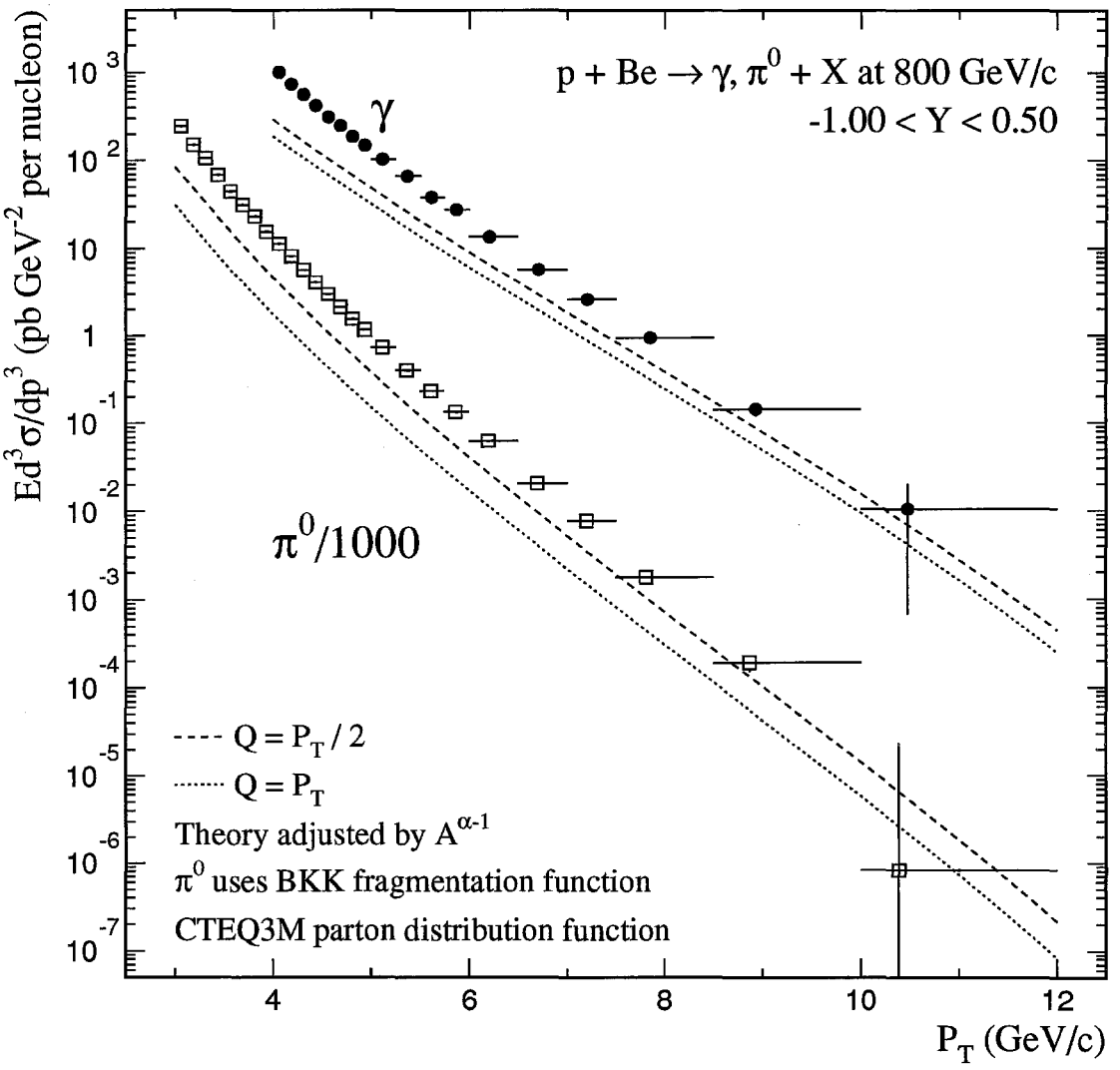

Figure 8.3 Invariant cross sections per nucleon for direct photon and π^0 production from 800 GeV/c proton beam incident on a beryllium target. The curves are from NLL QCD calculations for two choices of scale ($Q = p_T$ and $Q = p_T/2$).

should not depend on choices of scales. In practice, however this is generally not the case since the calculations are not performed to all orders. Figure 8.4 shows the sensitivity of the calculated cross sections to the choices of scales for direct photon production at 530 GeV/c for proton beam incident on a beryllium target. Also shown is the dependence of the cross section to different choices of parton distribution functions. The sensitivity of the cross section to various choices is presented in Figure 8.4 as the fractional difference in the resulting predictions when one of the inputs is varied while the others are kept constant. In addition to the factorization and renormalization scales, the π^0 calculation is also sensitive to the choice of fragmentation scale (m_F). Figure 8.5 shows the dependence of the calculated cross sections on the choices of scale and parton distribution functions, for inclusive π^0 production at 530 GeV/c with proton beam incident on a Be target.

• It is evident from Figures 8.4 and 8.5 that both the direct photon and π^0 cross section calculations show a significant dependence on choices of scale. Compared to them the dependence of the calculations on the choice of parton distribution functions is much smaller. Typically the variations are less than 20% for different choices of the parton distribution functions, but that may not be surprising in view of the fact that very similar data sets go into their determination.

• For reasonable or 'natural' choices of scale (of order p_T and $p_T/2$) the theory does not match the data very well. The data cross sections are higher than the theory evaluated with either of these two scale choices. Since the theoretical calculations evaluated with smaller scales yield higher cross sections, one option towards obtaining better agreement between data and theory is to choose smaller scales. For direct photons, even this does not yield good agreement between data and the theoretical calculations because after some point the calculated

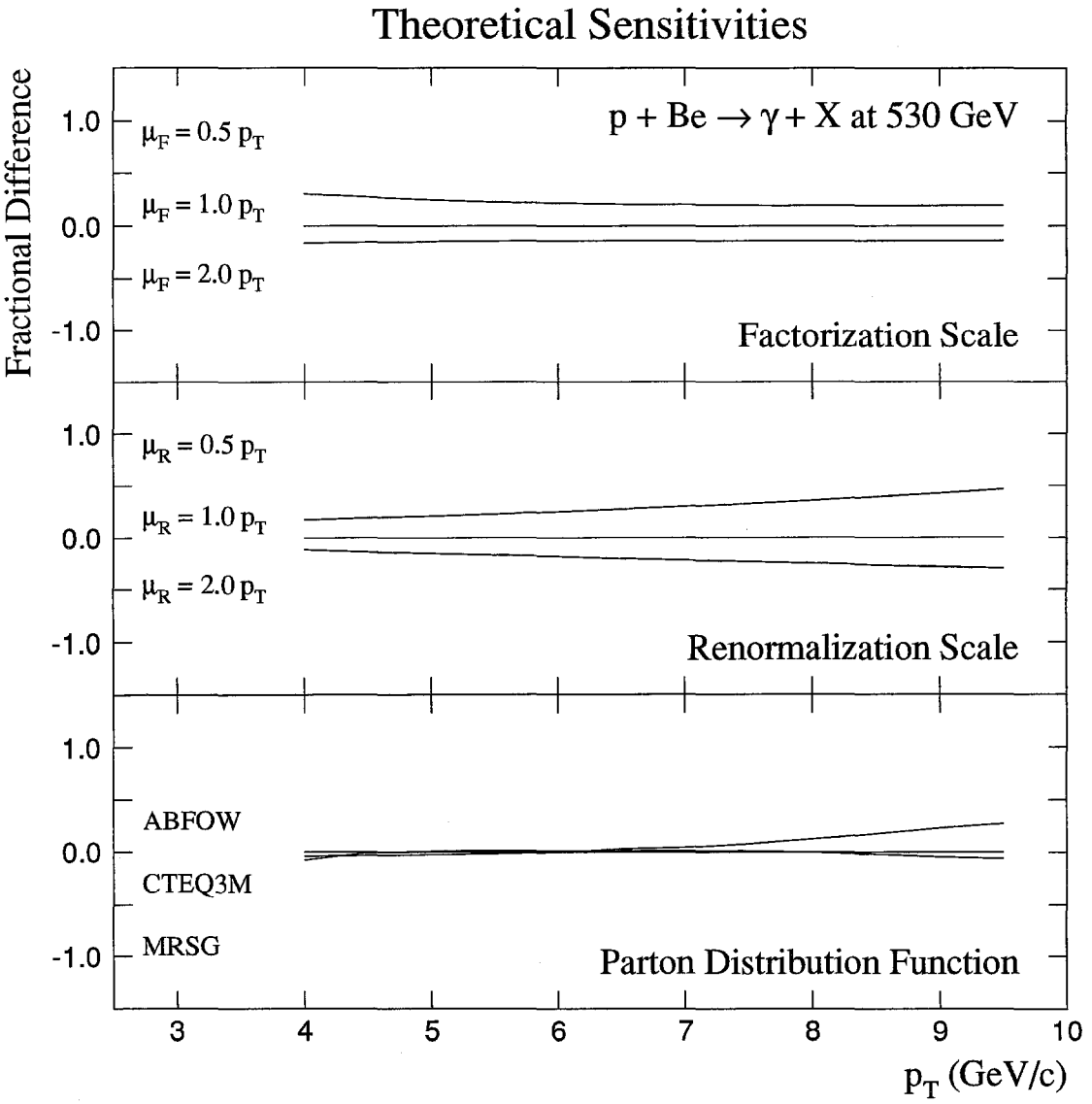

Figure 8.4 The fractional difference between γ cross-section calculations, illustrating the calculations' sensitivity to choice of factorization scale (top), renormalization scale (middle), and choices of a few recent parton distribution functions (bottom).

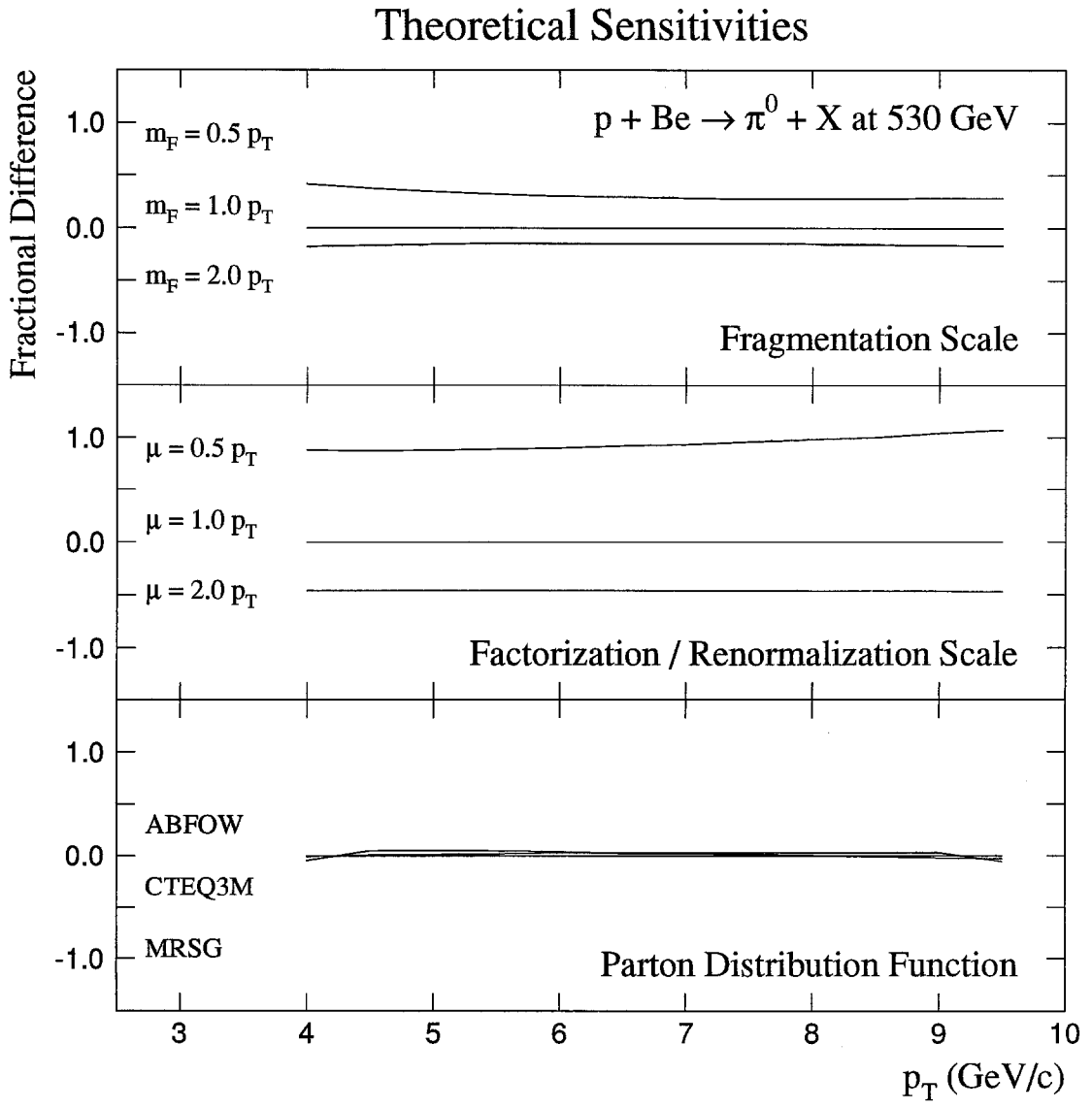

Figure 8.5 The fractional difference between π^0 cross-section calculations, illustrating the calculations' sensitivity to choice of fragmentation scale (top), factorization and renormalization scales (middle), and choices of a few recent parton distribution functions (bottom).

cross section value turns over and starts to decrease with decreasing scales. For π^0's, one can obtain agreement between data and the QCD calculations by tweaking the scales since there is an additional degree of freedom (the choice of the fragmentation scale). In both cases however, the situation is not very satisfactory since to get the QCD calculations anywhere close to the measured data cross section, one has to go to very low (of order $p_T/5$) scales where it is not even clear if perturbation theory is adequate. In any case, the large sensitivity of the theory to choices of scales indicates an inadequacy in the NLL theory calculations.

- Alternatively, it has been suggested that this discrepancy between data and the perturbative QCD calculations could be related to transverse momentum of the partons before the hard scatter (k_T) presumably due to initial state gluon radiation. Some of that is included in the NLL theory but the data indicates that the amount of radiation may be larger than accounted for in the calculations. Figure 8.6 through Figure 8.8 show the effect of incorporating an additional k_T smearing into the results for the three data sets. The data points on the plots are the same as in Figs. 8.1 through 8.3. The theory seems to match the data π^0 and photon cross sections well for a k_T value of around 1.4 GeV/c (for $Q = p_T/2$).

- While it is interesting that a k_T value of around 1.4 GeV/c gives a good agreement between data and theory, for both direct photons and π^0 for all beam types, it is not being claimed here as a measurement of k_T. (However, efforts are under way to directly measure the k_T value in data from this experiment by using away side fragmentation of jets, $\pi^0\pi^0$ and $\gamma\gamma$ events. Preliminary measurements yield values in the range 1.0 and 1.6 GeV/c.)

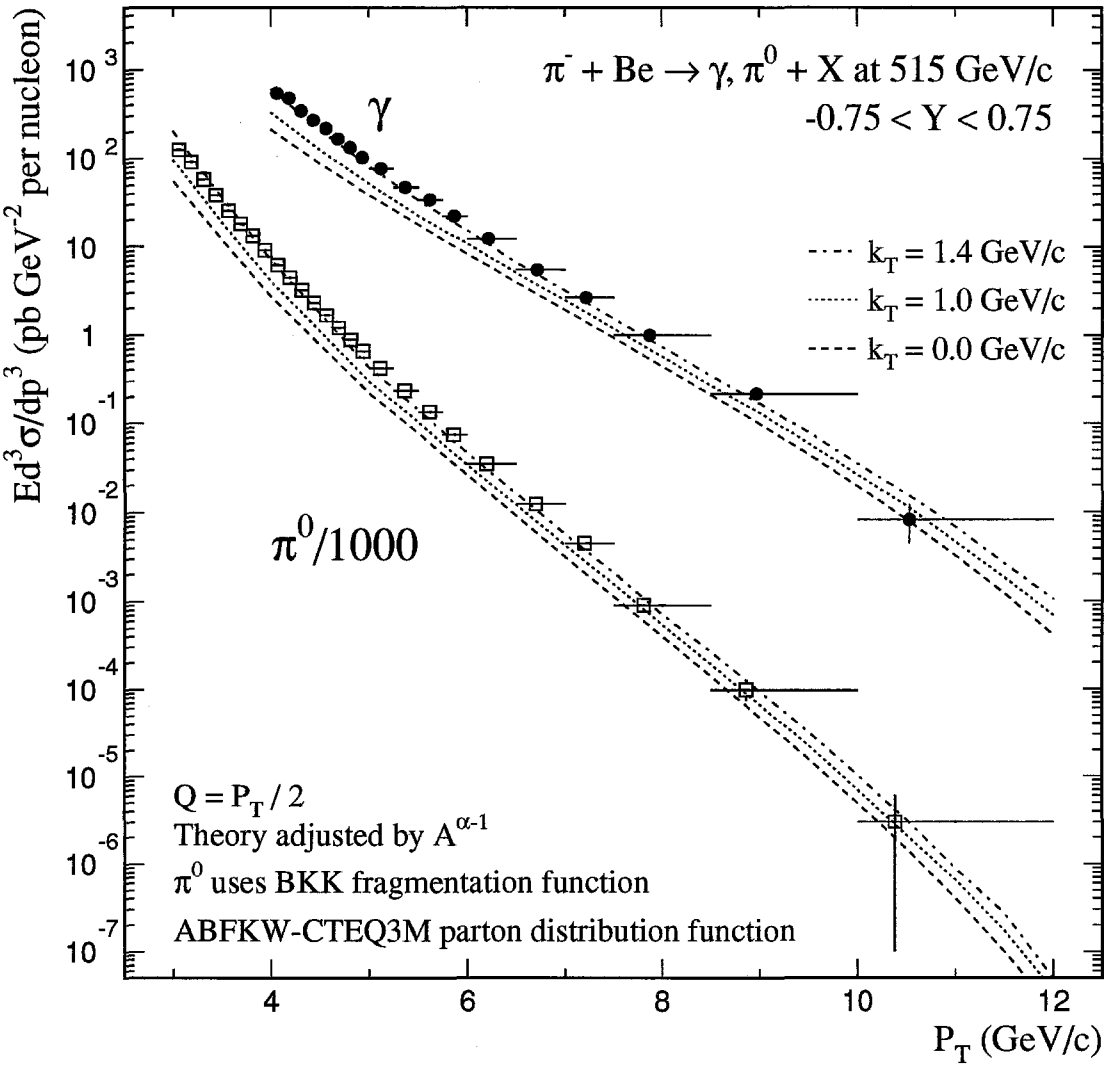

Figure 8.6 Invariant cross sections per nucleon for direct photon and π^0 production from 515 GeV/c π^- beam incident on a beryllium target. The curves are from NLL QCD calculations (with $Q = p_T/2$), supplemented by 0.0, 1.0 and 1.4 GeV/c of k_T respectively.

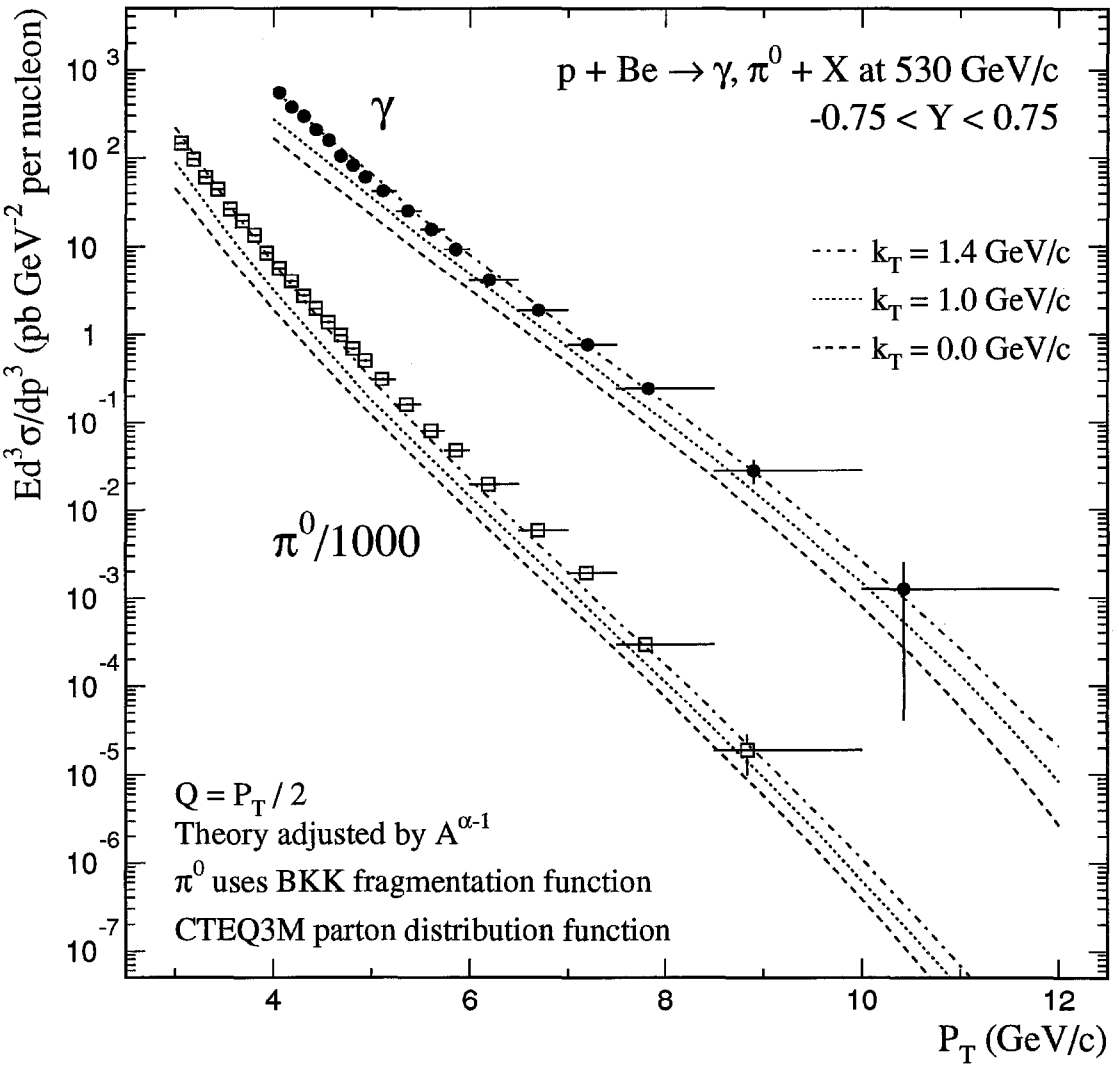

Figure 8.7 Invariant cross sections per nucleon for direct photon and π^0 production from 530 GeV/c proton beam incident on a beryllium target. The curves are from NLL QCD calculations (with $Q = p_T/2$), supplemented with 0.0, 1.0 and 1.4 GeV/c of k_T respectively.

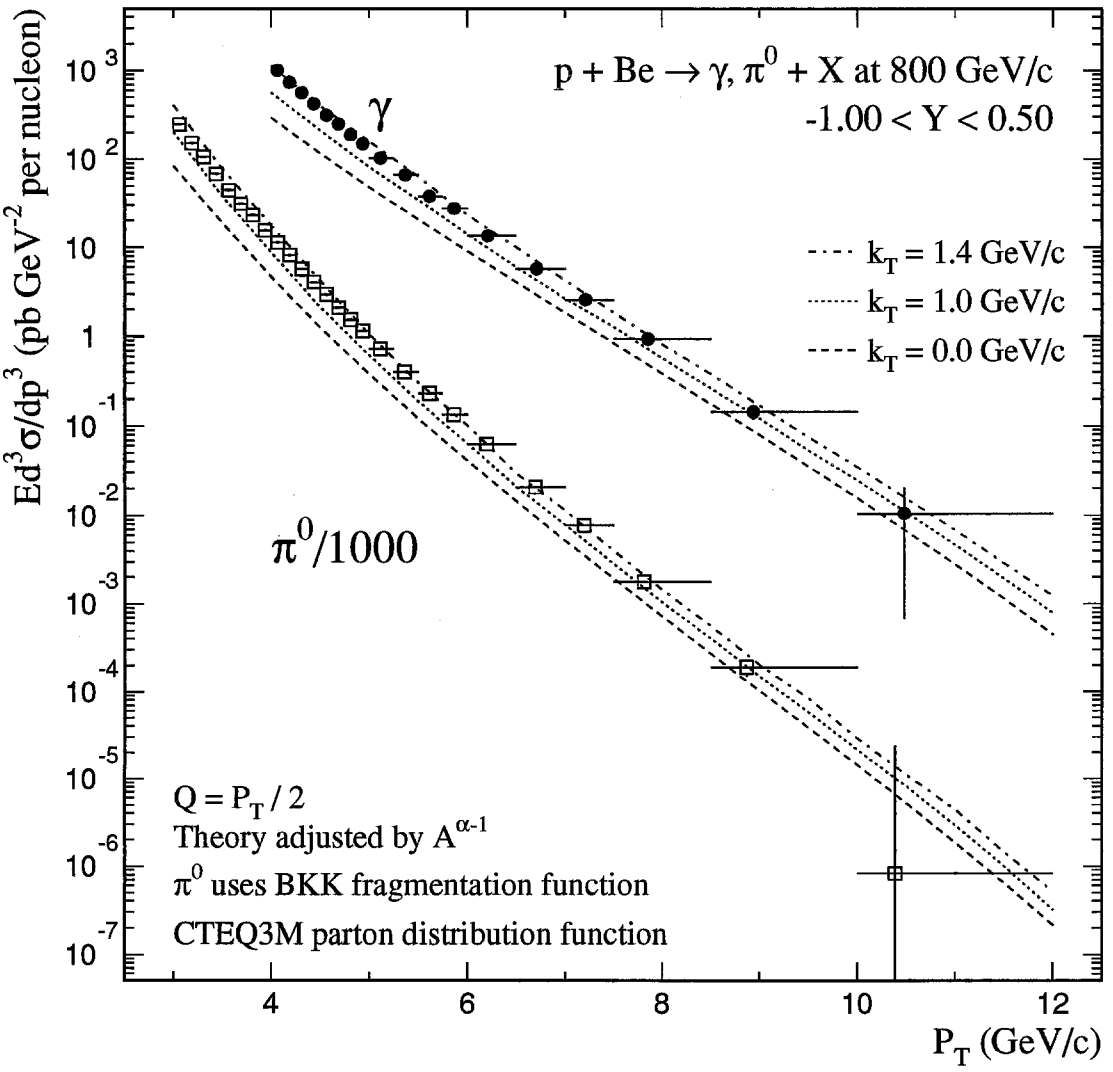

Figure 8.8 Invariant cross sections per nucleon for direct photon and π^0 production from 800 GeV/c proton beam incident on a beryllium target. The curves are from NLL QCD calculations (with $Q = p_T/2$), supplemented with 0.0, 1.0 and 1.4 GeV/c of k_T respectively.

8.2 Conclusions

This thesis presents results on direct photon and π^0 production with π^- (515 GeV/c) and proton (530 and 800 GeV/c) beams incident on a Be target. The inclusive cross sections were measured for p_T's above 3 GeV/c averaged over 1.5 units of rapidity. These data were collected by Fermilab experiment E706 during its 1990-91 fixed target run using a finely-segmented lead-liquid argon calorimeter for detection of photons and a precision tracking system for the detection of charged particles.

For reasonable choices of scales, the NLL QCD calculations do not match the measured data cross sections very well. In addition, the calculations exhibit significant sensitivity to choices of scale indicating a need for further theoretical efforts to effectively pin-down direct photon production calculations in this kinematic regime. When the NLL theory calculations are supplemented with an effective k_T or parton initial state transverse momentum of about 1.4 GeV/c, the results (for scales of $Q = p_T/2$) provide a reasonable match with the measured cross sections.

References

[1] E706 Collaboration, G. Alverson *et al.*, Direct Photon Production at High–p_T in π^-Be and pBe Collisions at 500 GeV/c, Phys. Rev. Lett. **68**, 2584 (1992).

[2] E706 Collaboration, G. Alverson *et al.*, Production of π^0 mesons at high p_T in π^-Be and pBe collisions at 500 GeV/c., Phys. Rev. D **45**, 3899 (1992).

[3] E706 Collaboration, G. Alverson *et al.*, Production of direct photons and neutral mesons at large transverse momenta by π^- and p beams at 500 GeV/c, Phys. Rev. D **48**, 5 (1993).

[4] E706 Collaboration, G. Alverson *et al.*, Structure of the recoiling system in direct–photon and π^0 production by π^- and p beams at 500 GeV/c, Phys. Rev. D **49**, 3106 (1994).

[5] I. J. R. Aitchison and A. J. G. Hey, *Gauge Theories in Particle Physics* (IOP Publishing Ltd, Bristol, England, 1989).

[6] G. Sterman *et al.*, Handbook of perturbative QCD, Rev. Mod. Phys. **67**, 157 (1995).

[7] J. F. Owens, Large-momentum-transfer production of direct photons, jets and particles, Rev. Mod. Phys. **59**, 465 (1987).

[8] T. Ferbel and W. R. Molzon, Direct-photon production in high-energy collisions, Rev. Mod. Phys. **56**, 181 (1984).

[9] P. Aurenche and M. Whalley, A Compilation of Data on Single Prompt Photon Production in Hadron–Hadron Interactions, RAL-89-106 (1989).

[10] E. Engels *et al.*, A Silicon Microstrip Vertex Detector for Direct Photon Physics, Nucl. Instrum. Meth. **A253**, 523 (1987).

[11] E. Engels *et al.*, Performance Characteristics and Radiation Damage Results from the Fermilab E706 Silicon Microstrip Detector System, Nucl. Instrum. Meth. **A279**, 272 (1989).

[12] K. Hartman, Hadronic Production of π^0 Pairs and Associated Event Structure at 530 GeV, Ph.D. thesis, Pennsylvania State University, 1990.

[13] C. Bromberg *et al.*, Design and operation of large straw–tube drift chamber planes, Nucl. Instrum. Meth. **A307**, 292 (1991).

[14] W. DeSoi, Construction and Performance of a Liquid Argon Calorimeter for Use in E706 at the Fermi National Accelerator Laboratory, Ph.D. thesis, University of Rochester, 1990.

[15] L. Sorrell, The E706 Trigger System, E706 Note 201.

[16] R. Roser, Eta Production at High Transverse Momentum by Negative 520 GeV/c Pions Incident on Beryllium and Copper Targets, Ph.D. thesis, University of Rochester, 1994.

[17] P. Chang, Massive $\pi^0\pi^0$, $\pi^0\pi^-$ and $\pi^0\pi^+$ Production from 515 GeV/c π^- Collisions with Beryllium and Copper Targets, Ph.D. thesis, Northeastern University, 1994.

[18] R. Benson, Characteristics of Forward Energy Production in Proton-Nucleus and Pion-Nucleus Collisions at 530 GeV/c, Ph.D. thesis, University of Minnesota, 1989.

[19] W. Długosz, The Production of High p_T π^0 Mesons in 515 GeV/c π^- - Nucleus Collisions, Ph.D. thesis, Northeastern University, 1994.

[20] S. Blusk, Measurement of the Production Cross Section of Charm Mesons at High Transverse Momentum in 515 GeV/c π^- -Nucleon Collisions, Ph.D. thesis, University of Pittsburgh, 1995.

[21] L. Sorrell, Measurement of the Nuclear Dependence of Direct Photon and Neutral Meson Production at High Transverse Momentum by Negative 515 GeV/c Pions Incident on Beryllium and Copper Targets, Ph.D. thesis, Michigan State University, 1995.

[22] N. Varelas, π^0 Production at High Transverse Momenta from π^- Collisions at 520 GeV/c on Be and Cu Targets, Ph.D. thesis, University of Rochester, 1994.

[23] M. Begel, Ph.D. thesis, University of Rochester, in preparation.

[24] R. M. Barnett *et al.*, Review of Particle Properties, Phys. Rev. D **54**, 1 (1996).

[25] G. Marchesini, I. G. Knowles, M. H. Seymour, and B. R. Webber, *HERWIG Reference Manual*, v5.6 ed.

[26] F. Carminati *et al.*, *GEANT: Detector Description and Simulation Tool*, 1993.

[27] G. Osborne, Direct Photon and Neutral Meson Production at High Transverse Momentum by Negative 515 GeV/c Pions and 530 GeV/c Protons Incident upon Hydrogen, Beryllium and Copper Targets, Ph.D. thesis, University of Rochester, 1996.

[28] P. Aurenche *et al.*, The gluon content of the pion from high-p_T direct photon production, Phys. Lett. B **233**, 517 (1989).

[29] P. Aurenche *et al.*, Gluon content of the nucleon probed with real and virtual photons, Phys. Rev. D **39**, 3275 (1989).

[30] H. L. Lai *et al.*, Global QCD analysis and the CTEQ parton distributions, Phys. Rev. D **51**, 4763 (1995).

[31] P. Aurenche *et al.*, Prompt photon production at large p_T in QCD beyond the leading order, Phys. Lett. B **140**, 87 (1984).

[32] F. Aversa *et al.*, Nucl. Phys. B **327**, 105 (1989).

[33] B. A. Kniehl, J. Binnewies, and G. Kramer, Pion and kaon production in e^+e^- and ep collisions at next-to-leading order, Phys. Rev. D **52**, 4947 (1995).